UNIVERSITÀ DEGLI STUDI DI PADOVA

TÉCNICO LISBOA

UNIVERSITÀ DEGLI STUDI DI PADOVA

DIPARTIMENTO DI INGEGNERIA INDUSTRIALE

Corso di Laurea Magistrale in Ingegneria Chimica e dei Processi Industriali

Tesi di Laurea Magistrale

CONSTRUCTION AND EXPLOITATION OF AN EXPERIMENTAL DEVICE TO TEST THE WETTABILITY OF STAINLESS STEEL BY LIQUID GALLIUM

Relatore: Prof. Piergiorgio Sonato

Relatore estero: Prof. Alberto Ferro

Correlatore: Dott. Rui Barrocas Gomes

Laureando: CATERINA CAVALLINI

ANNO ACCADEMICO: 2018 - 2019

ABSTRACT

Using external magnetic fields as means of plasma confinement is one of the successful strategies to achieve controlled nuclear fusion. Tokamak devices are showing constant progress in design during the past few decades. A big problem still to tackle is how to handle the high heat and particle loads on the walls that face plasma in a fusion reactor. Although nowadays solid materials are the most employed ones as plasma facing components, the problems related to their use have led to the research of viable alternatives. Liquid metals are considered the most feasible replacement since they partly improve lifetime and power-exhaust issues by introducing a self-healing, self-replenishing surface with no damage by neutron impact.

The topic of this thesis is the study of the wetting phenomena of stainless steel by liquid gallium, a liquid metal that could be used as plasma facing component. The assessment of the wetting properties of gallium is crucial for its application with materials that might be used as capillary porous systems (CPS), like stainless steel.

In this work, an ultra-high vacuum experimental set-up is designed and constructed in order to investigate gallium wetting properties on stainless steel samples. The experimental set-up is exploited to study how temperature, roughness and time affect the wetting process. All the experiments are recorded with a digital HD video camera recorder and the videos are further analysed by a specific software.

CONTENTS

LIST OF FIGURES

LIST OF TABLES

INTRODUCTION

The work here presented was entirely carried out at the Instituto de Plasma e Fusão Nuclear (IPFN) in Lisbon where the ISTTOK machine is located.

The increasing global energy demands driven by population growth and rising standards of living is becoming an issue. One of the greatest challenges of our time is to find a sustainable energy production with much lower environmental impact than conventional technologies.
Energy from nuclear fusion could be that alternative since it is a relatively unlimited, zero CO_2 energy source.
Currently, the most investigated fusion reactor is the Tokamak, a magnetic confinement machine.

High power magnetically confined fusion devices have very high heat and particle loads on the walls that face their plasmas. Handling this heat is a big challenge, in present and future devices. Solid materials used as plasma facing components (PFCs) undergo to surface melting, deterioration and surface cracking due to the impinging of these energetic particles. Liquid metals can be a feasible replacement to the solid materials since they partly improve lifetime and power-exhaust issues by introducing a self-healing, self-replenishing surface with no damage by neutron impact. By now, several liquid metals have been studied, like lithium (Li), gallium (Ga) and tin (Sn).

The topic of this thesis is relevant in the framework of the potential application of liquid gallium as plasma facing component as a reliable solution to the problem of heat exhaust at the divertor region of the Tokamak. Some concepts are already being tested at the proof-of-principle level, i.e. free-flowing surface or capillary porous system (CPS) in several devices among which ISTTOK and FTU. A crucial point in the liquid metal European strategy is the assessment of the wetting properties of gallium on materials that might be used as CPS, like stainless steel.

The main motivation of this work is to fulfil the lack of data about the gallium wettability on Stainless Steel 316. The choice of gallium with respect to lithium relies

at first on the several advantages of this liquid metal, like its wide liquid range, low reactivity in air and good power extraction capability. Furthermore, the choice was dictated by the curiosity and deep willpower to increase the limited pre-existing knowledge on gallium.

In order to study the wettability of stainless steel by liquid and oxide-free gallium, a specific experimental device was designed and constructed.

The first chapter provides a general introduction to the fusion energy and briefly describes the tokamak machine used to magnetically confine the plasma. Moreover, the Plasma-Wall interaction issue is here presented.

In the second chapter, liquid metals are presented as a possible alternative to the standard solid materials as PFCs. After a general comparison between the most investigated liquid metals, the focus is moved to gallium since is the chosen one to carry out this work.

The third chapter classify the wetting process into non-reactive and reactive wetting. Moreover, a definition of wetting and contact angle θ is here given. The focus in mainly on wetting by liquid metals.

In the fourth chapter, the two techniques used to treat the sample surface used in this work are presented. Afterwards, the experimental set-up specifically constructed to carry out the experiments is presented and described in detail.

The experimental results are presented in the fifth chapter. Two different series of experiments have been carried out in order to understand the effect of roughness, temperature and time on the wetting process. The conclusions are drawn at the end.

1

NUCLEAR FUSION ENERGY

In this first chapter, the necessity to investigate sources of energy alternative to the carbon based ones, is approached. These should be able to conjugate the increasing world energy demand while ensuring environmental sustainability. Fusion energy is one of the possible solutions and its main principles are explained in the second section of this chapter. In the third section, the tokamak machine used to magnetically confine the plasma is briefly described. The last section introduces the Plasma - Wall interaction topic and the importance of the research on new materials able to handle the high power load impinging on the walls of nuclear fusion devices.

1.1 THE WORLD ENERGY SCENARIO

Access to affordable, abundant energy, mainly from fossil fuel sources, has been a key factor in economic growth since the Industrial Revolution [1]. Nevertheless, the growth in world energy demand from fossil fuels has played an important role in the upward trend in CO_2 emissions: it has been demonstrated that in 2016, the average concentration of CO_2 was about 40% higher than in the mid-1800s, with an average growth of 2 ppm/year in the last decade [2]. The global energy consumption is increasing rapidly and, according to the U.S. Energy Information Administration (EIA), the world energy demand will be 28% higher in 2040 compared to that of 2015 (Figure 1.1). Furthermore, the biggest increase is expected to come from developing countries [3]. As a consequence, the research on renewable sources of energy is nowadays one of the most important scientific topics and goals. To sustain the non-renewable resources and reduce CO_2 emissions, the only available path is to develop new forms of renewable energy production.

Nuclear fusion is a future energy option since it could acquire a significant role in providing sustainable, secure and safe energy to the whole world. As a matter of fact, the nuclear fusion reaction is an inherently safe reaction since there are no possibilities of runaway reactions. Moreover, the fuel used to carry out this reaction

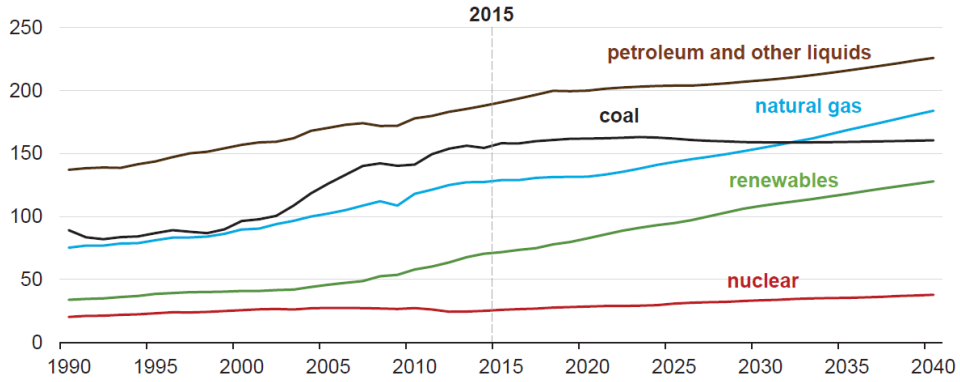

Figure 1.1: World energy consumption by energy source [3].

has no availability limits, no long-lived radioactive waste is produced and finally, no CO_2 greenhouse gas emissions are released.

1.2 PRINCIPLES OF NUCLEAR FUSION

Fusion is a form of nuclear energy that involves the merging of light elements to create a nucleus of larger mass number.

The nucleus of atoms are constituted by a number of protons (Z) and neutrons (N=A-Z, where A is the atomic number of the element), but the mass of a nucleus is always less than the sum of the single masses of its protons and neutrons. The difference represents the nuclear binding energy, which holds the nucleus together [4].

The *binding energy* of a nucleus is the energy required to completely disassemble it into separate protons and neutrons. The energy released during a fusion reaction indicates a decrease in the final total nuclear mass. This difference in mass is transformed into energy following the Einstein's equation:

$$E = \Delta m c^2 \tag{1.1}$$

All fusion reactions can only occur if the interacting nuclei have a kinetic energy that overcomes the repulsive Coulomb potential energy [4]. The probability that this Coulomb barrier will be overcome and that two light nuclei will undergo a nuclear fusion reaction is defined as *cross section* σ. The reaction rate of a nuclear reaction is the number of reactions per unit volume per unit time and is proportional to $<\sigma v>$. This latter is an average product of σ and v, which is the nuclei relative velocity of the nuclei taking into account the distribution of velocities of the different

particles [5]. A candidate reaction for commercial power plant must be exothermic and the cross-section must be high enough at achievable energies. Moreover, the reaction chosen should let the fusion power plant to reach a fusion gain between Q[1]=10 and 50. Some of the considered and studied reactions to achieve controlled thermonuclear fusion under on earth involve the hydrogen isotopes deuterium ${}^{2}_{1}H$ and tritium ${}^{3}_{1}H$ and are listed below:

1. Deuterium - Deuterium reaction (D - D)

$$ {}^{2}_{1}H + {}^{2}_{1}H \rightarrow {}^{3}_{2}He + {}^{1}_{0}n + 3.27MeV \tag{1.2} $$
$$ {}^{2}_{1}H + {}^{2}_{1}H \rightarrow {}^{3}_{1}H + {}^{1}_{1}H + 4.04MeV \tag{1.3} $$

2. Deuterium - Helium reaction (D - ${}^{3}He$)

$$ {}^{2}_{1}H + {}^{3}_{2}He \rightarrow {}^{4}_{2}He + {}^{1}_{1}H + 18.3MeV \tag{1.4} $$

3. Deuterium - Tritium reaction (D - T)

$$ {}^{2}_{1}H + {}^{3}_{1}H \rightarrow {}^{4}_{2}He + {}^{1}_{0}n + 17.59MeV \tag{1.5} $$

Figure 1.2 shows reaction the rates variation with temperature for reactions 1.2, 1.3, 1.4 and 1.5. The D-T reaction (Eq.1.5) has the highest reactivity at lower temperature. As a matter of fact, it can be carried out at about 150 - 200 million °C,

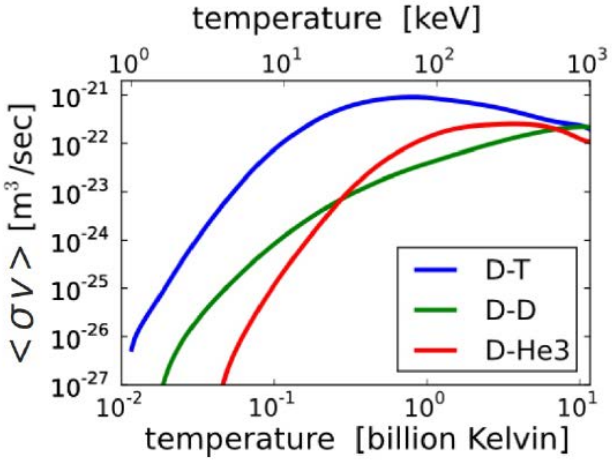

Figure 1.2: Reaction rates of the D - T; D - D and D - ${}^{3}_{2}He$ reactions [6]

[1]Q, in fusion, is the energy gain factor: ratio between the power produced by the fusion reactions and the external power required to sustain them via plasma heating

whereas the D - D reaction (Eq. 1.2 and 1.3) requires higher temperatures of 400 - 500 million °C since there is a lower probability that a pair of D - D nuclei will collide.

In order to provide the amount of energy necessary to overcome the Coulomb barrier, the reactants must be heated at very high temperatures, at which they become plasma. A thermonuclear plasma can be defined as a totally ionized gas containing ions and electrons. In a plasma, some electrons are freed from their atoms, allowing current to flow [7].

Taking into consideration the deuterium-tritium reaction (Eq. 1.5), which is the most favourable, the final products are charged alfa particles ${}^4_2He$ and neutrons. The alfa particles can be confined by a magnetic field, as will be better explained in Section 1.3, and interacts with the other charged particles, like ions and electrons, present in the plasma, acting as heating source. By contrast, neutrons cannot be confined and escape the plasma, impinging and releasing energy to the solid walls that surround the plasma [6].

One of the main advantages of fusion is the high natural abundance of inexpensive fuel that has the potential to supply large amounts of energy for thousands of years. As a matter of fact, deuterium, which is one of the reactant, can be distilled from water. By contrast, tritium, the second required fuel, is a fast-decaying radioelement of hydrogen with a short half-life [2] of about 12 years and so does not occur naturally in abundance on Earth [4]. To overcome this issue, tritium is breed in the blanket surrounding the region of D - T reaction and is produced during the fusion reaction from lithium: neutrons that escape the plasma interact with lithium contained in the reactor blanket and tritium is produced by the following reactions:

$$ {}^6_3Li + {}^1_0 n \rightarrow {}^3_1 H + {}^4_2 He + 4.78MeV \tag{1.6} $$

$$ {}^7_3Li + {}^1_0 n \rightarrow {}^3_1 H + {}^4_2 He + {}^1_0 n - 2.5MeV \tag{1.7} $$

The second reaction (Eq. 1.7) is endothermic, therefore the Li-fuel is enriched by ${}^6_3Li$ to maximize energy output [6].

The conditions that must be achieved by the plasma in order to have a net production of energy are determined by the *Lawson Criterion*. In 1955 John D. Lawson

[2] Half-life: the amount of time that a given amount of substance takes to half undergo some specified process. For a radioactive substance, is the time required by half of its atoms to decay.

proposed an ignition criteria for the Deuterium-Tritium (D-T) plasma in a magnetic fusion device. This criterion is following reported in terms of triple product:

$$nT\tau_E \geq 1.2 \cdot 10^{21} \quad [keVsm^{-3}] \tag{1.8}$$

where n is the plasma density, T is the temperature of the DT plasma in KeV and τ_E is the plasma confinement time in seconds, which indicates the rate at which the plasma loses energy. In order to produce energy from fusion reactions, a sufficiently hot (T) and dense (n) plasma must be confined effectively (τ_E) [8].

1.3 THE TOKAMAK MACHINE

To be able to create these fusion reactions, several conditions must be met. The mass of the stars is so high that gravity force is able to compress hydrogen to densities and temperatures so high that the creation of hot and confined plasma is allowed and ignition of a nuclear usion reaction is initiated. On earth, gravity force is not high enough and the desired plasma density can be achieved by the injection of extra particles in the system. On the other hand, a magnetic field confinement can be used to confine charged particles that characterized plasma. High temperatures can be obtained only thanks to gas heating techniques, for example circulation of strong current (ohmic heating) or injection of high energy particle beams or radiations (additional heating). Some different types of closed magnetic configurations for plasma confinement have been devised and tested over the years, such as Tokamak, Stellarators, Z-pinch and Reversed Field Pinch (RFP).

The Tokamak machine is the most extensively investigated machine, so far. The word "tokamak" is derived from the Russian words, *toroidalnaya*, *kamera* and *magnitnaya katushka* , meaning "toroidal chamber" and "magnetic coil". This reactor has the shape of a torus. The direction along this torus is named as "toroidal direction", whereas the plane perpendicular to this latter is called "poloidal plane".

The main role of the magnetic field is to confine the plasma and keep it away from the reactor *first wall* that protects the structure behind it from direct radiation and particle loads. Behind the first wall there is the *breeding blanket* which has three main roles: the first one is to remove the heat from the reactor to produce electricity, the second one is to create new fuel (tritium from lithium) and the last one is to shield the vacuum vessel (Figure 1.3a).

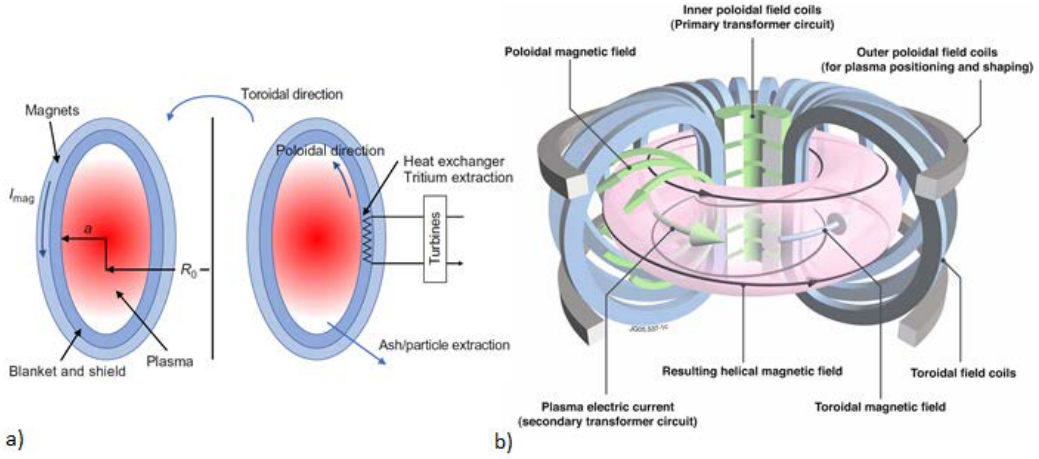

Figure 1.3: a)Section of a Tokamak showing the plasma, blanket, shield, magnets and power extraction [5]; b) Diagram illustrating the tokamak principle: arrangement of magnetic field coils and the resulting magnetic field that confines the plasma [9].

Any tokamak has a set of external poloidal-field (PF) coils, including the primary transformer and additional control coils, concentric with the toroidal vacuum vessel. Furthermore, a series of coils, placed all around the torus, generates a toroidal magnetic field B_T. The magnetically confined plasma inside the chamber acts as the secondary winding of a transformer. Plasma is ohmically heated by the current I_P produced in the primary. This current also induces a poloidal field B_P. The combination of the toroidal B_T and poloidal fields B_P give rise to magnetic field lines which have helical trajectory around the torus [10]. A tokamak geometry can be generically defined by its major radius R_0, minor radius a, the toroidal field B_T and the plasma current I_P. A schematic representation of a tokamak is reported in Figure 1.3b.

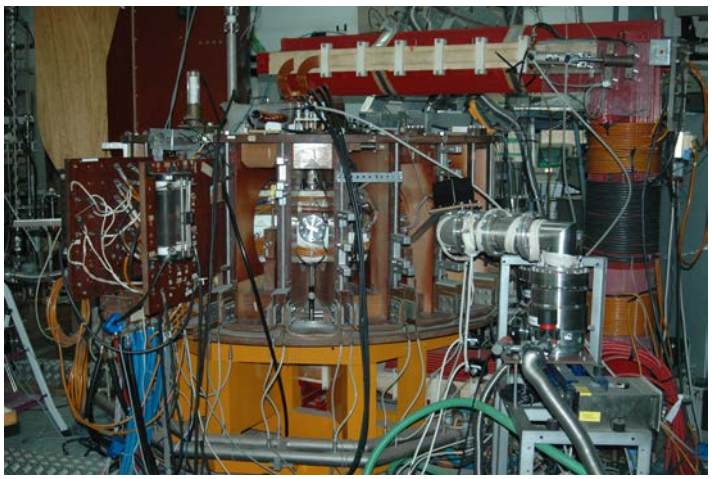

Figure 1.4: ISTTOK - Instituto Superior Técnico TOKamak

Table 1.1: Main characteristics of the previous mentioned Tokamaks

Device	R_0 [m]	a [m]	I_P [MA]	B_T [T]	Location
JET	3.0	1.0	6.0	4.0	United Kindom
ISTTOK	0.46	0.085	0.007	0.5	Portugal
ITER	6.2	2.0	15.0	5.3	France

The largest Tokamak is the Joint European Torus (JET) built in Culham, close to Oxford, in the early '80s. Another one present in Europe is ISTTOK, which is a small tokamak located in Lisbon (PT) at the *Instituto Superior Técnico* (Figure 1.4)

Currently, 35 nations are collaborating to build the world's largest tokamak, ITER, a magnetic fusion device that has been designed to prove the feasibility of fusion as a large-scale and carbon-free source of energy. ITER ("The Way" in Latin) is one of the most ambitious energy projects in the world today and is going to be build next to Cadarache in Saint-Paul-lès-Durance, in Provence, southern France [7].
Table 1.1 reports the most relevant characteristics of the mentioned Tokamaks.

1.4 PLASMA-WALL INTERACTIONS

Making commercially-viable fusion power reality is a very challenging objective since lots of issues have still to be faced and solved. One of the main issues is strictly connected to the ability of plasma-facing components (PFC's) to handle large particle and power loading. The order of magnitude of the power flux at the wall per unit surface is of Megawatts per square meter [MW/m^2]. Therefore, in order to handle the high power loads impinging on the first wall, there are two main possible "plasma-wall interface" configurations: the *limiter* and the *divertor* [11].

The *limiter* is a solid material inserted in the vacuum chamber in different configurations (Figure 1.5). The magnetic field lines of the Tokamak are defined *closed* if they don't impact a solid surface, whereas they are *open* if they pass through it. The last flux surface which doesn't hit the solid surface is defined as *last closed (magnetic) flux surface - LCFS*. The main concept behind the limiter is that, as the plasma flows across the LCFS, particles and also energy is deposited on the limiter surface: since outside the LFCS almost any field lines close on themselves, most of these lines will impinge the limiter [11].

The region radially outside the LCFS is called *scrape-off layer - SOL*.

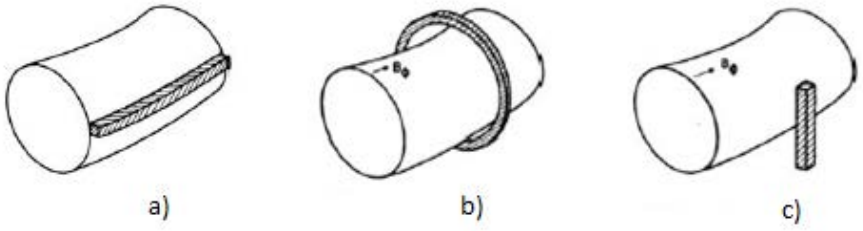

Figure 1.5: Various limiter configurations: a) *toroidal limiter* which is a structure mounted outside the vessel; b) *poloidal limiter* which is a circular annular plate; c)*rail or probe limiter* which is a solid directly inserted into plasma at a specific point [12]

One of the main drawbacks of the limiter is that, since it is very close to the plasma, it increases the number of impurities that enter the plasma and contribute to radiative losses. Moreover, the limiter is always exposed to extreme conditions that reduce its performance with time inducing the substitution of the limiter itself at a certain point [12].

Another possible solution to handle the power heat load at the walls is the *divertor*. This latter is characterized by extra coils that generate a toroidal current I_D in the same direction of I_P. The sum of the magnetic lines gives rise to a eight shape in the poloidal plane. As it is shown in Figure 1.6a, a solid plane divides the flux surfaces originated by the I_D: as plasma diffuses across the LCFS, particles that travel along the field lines are collected and deposited on the solid surface called *target plate* (Figure 1.6c) [11]. Thanks to the possibility to move these targets far from the confined

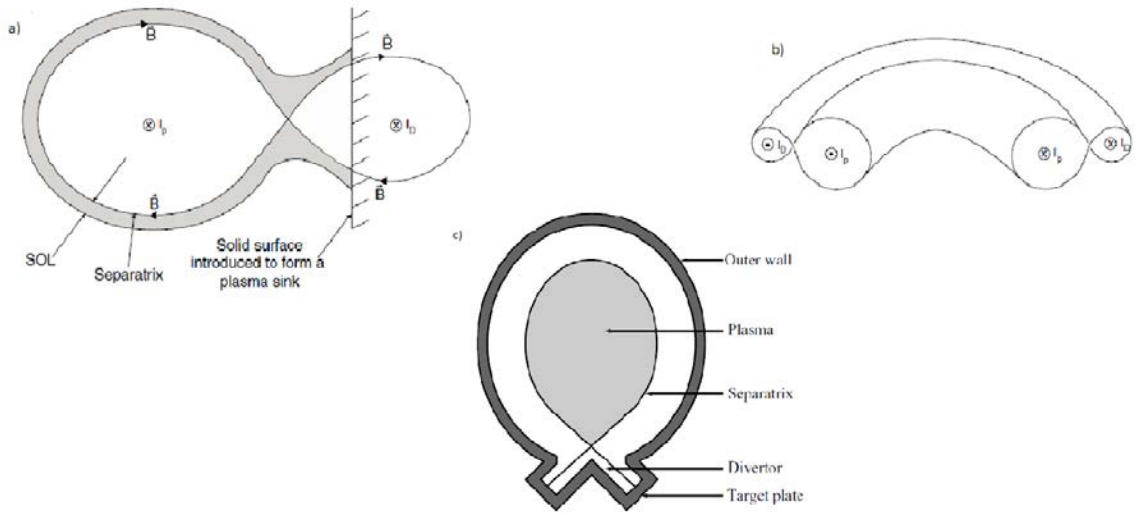

Figure 1.6: Schematic diagrams of a divertor: a) and b) divertor coil current I_D is generated parallel to I_P [12]; c) section of divertor in poloidal plane [11]

plasma, the divertor isolates better the impurities that can enter the plasma [12].

To handle the high power density loads to whom plasma face components (PCFs) are submitted and that can even reach the GW/m^2 range during off-normal events, a valuable alternative was proposed by Christofilos in 1970 [13]. This different approach consists in the replacement of the solid PFCs by liquid metals (LMs).

2

LIQUID METALS

In this second chapter the general concept of Plasma Facing (PFCs) Components is at first described. Afterwards, liquid metals are presented as a valid alternative to solid PFCs and, in particular, a comparison between lithium and gallium is presented in order to explain the reasons behind the final choice of liquid gallium to carry out the experiment presented in this work of thesis. In the second section of this chapter, the focus is placed on the oxidation and corrosion of gallium since these latter concepts are the ones important for the design and set-up of the experiment described in Chapter 4.

2.1 PLASMA-FACING COMPONENTS

Plasma-facing components (PFCs) of a fusion reactor have to withstand steady state and transient heat load that can degrade the material itself. Moreover, they are exposed to the impact of neutrons that can also decrease the lifetime of the wall components. The development and study of materials that can withstand these extreme conditions is a big technological challenge for fusion science. The general characteristics that a PFC should have are the following:

1. compatibility with plasma operation, in other words, the capability of the material to offer low contamination levels, guaranteeing plasma discharges with low impurity levels;

2. non-reactivity with plasma to avoid the generation of volatile components;

3. resistance to chemical and physical sputtering: the lifetime of a PFC depends on its erosion rate that leads to its damage and disintegration during the plasma operations;

4. good thermal shocks resistance and thermo-physical properties in order to be able to handle the high power loads;

5. a negligible or small long term retention of tritium (T) fuel to avoid radioactive issues and potential safety limitations;

6. a good neutron resistance and a low long term activation [14]; [15].

Unfortunately, a suitable material that gathers all these requirements is not available. All the PFCs can be classified into two main categories:

1. **High Z materials**: generally, they have low sputtering yield, high melting point and low impurities retention values but their main drawback is that their degradation leads to heavy impurities that go into the plasma and cool it down by radiation losses. The most studied and employed high Z materials are tungsten (W) and molybdenum (Mo).

2. **Low Z materials**: they have a moderate impurity production from sputtering and evaporation under plasma influence. The particles released into the plasma by these materials have a lower negative effect with respect to high Z materials since they radiate lower amounts of stored energy. The final result is a lower detrimental effect in plasma performance. The main drawbacks are their weak resistance to erosion and fuel retention characteristics. The most investigated low Z materials are graphite, beryllium (Be) and lithium (Li).

ITER will have a beryllium (Be) first wall and a tungsten (W) divertor. The reference value of the ITER fusion power is 1500 MW and ITER divertor should be capable to carry up to 315 MW from the main plasma [16].

Beryllium was selected because it has low atomic number and good retention of oxygen impurities that lead to an improvement of vacuum. Moreover, it also exhibits better erosion resistance compared to carbon. Nevertheless, beryllium has also some of drawbacks: first it has a low melting temperature of 1550 K that can be an issue under transient events, and second, it becomes very brittle under neutron impact that can lead to the release of hazardous dust in the plasma. Beryllium in the form of dust is very toxic and carcinogenic and there are only a few laboratories in the world that have the adequate equipment and installations to work with beryllium.

On the other hand, the selection of tungsten for the divertor is related to its high melting temperature (3695 K) and low sputtering by deuterium (the required energy threshold is quite high: 200 eV). Moreover, tungsten can exhaust the heat better than other materials thanks to its rather high thermal conductivity (W: $\sim$ 173 W/(mK); Cu: $\sim$ 390 W/(mK); Mo: $\sim$138 W/(mK)) [17]. By contrast, tungsten is very brittle at low

temperatures (<600 K) and it shows a reduction of strength and hardness above the recrystallization temperature (1300 - 1600 K). Moreover, the neutron impact enhances the material embrittlement reducing the ductile-brittle transition temperature (DBTT) to 950-1050 K [15].

2.1.1 *Liquid metals as Plasma facing components*

Liquid Metals (LMs) are considered a valid alternative to solid materials as PFCs thanks to their self-cooling, self-annealing, and self-healing capability. Moreover, they can exhaust power impinging on the first wall and particularly on the divertor and limiter regions of fusion reactors. As a matter of fact, they are potentially able to withstand peaks of heat fluxes greater than 50 MW/m^2. Another positive aspect is that their liquid surface is renewable and doesn't suffer from the radiation damage due to erosion mechanisms or neutron irradiation. Furthermore, evaporated metal forms a cloud in front of the plasma facing components (PFCs) that reduces heat load to the divertor by radiation cooling. [18].
By now, several liquid metals have been studied, like lithium (Li), gallium (Ga), tin (Sn). In Table 2.1 the main properties of the previously mentioned liquid metals are reported .

So far, lithium is the element that has been most widely investigated so far. It has an excellent compatibility with plasmas since it keeps the level of plasma contamination thanks to its low Z (Z = 3). Moreover, liquid lithium can also disperse highly localized heat loads by evaporation and/or radiation. Furthermore, lithium is also a good oxygen and nitrogen getter and its interaction with hydrogen isotopes leads to a reduced fuel recycling to the SOL, producing associated and spectacular benefits to the plasma performance.

Table 2.1: Liquid metals properties

	Li	**Sn**	**Ga**
Melting Point [K]	453	505	302
Boiling Point [K]	1615	2875	2477
Density ρ [kg m^{-3}]	534	7300	5910
Thermal Conductivity κ [W $m^{-1}K^{-1}$]	45	40	55
Specific Heat Capacity c_p [J $kg^{-1}K^{-1}$]	4300	250	380

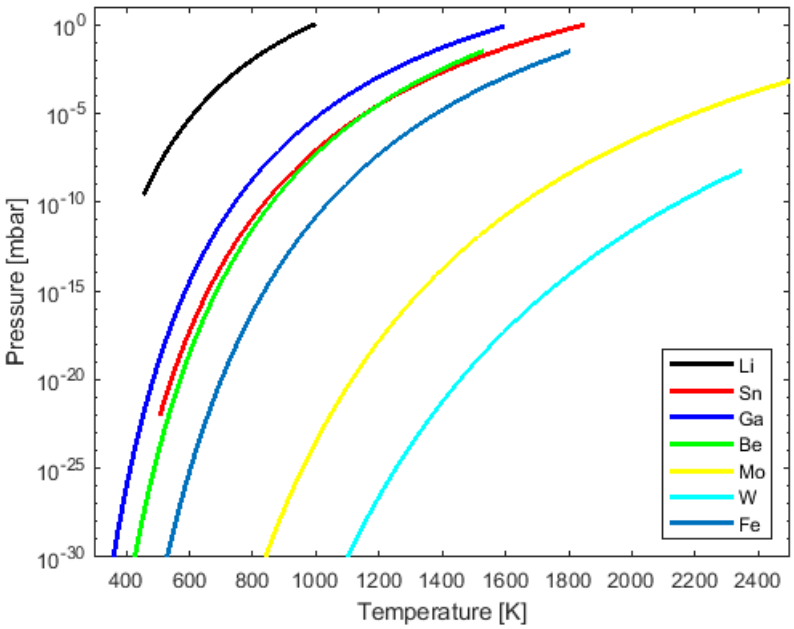

Figure 2.1: Metals vapour pressures as a function of temperature [21]

Despite all, lithium has a highly reactive chemical nature that leads to a strong hydrogenic retention (potentially tritium), therefore a tritium recovery system is required to reduce the tritium concentration. In addition, lithium has a strong reactivity with air components and this could be an issue in the case of accidental leaks. Furthemore, lithium reacts intensely with water, forming lithium hydroxide and higly flammable hydrogen. In the end, lithium has also a narrow temperature range in which remains liquid: it melts at 180 °C and it reaches the partial pressure of 10^{-4} mbar at ∼400 °C (Figure 2.1), where the pressure mentioned is the general one required to produce plasma in a tokamak [19], [20], [18].

Another liquid metal that is gaining lots of attention from the scientific world is gallium. One of the main advantages of gallium is that the temperature range in which it remains liquid is much wider: the melting point is 30°C whereas the temperature at which the partial pressure of 10^{-4} mbar is achieved is at 890°C (Figure 2.1). This allows having a good power extraction capability. Moreover, gallium has lower reactivity with air: the main remarkable reaction is its oxidation. Gallium has an intermediate Z(Z=31) but this can be an advantage if gallium is used in the divertor: the high impurity radiation can help to handle the heat power load provided that gallium ions don't reach the core plasma.
One of gallium drawbacks is its high corrosion activity on most materials (Section

2.2.6). [19] [20], [18].

Tin (Sn) due to its low melting point, low vapor pressure and low fuel retention is the main candidate as PFC next to Gallium, especially in the form of Sn-Li alloy.The sputtering and evaporation characteristics of these alloy were tested at the laboratory level, confirming the preferential sputtering and evaporation of the Li component. This can be an issue since would alter the bulk properties of the material, precluding the benefits of lithium contant and thus needing Li surface replenishment to restore the Li-Sn proportion on the exposed layers. Investigations with pure tin elements are currently underway [22].

Through the years, two main different approaches for the use of Liquid Metals as a protective surface in fusion reactors have been tested and studied.
The first one is based on a moving liquid metal film. As an example, on ISTTOK, a stable, free-flying liquid gallium jet has been developed in order to study its interaction with the tokamak edge plasma [23].
Due to MHD forces found in the implementation of this free moving liquid metal film in a magnetic fusion machine, a second alternative was proposed by a group of Russian researchers: the capillary porous system (CPS). The main concept behind this solution is the capillary force that arises when a flow of liquid metal is injected under a solid porous material: the high surface tension that characterizes these material allows to reach good wetting with LMs [19]. The capillary porous system will be treated in more details in Chapter 3.

Gallium is the liquid metal chosen to carry out the work presented in this thesis. This choice relies on the advantages of this liquid metals presented in Section 2.1.1 and on the curiosity and deep willingness to increase the limited pre-existing knowledge on gallium.

2.2 GALLIUM

2.2.1 *History of gallium*

Gallium was discovered in Paris by Paul-Émile Lecoq de Boisbaudran in 1875 while he was studying the spectra [1] of the chemical elements. At that time, Mendeleev had already predicted that there was a missing element: he had left a gap in his periodic

[1]Spectra: lines produced by elements when they are excited. Each element produces its own spectra.

table below aluminium, in position 31, and had forecasted that this still unknown element should be similar to aluminium (Z=13, above box 31) and indium (Z = 49, below box 31).
In 1875, Lecoq de Boisbaudran was working through a large amount of zinc ore (ZnS) when he observed a new violet line in the atomic spectrum of zinc and understood that he had found out a new element. Later that year, Lecoq isolated gallium metal and announced his discovery to the French Academy of Science. He proposed the name "Gallium" for this new element in honour of the ancient name for France, Gallia.

2.2.2 *Physical properties*

Gallium (Ga) is a chemical element with atomic number 31. It is a soft, silvery-blue metal similar to aluminium and with a shiny surface. With an average crustal abundance of 17 ppm, Ga is considered a trace metal.

Solid Ga crystallizes in an orthorhombic unit cell [2]. Six Ga isotopes have been identified but natural gallium consists of a mixture of only two stable isotopes: gallium-69 (60.4 %) and gallium-71 (39.6 %). In Table 2.2 the main atomic properties of gallium are reported.

Gallium has some unusual physical properties for a metal. First, it has a very low melting point of 29.7 °C. Therefore, it can be melted in a human hand. Second, it can be supercooled, which means that it can be cooled down below its freezing point without becoming solid. Another interesting characteristic is that liquid gallium

Table 2.2: Gallium atomic properties [24]

Periodic Symbol	Ga
Atomic Number (Z)	31
Atomic Mass	69.72 g/mol
Atomic Radius	130 pm
Electronic Structure	$1s^2\ 2s^2\ 2p^6\ 3d^{10}\ 4s^2\ 4p^1$
Oxidation States	-5; -4; -2; -1; +1; +2; +3
Stable Isotopes	^{69}Ga (abundance: 60.11%); ^{71}Ga (ab. 39.89%)
Crystal Structure	Orthorhombic [3]

[2]Orthorhombic system: structural category in which crystals are referred to three mutuall perpendicular axes that are unequal in length

Table 2.3: Gallium physical properties [24]

Variable	Property	Value
T_{mp}	Melting Point °C	29.79
T_{bp}	Boiling Point °C	2203
ρ	Density [kg m^{-3}]	
	293 K	5907
	at T_{mp}, Solid	5903.7
	at T_{bp}, Liquid	6094.8
μ	Viscosity[kg/m·s]	$321.5 + T^{-0.89}$
λ	Thermal Conductivity [W/m·K]	
	at 293 K, Solid	Axis a: 88.4 Axis b= 16.0 Axis c= 40.8
	at 350 K, Liquid	28.7
C_p	Specific Heat Capacity [J/kg·K]	
	0 K≤T≤200 K	-395 + 330 log[T]
	200 K≤T≤1400 K	367.8 + 0.06 T
γ	Surface Tension [mN/m] at 303 K	709
ΔH_v	Heat of Vaporization [KJ/mol]	1.014
ΔH_f	Heat of Fusion [KJ/mol]	5.563
β	Volumetric thermal espansion coeff. [1/K]	
	at 273-293 K, Solid	$5.95 \cdot 10^{-5}$
	at 303 K, Liquid	$1.20 \cdot 10^{-4}$
ρ_e	Electrical resistivity [Ω-m]	
	At 293 K, Solid (polycrystalline)	$15.05 \cdot 10^{-5}$
	At 303 K, Liquid	$25.795 \cdot 10^{-5}$

expands by 3.1% when it solidifies. Other materials that have the same behaviour are water, silicon, germanium, bismuth, plutonium, and antimony. Moreover, gallium remains in the liquid phase in a wider temperature range with respect to lithium, as it was already said in Section 2.1.1. In Table 2.3 the main physical properties of gallium are reported.

2.2.3 *Chemical properties*

Gallium can form many substances, such as bromides, chlorides, hydrates, iodides, nitrides, oxides, selenides, sulfides, and tellurides. The chemical properties of the metals depend on its purity: the purer it is, the more chemically stable it is [25].

As it is reported in the Pourbaix diagram (Figure 2.2), solid gallium doesn't interact with dry air at room temperature and slowly oxidizes in moist air until a protective film is formed. On burning in air or oxygen, it forms the white oxide Ga_2O_3. The oxidation of gallium will be treated and explained in more details in the Section 2.2.5. Moreover, gallium neither reacts with water at room temperatures up to 100

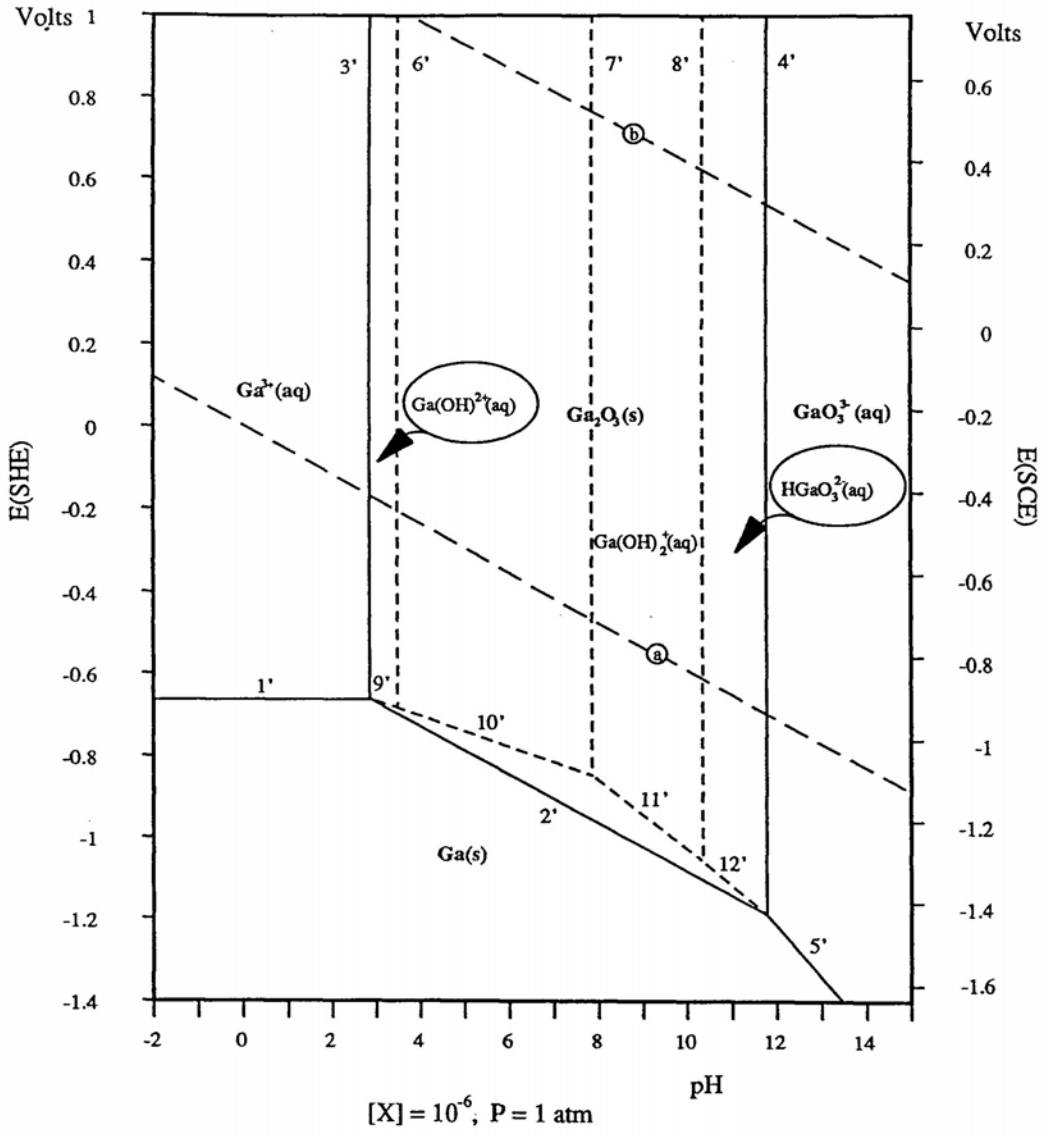

Figure 2.2: Potential-pH diagram of Gallium-water system at 298°C [26]

°C. By contrast, it reacts with hydrochloric and other mineral acids to give gallium ion Ga^{3+} and it dissolves in acids giving gallium salts, such as $Ga(NO)_3$. Also, alkalies dissolve gallium producing gallates salts that contain the $Ga(OH)_4^-$ anion. The dissolution process is a function of temperature: higher the temperature, faster is the reaction [27].

Gallium is amphoteric, which means that it reacts either in acid and basic environment.

In most of its compounds, gallium has an oxidation state of +3, but it can be also univalent and bivalent. With the chemical elements of the Group 15 (nitrogen, phosphorus, arsenic and antimony) and of the Group 13 (aluminium and indium), it forms compounds like gallium nitride (GaN), gallium arsenide (GaAs) and indium

gallium arsenide phosphide (InGaAsP) that are used in solid-state devices, such as transistors, thanks to their optoelectronic and semiconductor properties.

Gallium alloys are used in thermometers as a valid substitute to mercury since they are environmentally friendly and non-toxic. These alloys are called galistan since they are constituted by a eutectic composition of gallium, indium, and tin. There is no specific formula for galistan, but a general one can be the following: 68.5 %Ga, 21.5% In, 10% Sn.

Gallium can be considered a non-toxic metal: pure gallium is not a harmful substance for humans to touch, neither pose any large toxicological hazard in use. As an example, the gallium radioactive compound gallium citrate Ga-67 ($C_6H_5GaO_7$) is injected into the body for gallium scanning without harmful effects. Despite that, some precautions should be used everytime gallium is handled: eye contact with, or inhalation of gallium dust may cause irritation. Moreover, gallium oxide (Ga_2O_3) chronic industrial exposure has been examinated by Hahn [28]: he demonstrated that a month exposures of rats to this substance at concentrations near to the threshold limit values (TLVs) can induce lung damage; therefore, the human exposure to Ga_2O_3 at work should be limited.
Other gallium compounds have revealed to be very dangerous, such as gallium (III) chloride that can cause throat irritation and chest pain, up to pulmonary edema and partial paralysis if inspired [29].

2.2.4 *Gallium extraction*

Gallium does not exist in pure form in nature and its average crustal abundance is estimated to be 17 ppm. Usually, Ga is found in various amounts in aluminium ores, zinc ores, iron ores, coal ores, and other rocks. The majority of Ga is produced as a by-product of bauxite processing and the remainder from zinc-processing residues. In Table 2.4 the potential reserves of Gallium are reported.

It is estimated that bauxite contains more than 1 million tons of Ga, whereas the amount present in zinc resources is approximately 1.9 billion tons. Moreover the amounts of Ga present in coal resources are about 10 million tons. As a consequence of the low concentration of gallium, it is worthless to extract it mining the minerals and gallium is therefore recovered as a by-product from the production of aluminium and, to a lesser extent, from zinc production. It is estimated that about 90% of world

Table 2.4: Estimates of Ga potential reserve.

Raw Material	**Estimated reserve (10^9 tons)**	**Ga average content (ppm)**	**Ga potential resources (10^6 tons)**
Bauxite	55 - 75	50	>1
Zinc ore	1.9	50	0.095
Coal	>1000	10	10

primary gallium is produced from Bayer liquor obtained from the bauxite leaching process. In the Bayer process, about 70% of gallium is leached from bauxite and goes with aluminium into the caustic soda solution, whereas the remaining 30% forms the red mud.

Many methods have been developed to extract gallium from Bayer liquor, such as fractional precipitation while Al-Ga co-precipitate by using lime or CO_2. After the extraction, gallium can undergo purification by treatment with acid and alkaline solutions, filtering through porous glass partitions, and thermal treatment in vacuum [25], [27], [30].

2.2.5 *Oxidability of gallium*

As it was mentioned in Section 2.2.3, pure and dry oxygen doesn't react with solid Gallium up to 250-260 °C. Neither oxygen-free water affects this metal. By contrast, the reaction between liquid gallium and oxygen produces three main oxides: gallium protoxide (Ga_2O), gallium oxide (GaO) and gallium trioxide (Ga_2O_3).

The gallium oxide (GaO) was detected only by spectroscopy technique during the formation of Ga_2O_3 and Ga_2O. In fact, gallium oxide is produced under Ga_2O_3 reduction by hydrogen at 600°C. During this reaction, a huge amount of gallium protoxide is produced which further decompose into gallium trioxide,Ga_2O_3.

The gallium protoxide (Ga_2O) can be formed heating up to 500°C a mixture of gallium trioxide on metallic gallium:

$$Ga_2O_3 + 4Ga \rightarrow 3Ga_2O \tag{2.1}$$

This oxide is amorphous and it has a colour that varies from dark-brown to grey.

Finally, gallium trioxide Ga_2O_3 is the most stable of gallium oxides and it forms through the gallium oxidation reaction under heating:

$$2Ga + \frac{3}{2}O_2 \rightarrow Ga_2O_3 + 257kcal/mol \tag{2.2}$$

Gallium trioxide has five allotropic forms: α-, β-, γ-, δ- and ϵ-. All of these phases of gallium oxide can be prepared under specific conditions. As an example, α-Ga_2O_3 can be synthesized by heating GaO(OH) in the air between 450°C and 550°C and it is stable only in a temperature range between 300 and 600 °C [31].

The β- form is the most stable one and it can be obtained by baking any other polymorph of Ga_2O_3 in the air at sufficiently high temperatures (T>1000°C). Another possibility is through calcination of organic gallium compounds, like nitrites, at temperatures higher than 1000°C. Gallium oxide crystals can also be synthesized by sputtering, laser ablation and chemical vapour deposition [31].
The $\beta - Ga_2O_3$ has a density of 5.84 g/cm^3 and it is a poor thermal conductor. Due to its crystalline anisotropy, the thermal conductivity is different along different crystal directions: the highest value is 21 W/mK in the [010] direction [31].

Contrary to the fact that solid gallium doesn't react with oxygen at ambient temperature, oxidation of a liquid gallium surface occurs spontaneously when exposed to oxygen at T$\sim$20°C. The diffusivity of oxide particles on a liquid surface is much higher than on a solid surface. The oxidation reaction stops when oxygen doesn't diffuse anymore through the oxide layer. The resulting film is mechanically unstable and it can be easily ruptured by small oscillations. The formed cracks allow the rise of the oxide film.

Some experiments have demonstrated that some oxide clusters are generated on the liquid gallium surface a few minutes after this latter was exposed to oxygen. By the time, the size of the clusters increases thanks to their aggregation into larger ones but the width of the oxide layer remains almost the same [32]. The fractal-like structure that is formed on liquid gallium is not observed on the same solid metal on which, only at high temperatures, the oxide originates homogeneously along the exposed surface to oxygen. Therefore, it has been demonstrated that an isotropic, nonequilibrium diffusion aggregation process is responsible for the growth of the oxide layer on the liquid surface. The formation of this layer can be described as

following: oxygen after being chemisorbed on the liquid surface, diffuses and reaches a preexisting oxide laterally expanding this latter. A steady state point is reached when all the oxygen adsorbed on the surface is transferred to the growing oxide edge [33].

Some specific procedures have been studied and tested through years in order to work with pure liquid gallium. A possible solution is to extract this latter from the bulk of a melted gallium, which is the region not reached by the diffusing oxygen. The oxide layer that is formed during the oxidation process has a lower density with respect the pure liquid gallium and therefore it moves upward by convection giving rise to a covering oxide layer. This procedure is the one followed at ISTTOK to study the hydrogen retention in gallium samples exposed to ISTTOK plasmas [34]. This work takes inspiration from the this latter paper, starting from the construction of the experimental set-up presented in Chapter 4.

2.2.6 *Corrosion by Liquid Gallium*

One of the shortcomings of gallium is its very high corrosion activity on most of the metals since these latter are highly soluble in liquid gallium.
Corrosion induced by any liquid metal can be described by one of the following phenomena:

1. Pure metal dissolving in the liquid metal;
2. Liquid metal and pure metal forming the intermetallic compound. For most metals, the intermetallic compound is of the form MGa_3 or MGa_4 [35].

Luebbers and Chopra [36] studied the corrosion behaviour of liquid gallium on various structural materials used in the atomic reactor and they pointed out that iron, nickel, and chromium react quickly with gallium, while the Nb-5Mo-1Zr alloy has a better corrosion resistance to gallium.

Corrosion is strictly correlated to solubility: metals with high solubility show poor corrosion resistance. The solubility depends on the temperature and for pure metals, the relation can be described by:

$$\log[c_m] = A - \frac{B}{T} \tag{2.3}$$

where c_m is the concentration in atomic percentage, A and B are coefficients, and T is the temperature in Kelvin. Table 2.5 reports the values for A and B for the most

Table 2.5: Solubility data i binary Ga-M systems [37]

Pure Metal	Solid Phase	Temperature Range [K]	**A**	**B**$\cdot 10^{-3}$	C [%], T= 673 K	C [%], T= 773 K
Copper	$CuGa_3$	500 - 700	3.52	1.61	15.0	28
Titanium	$TiGa_3$	600 - 800	2.60	3.12	$9.5\cdot 10^{-3}$	$3.9\cdot 10^{-2}$
Chromium	$CrGa_4$	600 - 800	2.70	3.10	$1.2\cdot 10^{-2}$	$4.9\cdot 10^{-2}$
Manganese	$MnGa_6$	500 - 700	5.40	3.90	0.40	2.3
Iron	$FeGa_3$	500 - 700	4.00	3.85	$1.9\cdot 10^{-2}$	0.11
Cobalt	$CoGa_3$	500 - 700	3.50	3.10	$7.8\cdot 10^{-2}$	0.31
Nichel	$NiGa_3$	500 - 700	2.52	1.85	0.59	1.35

commonly used metals in nuclear reactors; whereas Figure 2.3 shows the solubility curves for the same metals.

The same article written by Luebbers and Chopra [36] reports that, in general, corrosion rates of alloy steels decrease as the chromium percentage increases; whereas the presence of nickel seems to have no remarkable effect on corrosion. Moreover, it is underlined that the addition of aluminium to nickel-chromium steels enhances the corrosion rates.

A metal which is totally destroyed by liquid gallium, even at room temperature, is aluminium. In the Al-Ga system, liquid Ga quickly penetrates deep into the solid grain boundaries replacing each boundary with a liquid layer. The final result is the brittle intergranular fracture under even modest stresses. This phenomenon is known as Liquid Metal Embrittlement (LME).

Gallium attacks not only aluminium alloys but also copper ones. Tikhomirova, Pikunov, et al [38] studied the interaction of liquid gallium with copper at 100°C revealing that copper dissolves into gallium forming an intermetallic compound layer. From Table 2.5, it's clear that the solubility of nickel in gallium is more than 20 times smaller than the one of copper. These two metals are the ones mostly used for CF (standard) flange sealing. Due to the higher corrosion resistance, nickel gaskets are preferred in the experiment carried out in Chapter 4.

Among all the materials that can be used in a fusion reactor, a special focus has to be put on the plasma facing components (PFCs), like tungsten and beryllium which are the chosen ones for ITER. Tungsten reacts slowly at high temperature (T$\sim$800°C)

with the formation of volatile oxides; whereas beryllium starts to be corroded at lower temperatures (T∼600°C).
Luebbers and Chopra [36] have carried out some more tests on structural materials for ITER-like Type 326 SS, Inconel 625, nickel 270, pure chromium and Nb-5 Mo-1 Zr alloy. The results obtained show that at temperatures higher than 400°C all these materials are attacked by gallium and, in general, the corrosion occurs primarily by dissolution and then, by formation of metal/gallium intermetallic compounds. The Nb-5 Mo-1 Zr alloy is the material that has showed the highest corrosion resistance in static gallium: as an example, at 400°C the corrosion rate for this latter was 0.03 mm/yr, whereas for Type 316 SS and for Inconel 625 were 4.0 and 0.5 mm/yr respectively.

The compatibility of steel with gallium was studied by Barbier and Blanc [39]. They carried out their experiments taking into consideration 1.4914 martensitic steel and 316 L austenitic stainless steel in presence of static liquid gallium at isothermal conditions (T∼400°C). The final results showed that these materials are severely attacked by the liquid metal underlining that, for further applications, these alloys

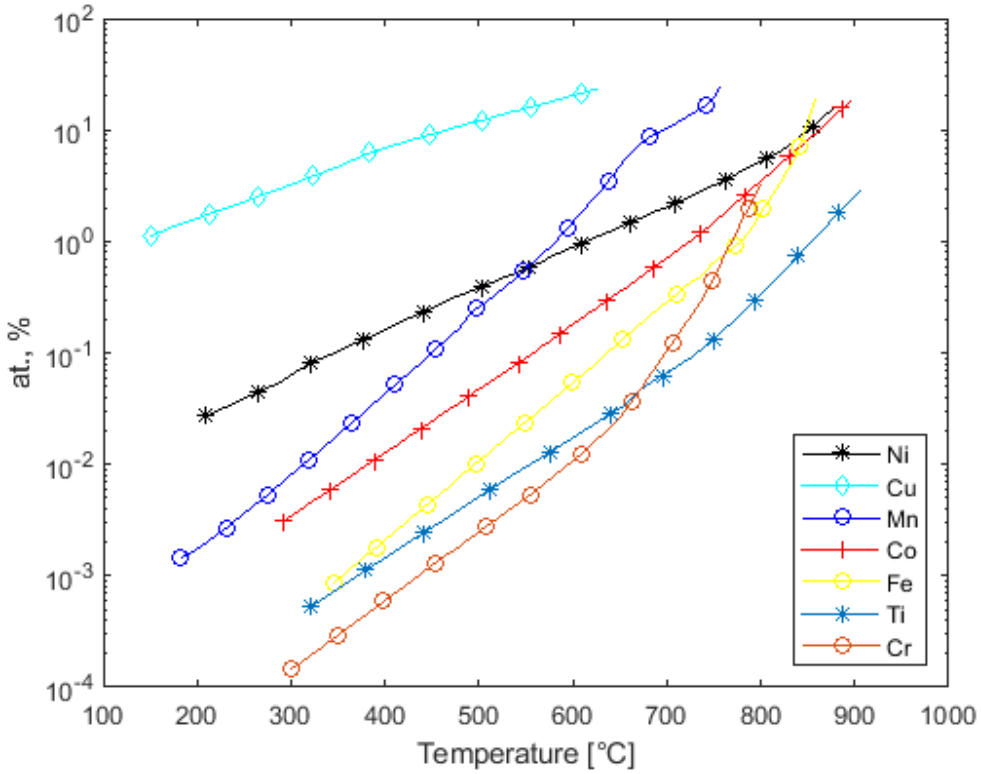

Figure 2.3: Solubility of pure metals in gallium at 200 - 900 °C [37]

must be coated with a stable metal oxide to prevent corrosion.

In another article [40] it was investigated the effect of liquid gallium on four thermoplastics: two semicrystalline (high-density polyethylene and polypropylene) and two amorphous (polystyrene and polymethylmethacrylate). The results showed no interaction between the liquid metals and the plastics even at temperatures close to their melting points and after these materials have been stored in these conditions for several days.

Corrosion of the PFCs by liquid gallium can be a big issue due to the release of the impurities in the melt with a further change of the cooling properties. In order to avoid this, a filtering system must be used to clean gallium. Taking into consideration all the pipes needed to transport gallium to a heat exchanger unit, it has been estimated that about 2800 m^2 total surface of ITER divertor would be exposed to gallium corrosion.

Lastly, another phenomenon, that should be taken into consideration in order to use gallium as a liquid metal coolant, is the wetting of the backing plate material by liquid gallium. The concept of wetting is going to be the main focus of Chapter 3.

3

WETTABILITY

The topic of wetting has received deep interest from both fundamental and applied points of view. In recent years, there has been an increasing interest in the study of wetting of solid surfaces by liquid metals due to their potential applications. A possible one is in the fusion research framework: the idea is to use the liquid metals as PFCs with a cooled structure called capillary porous system (CPS) through which liquid metals should diffuse thanks to the capillary force. The final result is the wetting of the metallic structure by liquid metals.

The process of wetting a solid by a liquid has a great technological importance since it is involved in a large number of biological, industrial, manufacturing and fabrication processes, like printing, painting cleaning, coating, soldering and brazing. More in general, wettability refers to the tendency of a liquid to spread on a solid substrate. Spreading is a physical process through which the area of the solid surface covered by a drop of liquid increases with time.
Wetting can be classified into *non-reactive* and *reactive wetting*.
The *non-reactive wetting* occurs when the liquid spreads on a substrate with no reaction/absorption of the liquid by the substrate material, and some examples are the spreading of water or polymeric liquids on glass or metals. On the other hand, the *reactive wetting* is characterized by the reaction between the liquid and the substrate: the spreading of solder on Copper substrate is an example of this type of wetting.

In the first Section of this Chapter, the non-reactive wetting is described giving the different definitions of contact angle and describing the thermodynamic conditions that allow wetting. In the second Section, the reactive wetting is presented into details. The factors and variables that affect wetting are briefly summarized in the third Section, whereas in the fourth one, the concept of capillary action is described and the Laplace pressure equation and capillary pressure equation are derived. The most used and efficient methods to measure the contact angle are presented in Section

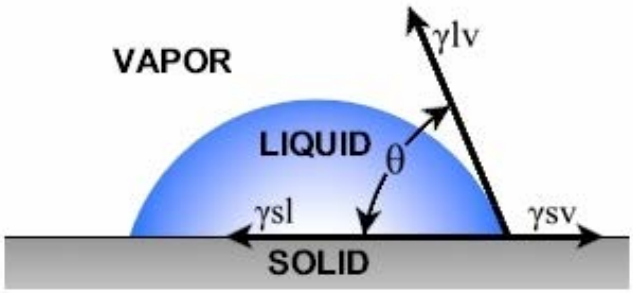

Figure 3.1: Equilibrium contact angle [41]

5. Finally, the focus in Section 6 is on wetting by Liquid Metals: after a comparison between non-reactive and reactive wetting, the concept of capillary porous system (CPS) is presented and described.

3.1 NON-REACTIVE WETTING

3.1.1 *Contact angle*

The aptitude of a non-reactive liquid to wet a flat, smooth and chemically homogeneous solid surface is described by the Young's contact angle θ, a unique characteristic of a solid S–liquid L–vapour V system (Figure 3.1).
At equilibrium, the spreading of the liquid drop on the surface ceases and the equilibrium contact angle θ can be derived from Young's equation:

$$\gamma_{sv} - \gamma_{sl} = \gamma_{lv} \cos(\theta) \tag{3.1}$$

where γ_{sv} is the surface energy (tension) of the solid phase, γ_{lv} is the surface energy of the liquid phase and γ_{sl} is the interfacial surface tension. Eq. 3.1 can be viewed as force balance in the horizontal direction as shown in Figure 3.1. Equilibrium contact angle θ is also known as *static contact angle*.

Another important concept that should be defined is the *work of adhesion* W_{sl}, which is the reversible work to separate a solid and a liquid initially in contact and to bring them at an infinite distance. The French scientist A. Dupre defined the work of adhesion for a liquid and solid combination at constant T and P as follows:

$$W_{sl} = \gamma_{sv} + \gamma_{lv} - \gamma_{sl} \tag{3.2}$$

By combining Young's equation 3.1 with the work of adhesion equation 3.2, Young-Dupre's equation is derived:

$$W_{sl} = \gamma_{lv}(1 + \cos(\theta)) \tag{3.3}$$

For a given value of γ_{lv}, the contact angle increases as the adhesion between the liquid and solid decreases.

According to Eq. 3.3, the intrinsic contact angle θ is a function of both the adhesion and the cohesive forces. The first forces are the ones that develop between molecules of different types. In the case of a liquid-solid-vapour system, they are expressed by W_{sl}: the work of adhesion tends to increase the common area improving wetting. On the other hand, the cohesion forces are forces between molecules of the same type. Cohesive forces between molecules cause the surface of a liquid to contract to the smallest possible surface area. This general effect is called *surface tension* γ_{lv}. Molecules on the surface are pulled inward by cohesive forces, reducing the surface area. Molecules inside the liquid experience zero net force, since they have neighbours on all sides. If there is strong adhesion to the substrate surface and weak cohesion within the liquid, there is a high degree of wetting. Figure 3.2 illustrates the different behaviours of the liquid on a solid substrate:

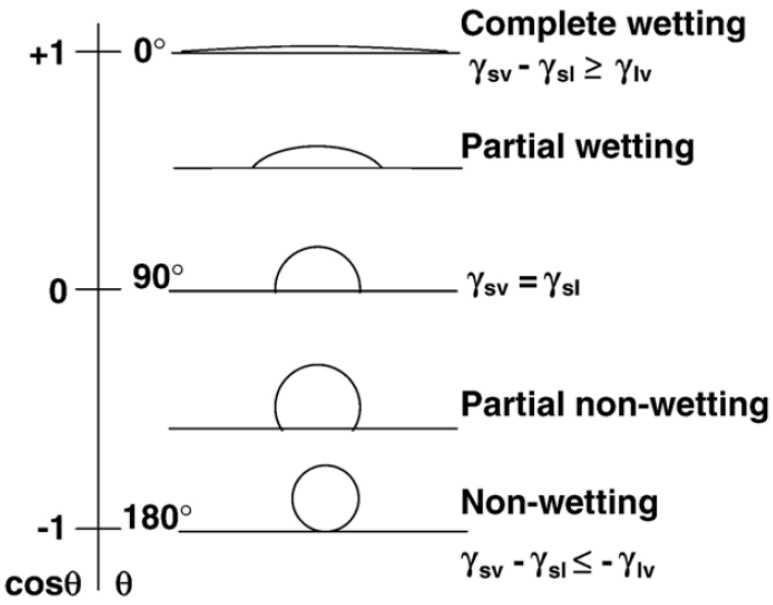

Figure 3.2: Liquid drop on a solid substrate under various wetting conditions [42]

- $\theta = 0°$: complete wetting conditions are reached and $W_{sl} = 2\gamma_{lv}$. The drop has no equilibrium configuration since it tends to spread completely on the solid.

- $0 < \theta < 90°$:there is partial wetting. The liquid wets the solid hydrophilic surface;

- $\theta \geq 90°$: in this case the surface is hydrophobic and the liquid is considered as non-wetting the solid. In such cases, the liquid drops tend to move on the substrate surface without entering into pores or holes by capillary action

To sum up, good wettability is reached when γ_{lv} is as large as possible while γ_{sv} and γ_{sl} are as small as possible.

All the previous equations are valid under the assumptions of non-reactive liquid spread on an ideal surface, which means physically and chemically inert, smooth, homogeneous and rigid. Unfortunately, these conditions are quite rare in reality. In order to take into consideration all the possible situations that can give rise to different contact angles, a variety of contact angle has been defined. The *equilibrium contact angle* or *Young's contact angle* θ_0 is formed at the 3-phase interface, hereafter named also triple line, under equilibrium conditions during the wetting of an ideal solid surface by a nonreactive liquid. It can be determined by balancing the surface tension forces under the assumptions of an ideal surface and thermodynamic equilibrium conditions. If no oxide or any other film/contaminant cover the substrate surface, the equilibrium contact angle is termed as *intrinsic contact angle* θ_y. Turning to real surfaces, a range of contact angles has been observed. The contact angle obtained when a liquid drop is placed on a real surface is known as *apparent contact angle* θ. The apparent contact angle obtained on a rough but homogeneous surface is generally

Table 3.1: Types of contact angles [42]

Contact angle	Definition
Intrinsic, θ_y	Contact angle made by the liquid with an ideal solid surface.
Equilibrium, Young's. θ_0	Contact angle obtained by Eq. 3.1
Apparent, θ	Contact angle on a real solid surface
Wenzel, θ_w	Apparent contact angle obtained on a rough and homogeneous surface
Composite (Cassie), θ_c	Contact angle obtained on a smooth composite surface
Advancing, θ_a	Contact angle measured when the interface is advancing toward the vapour phase
Receding, θ_r	Contact angle measured when the interface is receding away from the vapour phase

referred to Wenzel angle θ_w. Table 3.1 summarizes the main contact angles [43], [44], [45].

3.1.2 *Contact angle hysteresis*

All the previously mentioned angles are classified as static contact angles but, the phenomenon of wetting is more than just a static state. Contact angles defined when the liquid drop is still moving on the solid surface are termed as *dynamic contact angles*. An example of the dynamic contact angle is when a drop slides on an inclined surface (Figure 3.3): the gravity deforms the drop which forms an asymmetric shape. When the drop starts to slide on the tilted surface, the contact angle in the front reaches the maximum value (θ_a), whereas the back angle shows the minimum value(θ_r). The existence of multiple contact angles for a single drop is called as *hysteresis of contact angle*. The largest and the smallest among them are called *advancing* (θ_a) and *receding contact angle* (θ_r) respectively. The difference between these two contact angles is named *hysteresis* H:

$$H = \theta_a - \theta_r \tag{3.4}$$

The phenomenon of hysteresis can originate also from surfaces that have properties different from the ideal ones. As a matter of fact, real surfaces are not smooth, homogeneous, isotropic and non-deformable: the actual microscopic variations of slope on the surface create barriers that pin the motion of the drop and alter the macroscopic contact angles. Therefore, the surface roughness and heterogeneity, the impurities adsorbed on the surface, the swelling of the surface, etc. play the role of generating hysteresis. The polishing of the surface decreases this phenomenon [42], [43], [45].

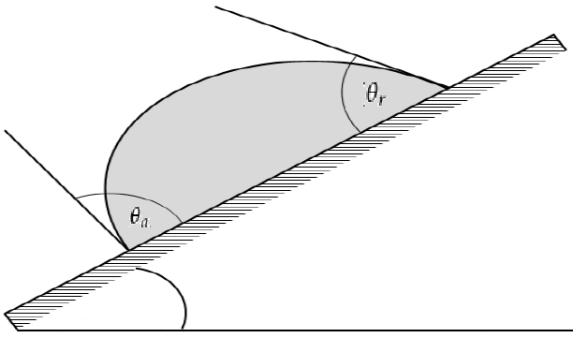

Figure 3.3: Hysteresis of contact angle of a drop on an inclinated surface [43]

3.1.3 *Thermodynamics and kinetics of non-reactive wetting*

The formation of a new interface between solid and liquid is determined by the minimization of the total energy of the system. Therefore, for an ideal surface, the Young's equation 3.1 can also be derived by using the energy minimization aproach. When a drop of liquid is placed on a solid surface, there is a change in the area of covered solid ΔA which is followed by a change in surface free energy ΔG^s as follows:

$$\Delta G^s = \Delta A(\gamma_{sl} - \gamma_{sv}) + \Delta A\gamma_{lv}cos(\theta - \Delta\theta) \tag{3.5}$$

At equilibrium:

$$\lim_{\Delta A \to 0} \frac{\partial G^s}{\partial A} = 0 \tag{3.6}$$

which combined to Eq. 3.5 leads to the Young's equation 3.1 [42].

Wolansky and Marmour [46] carried out an extensive thermodynamic treatment of contact angle equilibrium on real surfaces showing that multiple contact angles are possible on rough or heterogeneous surfaces. In case of a homogeneous rough surface, they derived that the apparent contact angle θ is the difference between the local intrinsic contact angle (θ_y) and the angle the solid surface makes with the x-axis ($\alpha(x)$), where the x direction is along the solid surface and y is perpendicular to it:

$$\theta = \theta_y - \alpha(x), \quad \text{for} \quad \alpha < \pi/2 \tag{3.7}$$

$$\text{or} \quad \theta = \theta_y - \alpha(x) + \pi, \quad \text{for} \quad \alpha > \pi/2 \tag{3.8}$$

The surface roughness can be expressed as:

$$r(x) = \mid \cos(\alpha) \mid^{-1} \tag{3.9}$$

Instead, for smooth but chemically heterogeneous solid surface, the apparent contact angle is always equal to the local intrinsic angle at the contact line:

$$\cos(\theta) = \cos(\theta_y)(x) \tag{3.10}$$

In order to better describe the wetting phenomenon, also the kinetics of contact line movement should be taken into consideration. When a liquid drop starts spreading on a flat surface, the contact angle θ relaxes from its initial value to its equilibrium value. Usually, the dynamic contact angle is expressed as a function of time/velocity. Classical models for spreading kinetics in inert systems account for surface tension

and gravity as driving and viscous dissipation as restraining forces.

In the case of a non-metallic drop spreading on a solid surface, the wetting kinetic data can be empirically correlated by the power law equation:

$$A = kt^n \tag{3.11}$$

where A is the measured liquid-solid contact area, k and n are empirical constants and t is the time. Another possible equation is:

$$A' = k\tau^n \tag{3.12}$$

where A' is the dimensionless drop base area normalized with respect to $V^{\frac{2}{3}}$, τ is the dimensionless time equal to $\frac{\sigma t}{\mu V^{\frac{1}{3}}}$, V is the drop volume, σ is the liquid surface tension and μ is the liquid viscosity. It has been demonstrated by several experiments, that the value of n is in a range of 0.2 - 0.3 for dimensionless drop base area. The assumption behind previous relations is that the substrate is not only inert but also smooth and homogeneous. The models have been extended to take into consideration real surfaces. Other models have been developed to describe the spreading of a inert metallic drop (Subsection 3.6.1) [42].

3.2 REACTIVE WETTING

The wetting process during which the interfacial reactions lead to the formation of continuous layers of a new compound is known as *reactive wetting*. In reactive systems, wetting frequently occurs with an extensive chemical reaction which leads to the formation of a continuous layer of a new compound at the spreading liquid/reactive substrate interface. As a consequence, the rate of spreading is influenced by the reaction between spreading liquid and reactive substrate material.

3.2.1 *Thermodynamics and kinetics of reactive wetting*

In reactive wetting, the wetting is characterized by material transport at the solid/liquid interface where the chemical reaction occurs.
From a thermodynamic point of view, the wetting is possible only if ΔG_r interfacial reaction is negative.

Turning to kinetics, reactive wetting kinetics is affected by different phenomena, like diffusion, convection, deoxidation, etc. Therefore, a single function can hardly describe the full range of behaviours that can result from the previous processes. Moreover, the final wetting rate depends on the controlling process. Researchers have marked and identified five different stages in a reactive wetting:

1. initial rapid spreading stage. This first stage is similar to the one observed for the non-reactive wetting and it can be described by the Young's equation 3.1;
2. initial quasi-equilibrium stage;
3. an interfacial front advancing stage;
4. a following continuous decrease in drop height stage;
5. a final wetting equilibrium stage.

However, no theoretical models are developed to describe complete reactive wetting phenomenon; only empirical relations that fits the experimental results are used [42], [47].

3.3 FACTORS AFFECTING WETTING

Wetting of a solid substrate by a liquid is a highly complex phenomenon which depends on different factors. The main important ones are listed below:

1. *Substrate surface roughness*: The roughness affects wetting modifying the true contact angle by adding an interfacial area for the spreading liquid. The effect of roughness was studied by Wenzel [48] who proposed the following relation:

$$\cos(\theta_w) = r\cos(\theta_0) \tag{3.13}$$

where θ_0 is the equilibrium contact angle, θ_w is the apparent contact angle on a rough surface a r is the average roughness ratio. For ideally smooth surfaces, r is equal to one, whereas for rough surfaces it is always greater than unity. For equilibrium contact angles θ_0 less than 90°, θ_w decreases as the roughness increases (the hydrophilic behaviour of the surface is enhanced); whereas for $\theta_0 > 90^\circ$ apparent contact angle and roughness are directly proportional (the hydrophobic behaviour of the surface is enhanced).
In non-reactive systems, sharp defects can pin the triple line at positions far from the equilibrium. Moreover, at a very high value of roughness, air or

vapour can be trapped giving rise to a composite surface. In reactive systems, the roughness has an additional effect that should be taken into consideration: the asperities and grooves can enhance the local reaction, diffusion, adsorption, nucleations, etc.

2. *Heterogeneity of the surface*: a solid substrate is defined heterogeneous when it contains a dispersion of particles or it is polycrystalline. The equilibrium contact angle θ_C on the heterogeneous surface is given by Cassie's equation:

$$\cos(\theta_C) = f_\alpha \cos(\theta_\alpha) + f_\beta \cos(\theta_\beta) \tag{3.14}$$

where f_α and f_β are the fraction of the surface occupied by the the surface type α and β having contact angles θ_α and θ_β respectively [49].

3. *Flux*: Fluxes are chemically and physically active phenomena which promote wetting of metal surfaces by the spreading liquid by breaking and removing the oxide film that can arise on the top of the surfaces. In wetting processes, fluxes have two major functions:

   - Chemical function to keep the surface clean by breaking oxide films and by protecting the surface from further oxides.
   - Physical function to remove reaction products from surfaces allowing the spreading liquid to have better contact with the surface.

   Fluxes are mainly used in soldering processes since the reactive surfaces are highly susceptible to contamination through adsorption, reaction and diffusion processes [42].

4. *Temperature*: Temperature affects several of properties of a liquid, such as viscosity, surface tension, oxidation behaviour, reaction rate, etc. The rise in temperature enhances the wettability since the viscosity and the surface tension decrease. Temperature speeds up the wetting process also in the case of reactive wetting since the diffusion rate increases, and so the reactivity between the liquid and the solid substrate, with the rise in temperature.

5. *Atmosphere*: It has been demonstrated that the decrease in oxygen content in the atmosphere allows the wetting to start at lower temperatures. Moreover, an inert atmosphere and/or vacuum conditions can hinder the oxidation process improving wetting. Reducing the oxygen content decrease the impurities that can deposit on the substrate and hinder the oxidation of both the metal and the solid surface. A feasible inert atmosphere to displace oxygen is nitrogen

since it is inert and chemically non-reactive with most of the metals, with the exception of lithium. Nitrogen is used especially in the solderable process in order to prevent oxidation of the metal surface. In the set-up constructed and exploited to carry out this work the chosen condition is vacuum since the final aim of liquid gallium is to be used in fusion reactors that work under vacuum.

6. *Liquid properties*: viscosity, surface tension and density can affect the wetting process. From Young's equation 3.1 it's clear that a better wetting is reached when γ_{lv} is low. Some surfactants can be used to reduce liquid surface tension. Moreover, the spreading activity depends also on the viscosity of the liquid: higher viscous dissipation reduces the rate of spread, therefore higher the viscosity smaller is the rate of spread.

3.4 CAPILLARY ACTION

In the last few decades, the contact angle has been mainly correlated to the concept of wetting. Miller [50] underlined that the contact angle is not the cause of wetting but a consequence of it. The term "contact angle" has a different meaning, like intrinsic contact angle, equilibrium contact angle, advancing and receding contact angle, as it was shown in Table 3.1. It has been demonstrated that the dynamic advancing contact angle depends on the liquid penetration [51].

When a liquid comes in contact with a small passage such as a tube of small cross-sectional area, like the openings in a porous material, it will rise due to the capillary effect. Liquids that rise in porous materials are said to wet the material, if not liquids are said not to wet the material.

In porous media, approximating a pore as a capillary tube, the surface tension γ of the liquid acts along the tangent to the liquid surface at the point of contact. This force can be resolved into two components: the vertical one ($\gamma_{lv}\sin(\theta)$) and the horizontal one ($\gamma_{lv}\cos(\theta)$) (Figure 3.4). The two horizontal components have the same modulus and direction but act in the opposite versus, therefore, the unbalanced vertical component $\gamma_{lv}\sin(\theta)$ is the one responsible for the upward movement of the liquid. The liquid penetrates into a pore until the equilibrium is reached. This equilibrium condition is reached when the force that pulls up the liquid (adhesion force) is balanced by the one that pulls it down (weight of the fluid) [52]:

$$F_{up} = F_{down} \tag{3.15}$$

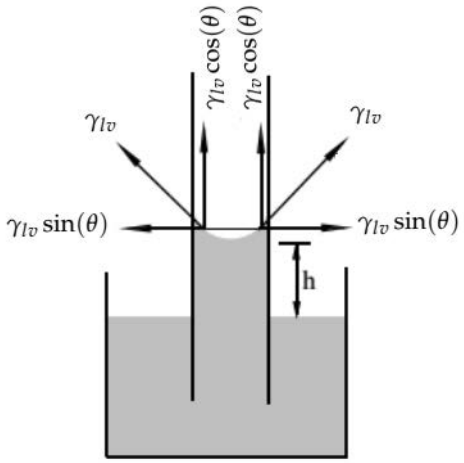

Figure 3.4: Force acting on a liquid in a capillary tube [52]

If r is the pore radius, the length along which the surface tension acts is $2\pi r$. Therefore, the upward force can be expressed as:

$$F_{up} = A_T(2\pi r) \tag{3.16}$$

where A_T is the *adhesion tension* that, taking into consideration the Young's equation 3.1, can be defined as:

$$A_T = \gamma_{sl} - \gamma_{sv} = \gamma_{lv}\cos(\theta) \tag{3.17}$$

Hence total upward force is:

$$F_{up} = \gamma_{lv}\cos(\theta)(2\pi r) \tag{3.18}$$

On contrast, the weight of the liquid acts vertically downward. If m is the mass of the liquid, V its volume, ρ its density, and (πr^2) the cross-section of the pore, the downward force can be expressed as:

$$F_{down} = mg = V\rho g = \pi r^2 \rho g \tag{3.19}$$

where h is the maximum height reached by the liquid in the pore. Substituting into 3.15 equations 3.18 and 3.19, an expression for the maximum height h is obtained :

$$h = \frac{2\gamma_{lv}\cos(\theta)}{\rho g r} \tag{3.20}$$

When two immiscible fluids are in contact with each other an interface arises between them from interfacial tension effects. The *Laplace pressure* can be defined as the pressure difference between the inside and the outside of the curved interface.

Taking into consideration a system characterized by a spherical surface that divides the inside material β from the outside material α (i.e air bubble inside water), the pressure inside the droplet is increased by an amount equal to ΔP due to the surface tension that is pulling in on the surface of the droplet. The relation between ΔP and the surface tension γ can be studied by using the differential of the Helmholtz function (F):

$$dF = -PdV - SdT + \gamma dA \tag{3.21}$$

where γdA is the additional term of energy due to the surface tension. In order for the bubble not to shrink, the pressure inside must be greater than the pressure outside. Therefore, the focus is only on this difference in pressure ΔP. Considering that the temperature is constant and that the system is in equilibrium, the previous equation can be simplified into:

$$0 = -\Delta P dV + \gamma dA \tag{3.22}$$

Solving it for ΔP and assuming the Volume of the droplet equal to $\frac{4}{3}\pi r^3$ and the Area of the droplet equal to $4\pi r^2$:

$$\Delta P = \frac{2\gamma}{r} \tag{3.23}$$

which is called the *Laplace pressure* for spherical shapes [53], [54].

When the two immiscible fluids are in a porous media, one of them preferentially wets the tube surface and it is called the *wetting* fluid, the other fluid is the *non-wetting* fluid. The pressure difference between the two fluids is called *capillary pressure* P_c and it can be expressed as the difference between the pressure in the non-wetting phase and the pressure in the wetting phase:

$$P_c = P_{nw} - P_w \tag{3.24}$$

In case of a water-gas air, the *wetting* fluid is the water, whereas the *non-wetting* fluid is the air. An expression for the capillary pressure can be derived by the following force balance, assuming that the small pores can be approximating to capillary tubes:

$$(P_{nw} - P_w)(\pi r^2) = P_c(\pi r^2) = \gamma_{lv}\cos(\theta)(2\pi r) \tag{3.25}$$

where (πr^2) is the cross-sectional area of the pore and $(2\pi r)$ is the circumference. Therefore:

$$P_c = \frac{2\gamma_{lv}\cos(\theta)}{r} \tag{3.26}$$

This final equation is the most common used variation of the Laplace pressure equation 3.23 [53], [54].

3.5 METHOD TO MEASURE CONTACT ANGLE

3.5.1 *Sessile drop method*

One of the most common methods for measuring the contact angle is the sessile drop method: a liquid drop is deposited on a solid surface and the angle between the solid surface and the tangent to the drop profile at the drop edge is measured. The images of the spreading sessile drop are captured and processed. The image can be analysed either by eye with a protractor or by an image analysis software.

Bigelow et al. [55] invented and implemented an instrument able to measure contact angles of different liquids on polished surfaces. This instrument is called *telescope-goniometer* and its first commercial version came out in the early 1960s thanks to W. A. Zisman. The machine is usually characterized by a horizontal stage to mount the substrate, a micrometre pipette to form a liquid drop, an illumination source, and a telescope equipped with a protractor. A camera can be added to take photographs of the drop profile whenever the user needs. Despite the simplicity of this technique and the small drops and solid surfaces required, there are lots of drawbacks to take into consideration. First, there is a high risk of impurities due to the small size of the drop and substrate. Secondly, the measurement is strongly affected by the user in the assignment of the tangent line. This negative aspect affects more the analysis in case of an almost flat drop. Thirdly, this method cannot be applied if the contact angle measurement should be carried out under vacuum.

The previously mentioned method is used to measure a static contact angle. In order to measure the contact angle hysteresis, two different approaches can be used. In the first one, a small droplet is displaced on the substrate and its volume is gradually increased by using a needle brought close to the surface. The change in volume is recorded in order to measure the advancing contact angle. The receding angle is measured following the same procedure but by decreasing gradually the volume. In the second method, the droplet is placed on a substrate which is gradually tilted until the drop starts to move. The advancing contact angle is measured in the front of the droplet and the receding angle is measured at the back of it, at the same time [42], [45].

3.5.2 *Tilting Plate Method*

In this method proposed by Adam and Jessop [56], a solid surface is immersed in the liquid and rotated until a meniscus is formed on both sides of the plate. Then it is tilted until the meniscus becomes horizontal only on one side: the contact angle is measured on this side and it is the angle formed by the horizontal line of the meniscus and the surface plane of the plate. The main drawbacks of this method are the difficult procedure and the difficulties in further measurement. Moreover, the liquid contamination can affect a lot the final result. This latter issue can be improved by cleaning the surface and detecting the impurities on the liquid surface.

3.5.3 *Wilhelmy balance method*

The Wilhelmy balance method [57] is used to indirectly measure the average advancing and receding contact angles on solids of uniform geometry. A thin, smooth, vertical and rectangular plate is brought in contact with a liquid of known surface tension and the wetting force on the solid is measured as the solid is immersed in or withdrawn from the liquid. Considering a plate of l width and b thickness (Figure 3.5), the wetted perimeter can be defined as:

$$L = 2l + 2b \tag{3.27}$$

At the three-phase contact line a tension force F_{tens} acts tangentially to the liquid

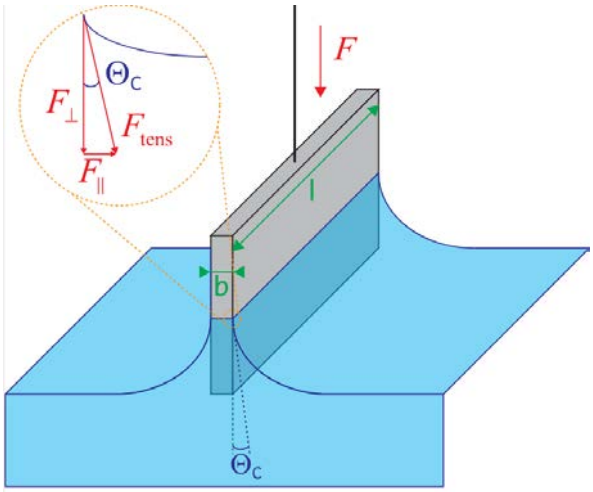

Figure 3.5: Wilhelmy plate with liquid lamella [57]

surface. This force can be split in a parallel force and in perpendicular one to the liquid surface:

$$F_{\perp} = F_{tens} \cdot \cos(\theta) \tag{3.28}$$

$$F_{\parallel} = F_{tens} \cdot \sin(\theta) \tag{3.29}$$

Making a balance on the z-direction, the Wilhelmy equation is derived:

$$\gamma = \frac{F_{tens}}{L} = \frac{F_{\perp}}{L \cdot \cos(\theta)} \tag{3.30}$$

where γ is the surface tension, L the wetted perimeter, and θ the contact angle. The same equation can be used to directly determine the surface tension knowing L and the $F_{\perp}$ and assuming complete wetting ($\cos(\theta)$=0).
As the solid sample is pushed into or pulled out of the liquid, an advancing or receding contact angle can be established, respectively. This method has several advantages over the previously described methods. First, the width and the thickness are the only values required to determine the contact angle and that can be measured with high accuracy. Secondly, the measured contact angle takes already into account the heterogeneity of the sample. Thirdly, this method can be used also in case of dynamic contact angles. Nevertheless, the method also suffers from several drawbacks. The sample must have a uniform cross-section and sometimes it is quite difficult to precisely determine the wetted perimeter due to the anisotropy of the sample. In addition, enough quantity of liquid is required to perform the experiment.

3.5.4 *Capillary rise method*

Capillary rise method is widely used for contact angle determination and it involves monitoring the rate at which a liquid penetrates into a porous media. This method was developed by Washburn [58] and it allows the determination of the radius of the porous media and contact angles of liquid on the solid surface. Washburn's theory was derived starting from Poiseuille's law:

$$Q = \frac{dV}{dt} = \frac{r^4 \Delta P \pi}{8 \eta h} \tag{3.31}$$

where Q is the volume flow rate of a liquid of viscosity η, through a porous of radius r until the height h is reached, when a ΔP pressure difference is given.

The relationship between the liquid volume and height is given by:

$$dV = r^2 \pi dh \tag{3.32}$$

By substitution of Eq. 3.25 and Eq. 3.32 to Eq. 3.31, the Washburn's equation is obtained:

$$h^2 = \frac{r\gamma_{lv}\cos(\theta)t}{2\eta} \tag{3.33}$$

Washburn's equation presents linear dependence of square of height penetration of penetrating liquid in the tube versus time. In case of porous media, Washburn's theory assumes the pores as if they were a bundle of cylindrical capillaries. Capillary radius r is equivalent to the pore radius [45], [59].

3.6 WETTING BY LIQUID METALS

3.6.1 *Non-reactive wetting by liquid metals*

Liquid metals are high cohesion energy liquids, therefore good wetting on a solid substrate can be obtained only if the work of adhesion is high as well, which is possible if the interfacial bond is strong. As a consequence, the solid metals are usually wet by liquid metals thanks to the interfacial metallic bond. Good wetting is also reached on semiconductors such as Si, Ge, or SiC since they have a metallic character near the surface that allows a strong bond. Moreover, liquid metals also wet ceramics such as carbides, nitrides or borides which are characterized by metallic bonds that hold them together. Despite that, the wettability of these solids can be affected by the presence of wetting barriers, i.e oxide films. On the other hand, liquid metals don't wet at all carbon materials (i.e Au on C), iono-covalent oxides (i.e Cu on Al_2O_3) and covalent ceramic (i.e Au on BN).

With regards to the kinetic, De Gennes [60] derived a model that describes the spreading rate of a spherical metallic drop on a smooth and perfectly wetted surface. The spreading rate is controlled by the viscous flow and described by the following relation:

$$R_t^{3n+1} \sim t \tag{3.34}$$

where R_t is the radius of the drop at time t. The model developed by De Gennes leads to m=3.

3.6.2 *Reactive wetting by liquid metals*

Wetting with the formation of a new compound at the interface

Wetting in metal-metal and metal-ceramic systems is often followed by reactions at the solid-liquid interface. Different studies have been carried out on various reactive systems, like Ni-Si alloys on vitreous carbon (C_v) substrates; spreading of Copper on SiC substrates; spreading of pure tin on copper substrates.

An important and remarkable model is the one developed by Eustathopoulos et al. [61] which focuses their studies on the dynamics of wetting in reactive metal-ceramic systems and proposed a Reaction Product Control (RPC) mechanism to describe this latter: the final degree of wetting and the spreading kinetics are controlled by the new compound originated at the interface by the reaction and by the transport of reactive species from the drop bulk to the triple line. In Figure 3.6 the main stages of reactive wetting identified by the model are reported:

1. The liquid drop reacts with the unreacted surface and an initial contact angle θ_0 is obtained;
2. during the transient stage, there is a lateral growth of wettable reaction product layer;
3. a steady-state configuration is reached when the presence of the non-wettable substrate in front of the triple line impede the advance of the liquid. At this point, the dynamic contact angle is the final equilibrium contact angle θ_F.

The spreading time t_{spr} in metal-metal and metal-ceramic reactive systems is in the range $10 - 10^4$s, which is higher than the spreading time observed for non-reactive metals ($t_{spr} \approx 10^{-2}s$). This is due to the fact that the RPC for the spreading rate is the interfacial reaction at the triple line. With respect to the non-reactive wetting,

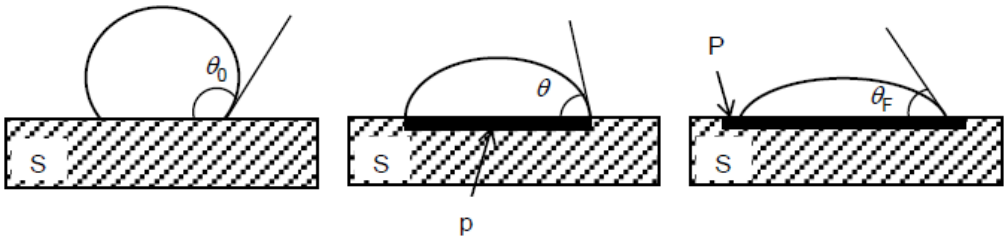

Figure 3.6: Variation with time of the contact angle and drop base radius observed in a metal-ceramic system [61]

where the relevant defect is the 2D interface, in reactive wetting the line defect is the contact line of three phases S, L and V: the liquid has direct access to the solid at the triple line and, as a consequence, the reaction rate at this specific point is three orders of magnitude higher than the reaction rate at the interface far from the triple line where the reaction occurs by slow diffusion through the solid layer. Eustathopoulos et al. [61] pointed out that the reaction rate at the triple line can be controlled by two different phenomena: diffusive transport of reacting species to or from the triple line and local reaction kinetics at the triple line.

In the first case, the Reaction Product Control (RPC) is the reaction kinetics since the diffusion is comparatively rapid. Assuming that the drop composition doesn't significantly change during the reaction and that a steady state configuration is reached at the end, the radius R of the spreading drop can be expressed as a linear function of time:

$$\frac{dR}{dt} = K \tag{3.35}$$

where K is a constant independent of drop volume. As a consequence, the rate of reaction at the triple line and the triple line velocity ($U = \frac{dR}{dt}$) are constant with time. This linear spreading has been observed in many of cases after the initial drop spreading. An example is the spreading of Ni-66.8 at % Si alloy [1] on vitreous carbon at 1200°C. This latter system was studied in detail by Bougiouri and co-workers [62] who showed that the radius of the spreading drop $R(t)$ presents a non-linear increase (from t_0 to t_N) followed a by a linear one (from t_N to t_F) (Figure3.7).
The first stage of the process ($t < t_N$) is characterized by a strong coupling between the local chemical reaction and spreading kinetics due to the direct contact between the liquid and the initial substrate. The contact angle θ_0 is the contact angle of the metal alloy drop on the unreacted substrate, whereas θ_N is the first contact angle corresponding to an interface fully covered by a reaction product layer. The triple line velocity U decreases approaching a limiting value U^* as the initial contact angle θ_0 tends towards θ_N. Therefore, the decrease from θ_0 to θ_N corresponds to a transition from a non-reacted to a completely reacted interface. This first stage is controlled by the local reaction process at the triple line. When θ is equal to θ_N, a second wetting stage starts ($t > t_N$): a steady state configuration is established at the triple line and the reaction rate and the triple line velocity U are constant with time, whereas the drop base radius R linearly grows with time following equation 3.35. The liquid has no longer direct access to the initial substrate surface and the coupling between the

[1] at% signifies atomic percentage, so Ni-66.8at % Si would have 66.8% of atoms in the alloy as Silicon and 33.2% of the atoms in the alloy as Nickel

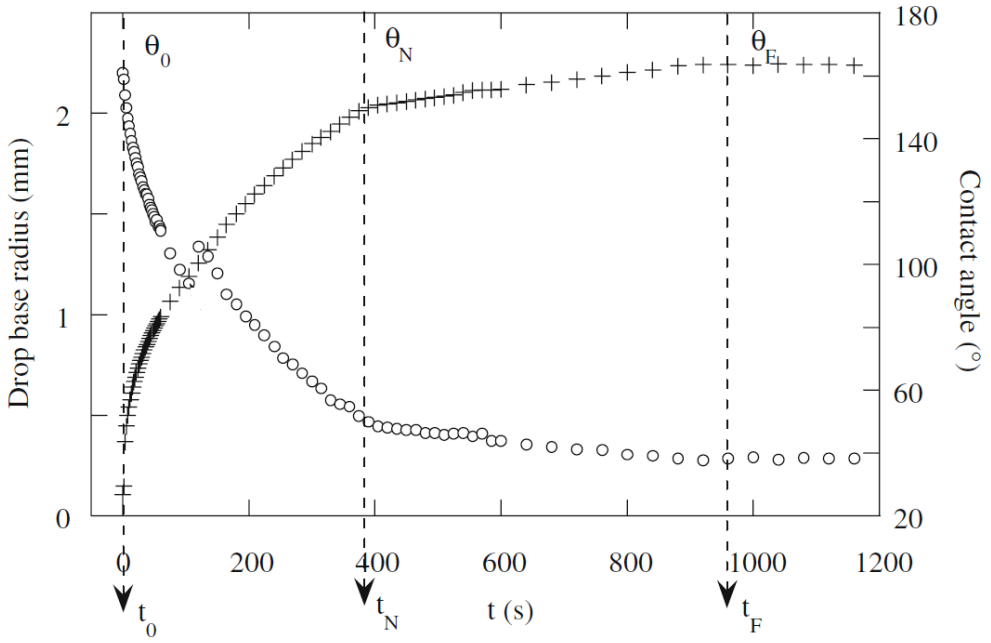

Figure 3.7: Contact angle and drop base radius versus time for a Ni–66.8 at % Si alloy at 1200 °C [62]

local chemical reaction and spreading kinetics is weak: the advance of the liquid is hindered by the presence of a non-wettable surface in front of the triple line. The only way for the reaction to take place is by lateral growth and nucleation of the reaction product particles on the substrate free surface in front of the triple line. This second stage is controlled by the diffusion of the reactive element and it lasts until θ is equal to θ_F, which is the equilibrium contact angle of the metal alloy on the vitreous carbon substrate: at this point, there is no longer coupling between the local chemical reaction and the spreading kinetics and the reaction front advance while the triple line doesn't move.

In the second case, when the local reaction rates are comparatively high, the spreading is limited by the reactants transport from the drop bulk to the triple line. Therefore, the controlling process is pure diffusion: the contact angle decreases with time and so the reaction rate and the rate of movement of the triple line U, as a consequence. Also in this case, the evolution of the drop base radius R can be expressed as a function of time:

$$\frac{dR}{dt} = K(Co, T)\theta \tag{3.36}$$

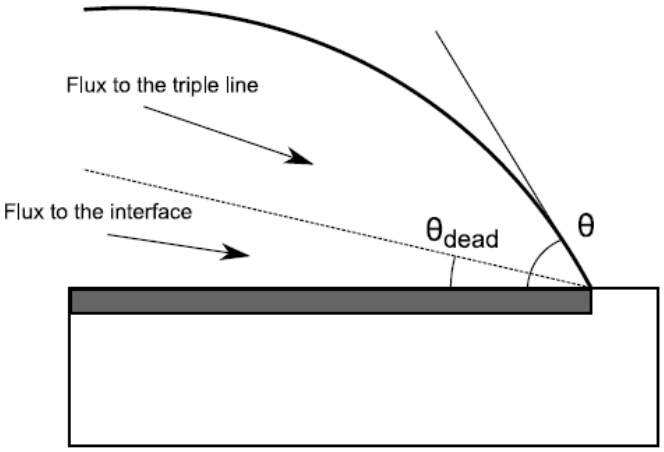

Figure 3.8: Physical meaning of the dead angle [47]

where K is a constant depending on the temperature T and on the concentration of the reactive component in the drop *Co*.
For small drops, that form approximatively spherical cups and contact angles that can be considered nearly equal to $\frac{4V_d}{\pi R^3}$, where V_d is the drop volume, the previous Eq. 3.36 can be integrated into:

$$R^4 - R_0^4 = KV_d t \tag{3.37}$$

This model has been studied by Mortensen, Eustathopoulos et al. [47] and it neglects the convection within the drop. At the end of their simulations, the presence of a *dead-angle* was detected: this angle should be subtracted from the angle θ that appears in Eq. 3.36 since the flux to the triple line delimited by the *dead-angle* is deflected from the triple line and it is consumed on the layer behind the triple line (Figure 3.8).

Eustathopoulos, Mortensen and co-workers [61] affirm that the RPC model is also valid for other types of systems, i.e metal-metal.

Dissolutive wetting

The dissolution of a solid in a liquid is a phenomenon that occurs in many liquid metal-solid metal or metal-ceramic systems. In this case, the liquid metal spread on top of the solid substrate dissolves the substrate that it is wetting. There are two types of dissolutive wetting systems: 1) intrinsically dissolutive systems in which only the dissolution of solid in the spreading liquid occurs; 2) product forming systems in which the formation of a new compound follows the dissolution of the solid in the liquid.
In the first case, considering a liquid A/solid B system where B is highly soluble in

liquid A, the wetting of B results in a first contact angle θ_0 and in further spreading of the liquid on the substrate surface in order to maintain the capillary equilibrium at the three triple line. The final result is the formation of a crater under the droplet and the alteration of the interfacial energies and of the contact line geometry. An example of the intrinsically dissolutive system is the Bi-Sn.
In the second case, the initial dissolution is followed by the formation of a layer of a new compound at the interface that retards the dissolution rate. An example is the spreading of Au-40 at % Ni alloy on ZrB_2 substrates [63].

3.6.3 *Capillary porous system*

As part of the application of liquid metals for fusion reactors, the use of capillary action to counteract disruption and electromagnetic forces have been proposed. Typically a mesh or a porous substrate (Figure 3.9) on top of an actively cooled structure together with a liquid metal reservoir is used in the so called capillary porous system (CPS). The radius of the porous structure or mesh is typically in the sub-mm range (10 - 200 μm) to facilitate capillary action. The rise of the liquid is caused by the pressure difference along the capillary that can be expressed by the previous Equation 3.26. The total height reached by the liquid in the pore can be calculated by Equation 3.20. The wetting of the solid substrate by the liquid is fundamental to have potential alloying, heat-flux resistance and nuclear safety aspects of the substrate. The choice of the material is functional to have a good replenishment of the liquid surfaces as well as a good compensation of the electromagnetic forces applied to the metal by induced currents. In order to understand if a material is able to withstand the heat fluxes, the penetration of a heat pulse into the solid should be estimated by the physical properties of the material itself.

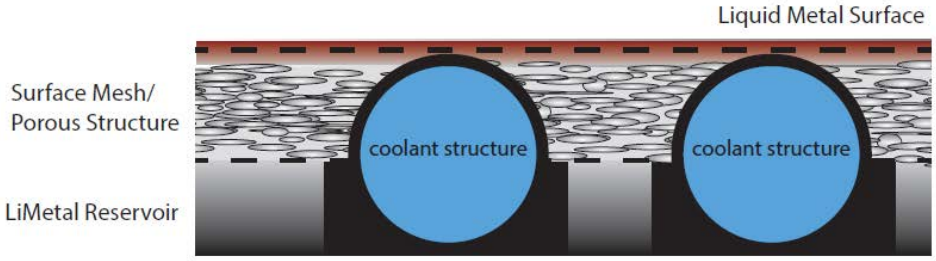

Figure 3.9: CPS Components [20]

4

EXPERIMENTAL SET-UP

Wetting of steels and other materials by liquid metals has been studied for many years, but few experiments have been carried out to study the processes which take place at the solid-liquid interface. It has been tested that factors that influence interfacial composition also affect the solubility rate of the solid, but inadequate control of contamination and inadequate analytical methods of the past have led to confusing and often misleading results. In order to study wetting phenomena in details, ultra-high vacuum (UHV) equipment is required at first to ensure that gallium does not oxide and, in second instance, to maintain clean surfaces for sufficient time reducing almost at zero the number of impurities and oxygen that can react either with the surfaces or with the liquid metal. Therefore, the first task to get meaningful test results is to have high purity starting materials and clean samples. In the first section of this Chapter, the techniques used to clean and treat the surfaces of the stainless steel 316 samples are presented. In the second section, the machine set-up, specifically built up to carry out the contact angle study measurements, is showed and described in details.

4.1 SURFACES TREATMENT

The samples chosen to study the wettability of gallium are stainless steel 316L: type 316L is an austenitic chromium-nickel stainless steel that contains 2 % molybdenum. The molybdenum content increases corrosion-resistance, improves resistance to pitting in chloride ion solutions, and increases strength at high temperatures. Therefore, this material shows higher resistance to gallium corrosion than other types of stainless steel even at temperatures up to 300°C. This aspect is very important since, in the experiment, the temperature of the sample will increase up to values at which the wetting goal is reached.

Table 4.1: Surface Finish and Surface Roughness for Steel

Standard ANSI grit	European (P-Grade)	Median Diameter (microns)	Surface Roughness on Steel (Ra - nm)
60	P60	250	-
80	P80	180	1140
120	P120	106	1050
180	P180	75	880

The first step to carry out the experiment is to clean the surface of the samples. When the solid substrate is heated, impurities present in the bulk can diffuse to the surface where they may react with any adsorbed material already present. Carbon, for example, could react with adsorbed Oxygen to form gaseous oxides. The choice to work under vacuum was primarily made to decrease the impurities content in the atmosphere and, secondly to reproduce the vacuum conditions of fusion reactors: as a matter of fact, liquid metals are envisaged to be employed as PFCs.

There are several different ways to treat a solid surface and the choice depends upon the material to be mechanical prepared and the equipment available. Several methods are commonly used either separately or in combination to treat a given surface. The two different methods used in this work of thesis are grinding and polishing since they are the most used in case of steel.

Grinding removes saw marks and levels and cleans the specimen surface. Proper grinding removes damaged or deformed surface material while limiting the amount of additional surface deformation. This method uses a rotating abrasives paper attached to a disk to remove material, creating a flat surface. The process of making chips with a sharp abrasive grain produces the lowest amount of deformation in the specimen while providing the highest removal rate. For the experiment described in the thesis, the stainless steel samples were ground with Silicon Carbide papers of different grit sizes. SiC abrasive paper is available in all common grit sizes ranging from 60 grit to 1200 grit. The grid size affects the final roughness of the sample surface. Table 4.1 reports the relation between the grit size of the Silicon Carbide paper and surface roughness for steel.
The manual grinding was used not only to clean the surface but also to get different values of roughness. The machine used is the one shown in Figure 4.1 and the procedure is the following: once the desired Silicon Carbide paper has been positioned on the rotating grinder, the running water is turned on. The successive step depends on

Figure 4.1: Manual grinding machine

the desired final result. If only the grinding method is required to get high values of roughness, the specimen is held and moved on the abrasive disc in a figure of eight manner (to ensure even grinding) under running water. The grinding is continued until the saw marks are replaced by uniform scratches on the surface. In the other case, if the grinding is followed by the polishing to obtain a "mirror" surface (very smooth), the specimen is held firmly against the abrasive disc until parallel scratches of the first abrasive paper are obtained. After that, the specimen is rinsed in warm tap water and a finer abrasive paper is used. The samples are held on the disc in a 90°C rotated angle position with respect to the previous one so that scratches are removed. After the last abrasive paper, the specimen is cleaned in an ultrasonic bath before moving on to the polishing step.

Polishing removes the artefacts of grinding but very little stock. It uses free abrasives on a cloth; that is, the abrasive particles are suspended in a lubricant and can roll or slide across the cloth and specimen. The polishing usually follows the finest grinding step. Diamonds are used as an abrasive to accomplish the fastest material removal and the best possible flatness. Diamond polishing abrasives are typically available in 30, 15, 9, 6, 3, 1, and 0.25 μm sizes, in liquid suspensions, pastes, and aerosols. In this work, the manual polishing with lubricant and 1 μm diamond paste was carried out. The size of the diamond paste affects the final roughness of the surface: in theory, if the 1 μm diamond paste is used, a final roughness of 1 μm is

Figure 4.2: Manual polishing machine

obtained. The lubricant is used to enhance the interaction between the abrasive and the specimen, whether the abrasive is fixed or free. The polishing lubricant adheres the abrasive and enables the abrasive particles to roll and slide easily between the paper and the specimen, and uniformly distributes the contact stresses between the paper and the specimen during polishing. The manually polishing steps are as follows: a very small amount of diamond paste and the lubricant are sprayed on the polishing cloth stuck onto the rotating plate. Specimen is polished in a figure of eight manner until the surface is glossy. The used polishing machine is shown in Figure 4.2.

After having treated the samples, its final roughness is studied with the 3D optical profilometer reported in Figure 4.3.

Figure 4.3: 3D optical profilometer

4.2 EXPERIMENTAL SET-UP

High energy surfaces of liquid metals are easily contaminated; therefore care must be taken to maintain clean surfaces while measuring the contact angle. One of the easiest ways to do this is to conduct tests under vacuum conditions, 10^{-4} mbar range or less. It has to be underlined that all the components and materials need to be cleaned before starting vacuum in order to achieve very low pressure values.
In this work, a specific experimental set-up is built up in order to study the wettability of stainless steel 316 by liquid gallium under vacuum conditions. Vacuum was required to reduce the impurities content mainly to hinder the oxidation of gallium in order to get free-oxide gallium and, secondly, to reproduce the vacuum conditions present in a fusion reactor. The breakdown of the oxide film is vital to achieve true wetting in any system since the film present on the substrate surface or spreading liquid will alter the interfacial properties. However, the surface tensions of oxides are significantly lower than those of the corresponding metals. As a consequence, an oxidised liquid metal is expected to exhibit better wetting than the unoxidized one. Nevertheless, the general result observed is a deterioration of wetting by the oxide layer. The main reason for this is that wetting is a complex phenomenon that depends

not only on liquid surface tension but also on surface properties of the substrate. The atmosphere that caused oxidation of liquid solder would definitely cause oxidation of the substrate also. Furthermore, the process will add contaminants to the surface. The net effect is the deterioration of wetting.
The experimental device constructed and exposed in the paper [34] was taken as a reference to design the set-up described below.

The UHV system used in this study consists of a rotary vane pump (Duo 10 M, 1-phase motor [1]) with a pumping speed of up to 12 m^3/h and a turbo-molecular pump with a pumping speed of up to 219.6 m^3/h. The entire structure of the system is constructed from stainless steel 304L and uses oxygen-free copper or nickel gaskets throughout. Nickel gaskets are used only to connect the parts where liquid gallium is always in contact with the gasket or might accumulate during the experiment leading to the corrosion of the gasket itself. Accurate pressure measurements from 10^{-2} to 10^{-8} mbar are made by a penning vacuum pressure gauge mounted in a DN40CF flange located on the left side of the machine, under the flange where the pumps are mounted. Figure 4.4 represents a cross-section of the system with the sensor and the pumps removed, whereas the next Figure 4.5 is a photograph of the implemented experimental set-up.

In order to achieve ultra-high vacuum, all the materials are carefully chosen and the components are cleaned with alcohol in ultrasound bath before being installed. Furthermore, once the set-up is assembled and closed, the system is degassed heating it up at high temperature for 24 hours at about 80°C using heating bands wrapped all around the system, as it showed in Figure 4.5. This last step is repeated every time the machine is opened to change the sample. The final vacuum pressure reached is usually in the 10^{-8}-10^{-7} mbar range in cold state and just above 10^{-6} mbar with the heater, where the samples are mounted, on.

[1] $https://www.pfeiffer-vacuum.com/productPdfs/PKD62712.en.pdf$

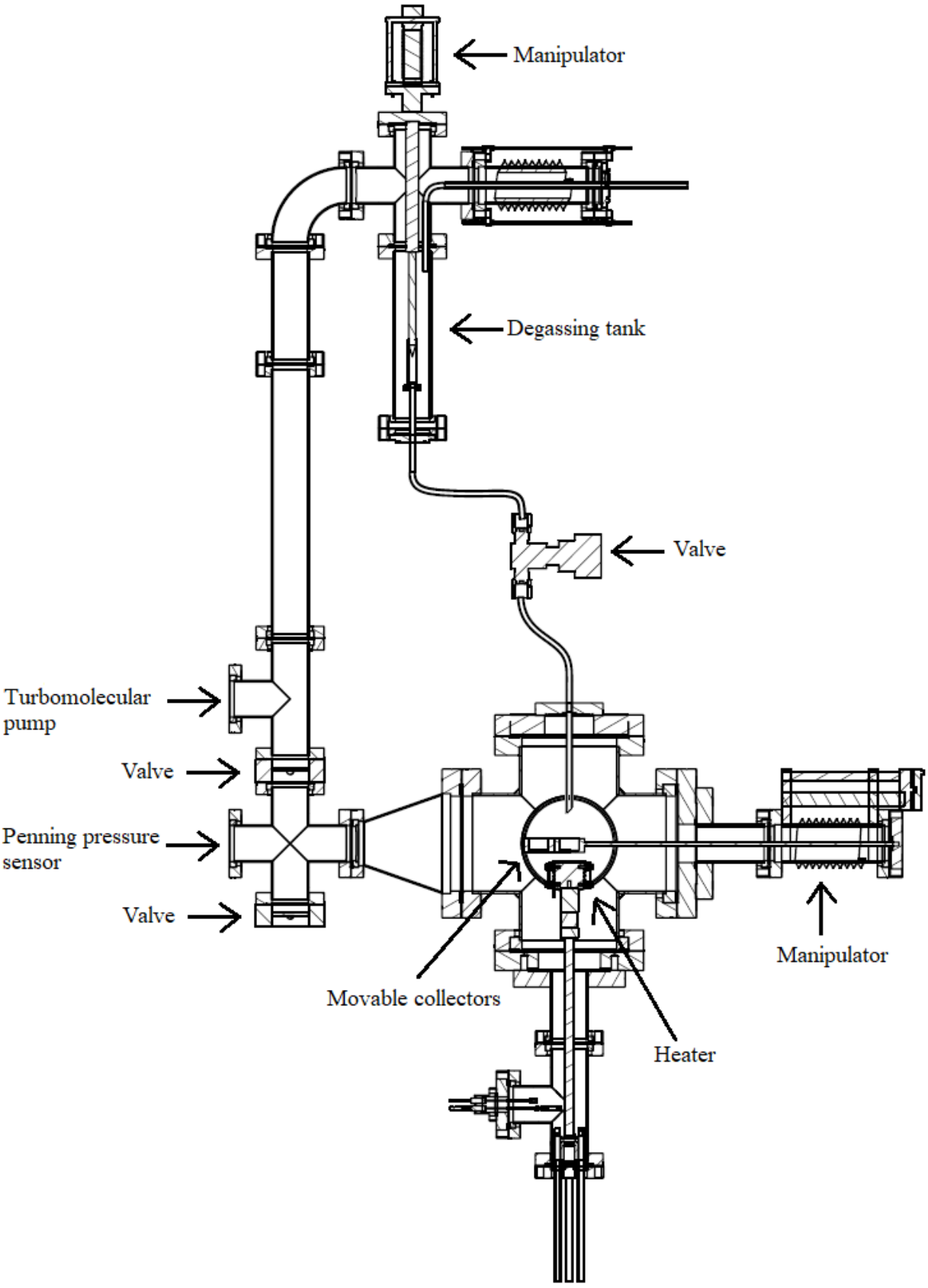

Figure 4.4: Section of the experimental set-up

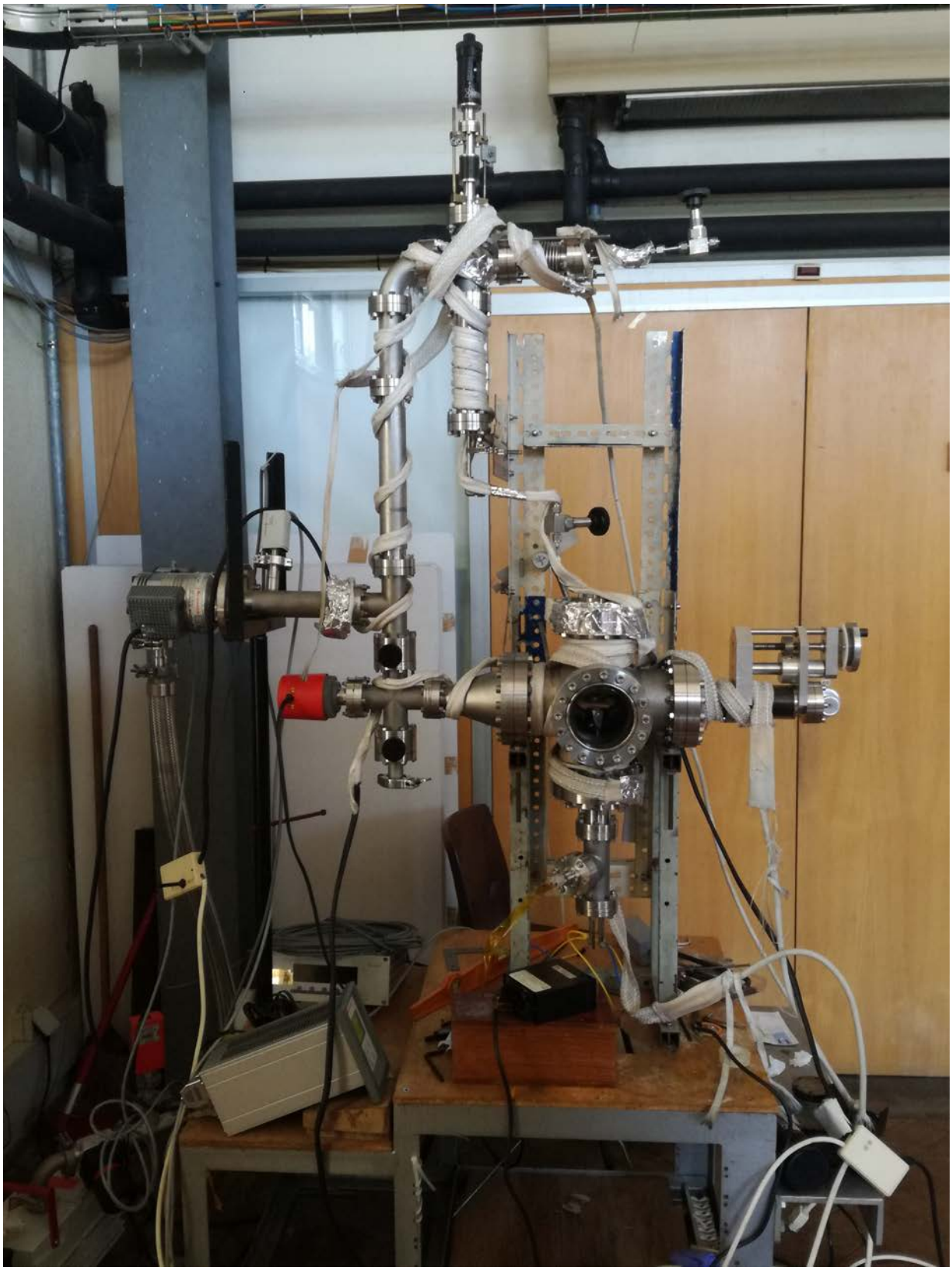

Figure 4.5: Experimental set-up

The top part of the machine (Figure 4.6) is characterized by the gallium injection pipe, a manipulator and a degassing tank where liquid gallium is held. Liquid gallium is inserted in the top-right pipeline and collected in the degassing tank which is a straight connector of 18 cm with DN40CF flanges. The lower part of the tank is sealed by a stainless steel membrane mounted in a 16CF flange. A vanadium rod is located on top of the membrane and it can be moved up and down thanks to a manipulator in order to break the membrane and let gallium flows in a 1\8" pipe of 3 mm outer radius after this latter has been degassed. The degassing process is carried out heating up the gallium tank at a temperature about 200°C for 24 hours by heating bands wrapped all around the machine (shown also in Figure 4.5) in order to separate gallium from its oxides or other intrinsic impurities. The gaskets used for the degassing tank are in nickel since the temperature reached during the degassing process are high enough (∼200°C) to strongly corrode copper.

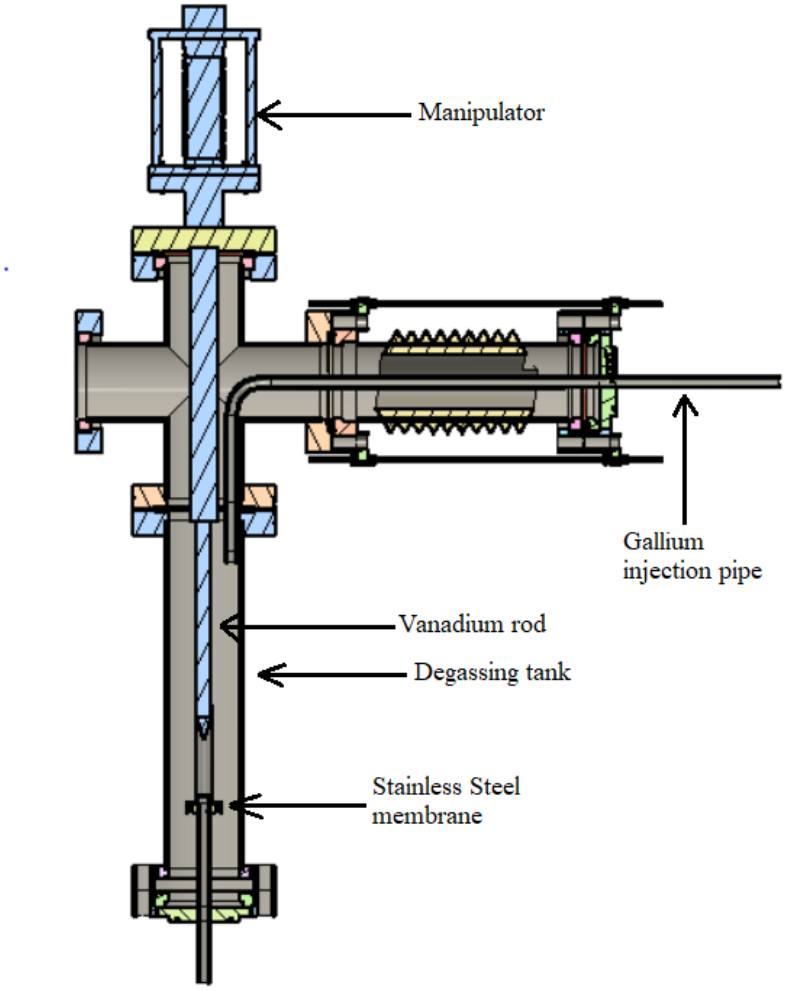

Figure 4.6: Top section of the experimental set-up

Figure 4.7: a) Cap used to insert gallium; b) Bottle of gallium 6N

Liquid gallium is injected in the machine turning off the turbo-molecular pump and connecting a gallium bottle (Figure 4.7b) to the small pipe on the top-right of the experimental set-up. After have estimated the volume of the degassing tank, liquid gallium, pure at 99.9999% (6N), is inserted using the device shown in Figure 4.7a: the bottle containing the Liquid metal is closed by a cap where a pipe and an electrode are mounted. The outside part of the electrode is connected to a multimeter and the electrode is cut in such a way that, when all the desired gallium is inserted in the set-up, the electrical circuit previously short circuited by gallium is opened and the multimeter stops beeping. Gallium is injected in the machine keeping only the rotary pump on. After the injection, gallium is degassed at high temperatures and then the stainless steel membrane is punctured by the rod, taking advantage of differential pressure. The degassing tank is continuously heated at temperatures higher that 30°C in order to keep gallium in the liquid state. Only after this procedure, the valve that separates the degassing tank from the bottom chamber of the experimental set-up is opened and gallium allowed to flow.

The initial gallium flow is received on a first moveable collector of stainless steel 304 in order to collect gallium that might have been contaminated or oxidised by impurities trapped in the walls. The second movable collector, made in stainless steel 304 as well, has a hole of 1.8 mm to create the desired droplet size of gallium. The two collectors are mounted in a manipulator allowed to flow. In Figure 4.8a the

Figure 4.8: a) Collectors mounted in a manipulator; b) the two movable collector: the right one blank and the left one with a 1.8 mm hole

manipulator is shown, whereas a photo of the two collector is reported in Figure 4.8b. The choice of stainless steel 304 is due to the fact that other materials, like brass and copper, can evaporate at the vacuum pressure of 10^{-8} mbar and high temperatures at which they are exposed.

The gallium droplets fall on top of the stainless steel 316 sample. The sample is mounted on top of a heater in order to reach temperatures up to 540°C. A screw and a washer are used to keep the sample in place and to fix the thermocouple on top of the sample surface in order to measure its temperature. The thermocouple used is of type C. A photo and the drawing of the heater are reported in Figure 4.9. The heater is made of a copper cylinder of 3 cm diameter and 3 cm high around which are wrapped 80 cm of thermocoax. The themocoax is an heating element of small diameter. Essentially, the thermocoax is characterized by both thermocouple conductors, insulation and metal protecting sheath. The one used to construct the heater has nickel-chromium as heating element, magnesium oxide as an insulant and austenitic stainless steel 304L as a sheath. The maximum temperature that the thermocoax can withstand is 800°C and the resistivity per centimetre is 72 $\mu\Omega cm$. A stainless steel shield is put around the heater (Figure 4.9a, shown in blue) in order to minimize heat dissipation by reflecting a fraction of the radiated power.. The heater is mounted on a power-feedthrough, characterized by 4 pins, as it is shown in Figure 4.9b. The electrical insulation is ensured by a ceramic cylinder located underneath the heater. Figure 4.9c shows the complete configuration of the heater mounted at the bottom of the experimental set-up with a sample held on the top and the thermocouple kept in place on the sample surface.

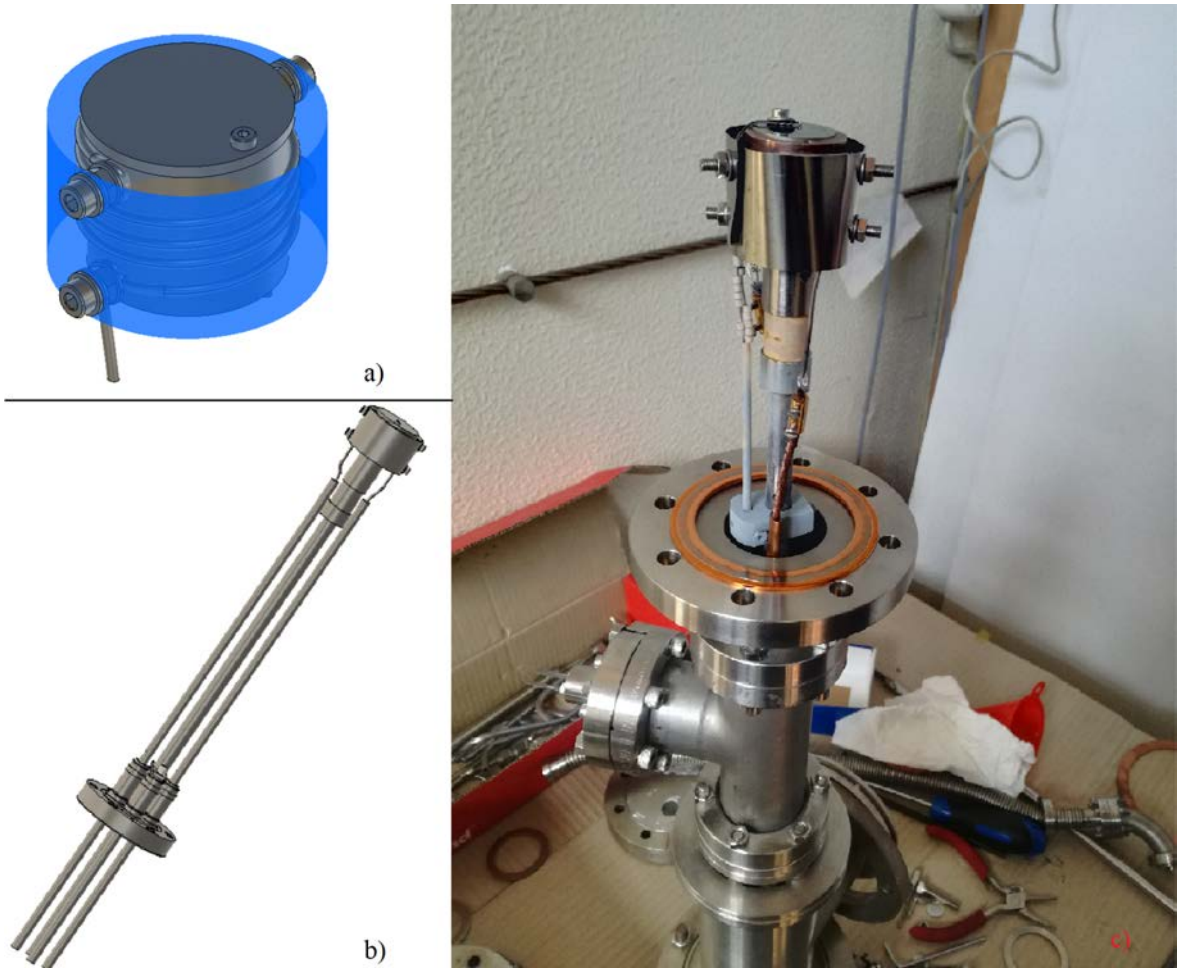

Figure 4.9: a) Heater drawing and SS shield (blu); b) Heater mounted on the power-feedthrough drawing; c) Picture of the heater mounted in the bottom part of the set-up

After a droplet is produced on top of the sample, each experiment is carried out increasing the temperature of the heater up to the desired value and recording the contact angle time evolution with a digital HD video camera recorder. The video is further analysed and the contact angles are studied by using the open source plugin *Contact Angle*, which estimates the contact angle of a drop on a surface using the sphere and ellipse approximation and calculating the tangent of a fitting curve for the drop profile near the triphase line. This plugin is written in Java programming language and it is loaded and run in ImageJ, a public domain Java-based image processing program.

Each sample is replaced with a new one isolating the top part of the experimental set-up from the bottom one thanks to two valves. During this step, Argon is injected from the opening located at the bottom left side of the machine. Argon is used to reduce the oxidation of the gallium still trapped in the pipe positioned after the

valve located at the end of the degassing tank and to hinder the entrance of the air inside the bottom chamber of the machine. The heater is removed and the sample is replaced and put back into place. The manipulator to which the two collectors are connected is also removed: gallium, previously collected, is discarded before doing a new experiment with a sample of different roughness in order to prevent its oxidation during the replacement procedure.

5

EXPERIMENTAL RESULTS

In this Chapter, the experimental results are presented and discussed. Two different set of experiments are carried out: the first one occurs at high temperatures (>500°C) in order to investigate the effect of roughness in the wetting process. The dependence on temperature of the contact angle is studied with the second type of experiments keeping constant the sample temperature at values lower than 500°C. The effect of time is also investigated here: the objective is to understand if wetting is achieved even at temperatures below than 400°C in a long experimental time scale (almost 12 hours).

5.1 GALLIUM INJECTION

After properly cleaning with alcohol in ultrasonic bath all the components, the experimental set-up is assembled and put under vacuum. In order to further decrease the pressure, the entire system is degassed for 24 hours at about 80°C by using the heating bands wrapped around. The final pressure reached is usually in the range of 10^{-8} - 10^{-7} mbar in cold state and just above 10^{-6} mbar with the heater on.

Gallium contained in the bottle showed in Chapter 4 is melted at 50°C in an oven and injected in the degassing tank by the procedure previously described. The total volume injected is approximately 194 cm^3. After that, gallium is degassed for 24 hours at 200°C and then the stainless steel membrane, located at the bottom of the degassing tank, is punctured.

In order to study how the contact angle is affected by temperature, roughness and time, two different kinds of experiments are carried out.

5.2 CONTACT ANGLE AS A FUNCTION OF ROUGHNESS

The first goal is to understand how roughness affects wetting when high temperatures are reached and kept constant on the sample surface. Therefore, three samples characterized by three different roughness values are prepared by using the techniques described in Chapter 4. The final roughness values, expressed in arithmetic mean value S_a, are: 3.3 nm, 63 nm and 750 nm. All the following experiments are recorded by a video camera and the video recording starts when the temperature on top of the specimen surface reaches 283°C. This value is chosen as a reference since before 300°C corrosion doesn't occur between gallium and stainless steel and no droplet changes are expected. Therefore at 283°C the evolution of the droplet can be studied just before this latter starts to evolve. As a consequence, the time reported in the images and in the graphs is referred to the time after 283°C is reached. Furthermore, considering the fact that temperature reaches the maximum value in about one hour from the start of the video and remains constant until the end, all the following experiments are considered to occur in an isothermal way.

3.3 nm rough sample

At first, the sample surface is treated with the grinding technique. Three different silicon carbide papers are subsequentially used, starting with the one with the highest roughness until the finest one: P1000, P2400, P4000. After the grinding step, the polishing is carried out and a cloth of 1 μm is used to get a mirror like surface. In the end, the final roughness is studied with the 3D profilometer. The final roughness

Figure 5.1: Image taken with the profilometer. S_a=3.3 nm

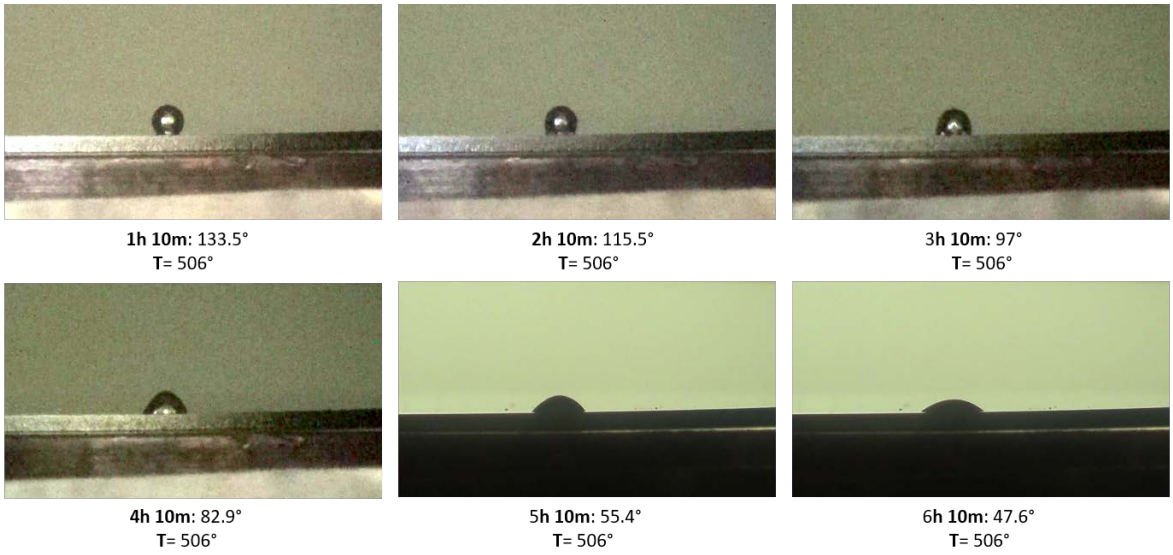

Figure 5.2: First droplet evolution on 3.3 nm rough sample

value, expressed in arithmetic mean value S_a, is 3.3 nm. The image of the surface taken with the profilometer is reported in Figure 5.1.

After having installed the sample on top of the heater, closed the machine and started the vacuum, two experiments are carried out depositing two droplets .

The first droplet is heated up to 506°C increasing the voltage of the power supply. The video is started when temperature reaches 283°C. After one hour of video recording, the temperature reaches the maximum value of 516°C and remains constant. The droplet evolution is recorded for 6 hours. The time evolution of the droplet is reported in Figure 5.2: 6 images taken every one hour are shown. The respective time, temperature and contact angle are reported in the caption.

On the same sample, a second droplet is deposited and heated up. This time, the maximum temperature reached by the heater, using the same voltage, is 509°C. The droplet evolution as a function of time is shown in Figure 5.3. Since a third droplet was involuntarily created, the one considered for the experiment is the nearest one to the camera, which is the one placed in the centre of every image of Figure 5.3 and marked by a red circle.

From the videos of the two experiments, images at different time are extracted and the apparent contact angle θ is studied by using the *Contact angle* plugin of ImageJ software, as it was already described in the previous chapter. In Figure 5.4 the contact angle evolution of the two droplets is reported. Considering that the difference in

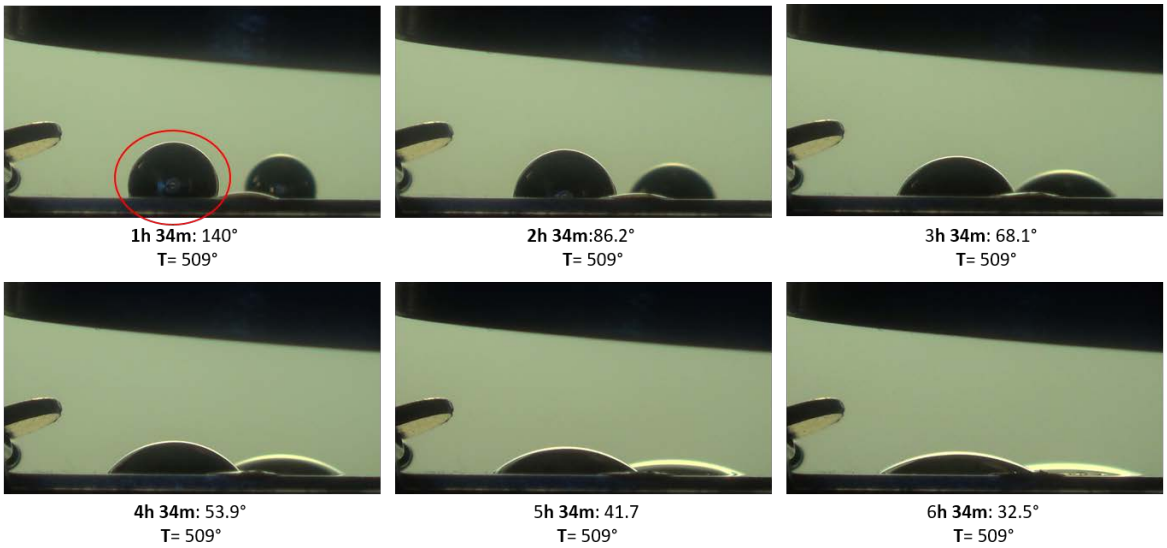

Figure 5.3: Second droplet evolution on 3.3 nm rough sample

the maximum temperature reached in the two experiments is negligible, Figure 5.4 reports two plots where the temperature is considered constant and equal for both the cases. From the graph, it's clear that the contact angle θ decreases with time to values below 90° and therefore, wetting is achieved. Moreover, the contact angle continues to decrease during the full video duration: in this case, the wetting process

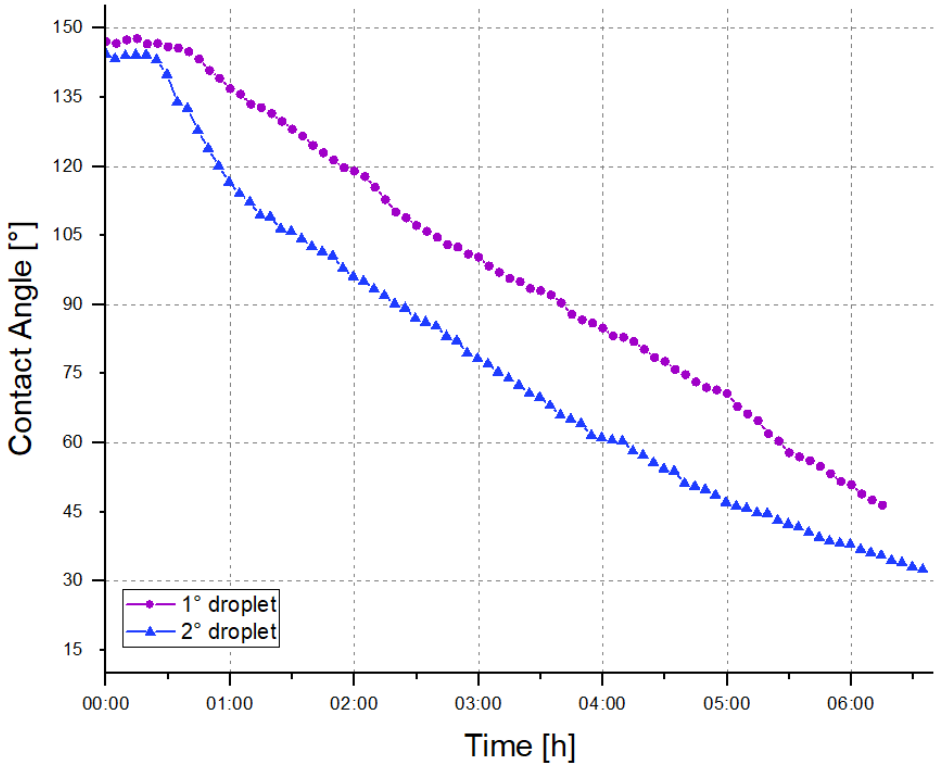

Figure 5.4: Contact angle plot, sample of 3.3 nm rough

occurs with the spreading of the droplet. The two contact angle θ values reached at the end of the recordings are quite different from each other: the second droplet spreads on top of the sample faster than the first one deposited. On the other hand, the time recording video was not enough to let the contact angle reach an equilibrium value. Lastly, for both the experiments, the droplets don't change for the first 30 minutes and the contact angles oscillate around a constant value. After that, the contact angles start to decrease.

63 nm rough sample

This second sample is treated by the grinding techniques in order to get a higher value of roughness. Only one silicon carbide paper is used and the chosen one is the P320. In Figure 5.5 the image of the treated surface taken with the 3D profilometer is reported. The measured roughness, expressed in arithmetic mean value S_a, is 63 nm.

Two droplets are deposited on top of the sample surface, after having installed it on the heater. The temperature is faster increased and the camera is turned on when the temperature reaches 283°C. After this point, the experiment is recorded for about 6 hours. Temperature reaches the maximum value of 507°C in the first experiment and of 504°C in the second one. A fast evolution of the droplets is showed in Figure 5.6 and Figure 5.7: 6 images extracted every one hour are reported with the respective contact angle values.

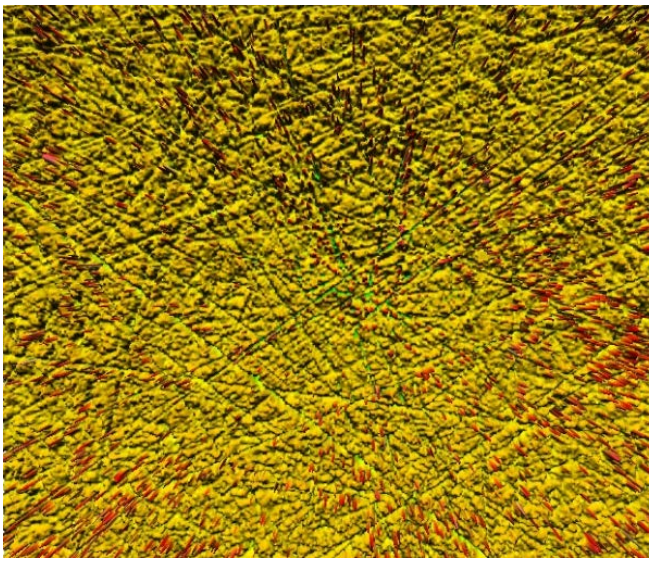

Figure 5.5: Image taken with the profilometer. S_a=63 nm

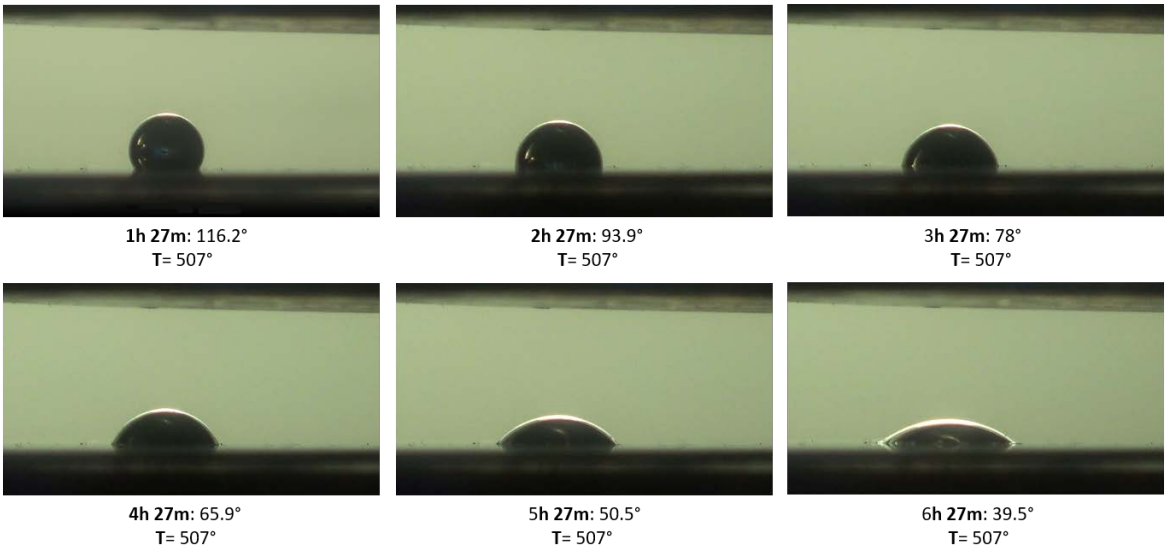

Figure 5.6: First droplet evolution on 63 nm rough sample

The contact angle behaviour with respect time for both the droplets is reported in Figure 5.8. Since the difference in temperature between the two experiments is negligible, Figure 5.8 is an isothermal graph. The same observations made for the previous plot 5.4 can be done for this last graph: wetting is achieved and the contact angle continues to decrease with time without reaching an equilibrium value in the video recording time. Moreover, the second droplet spreads faster with respect to the first one.

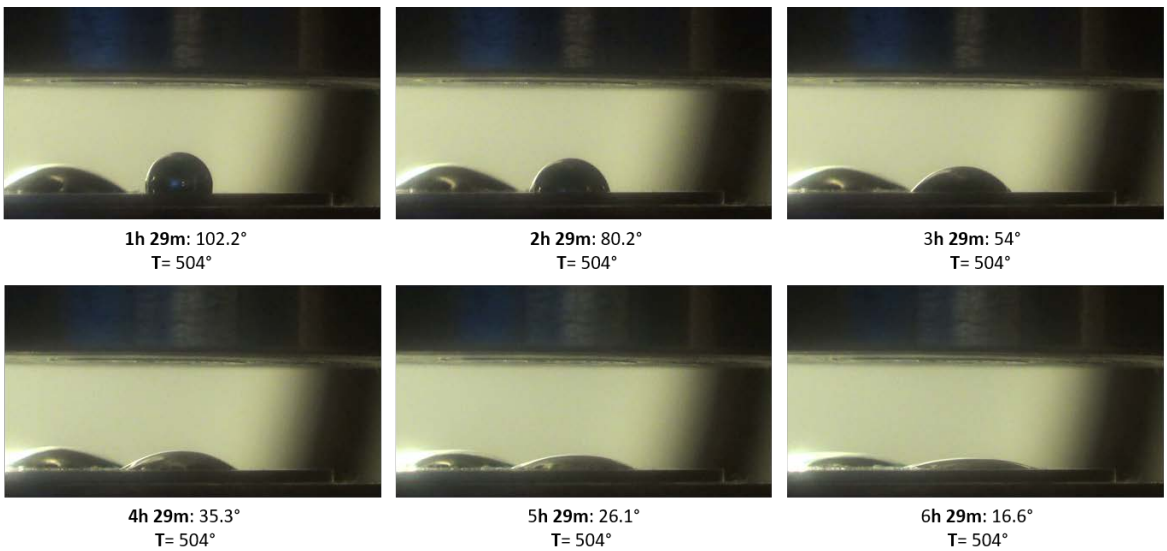

Figure 5.7: Second droplet evolution on 63 nm rough sample

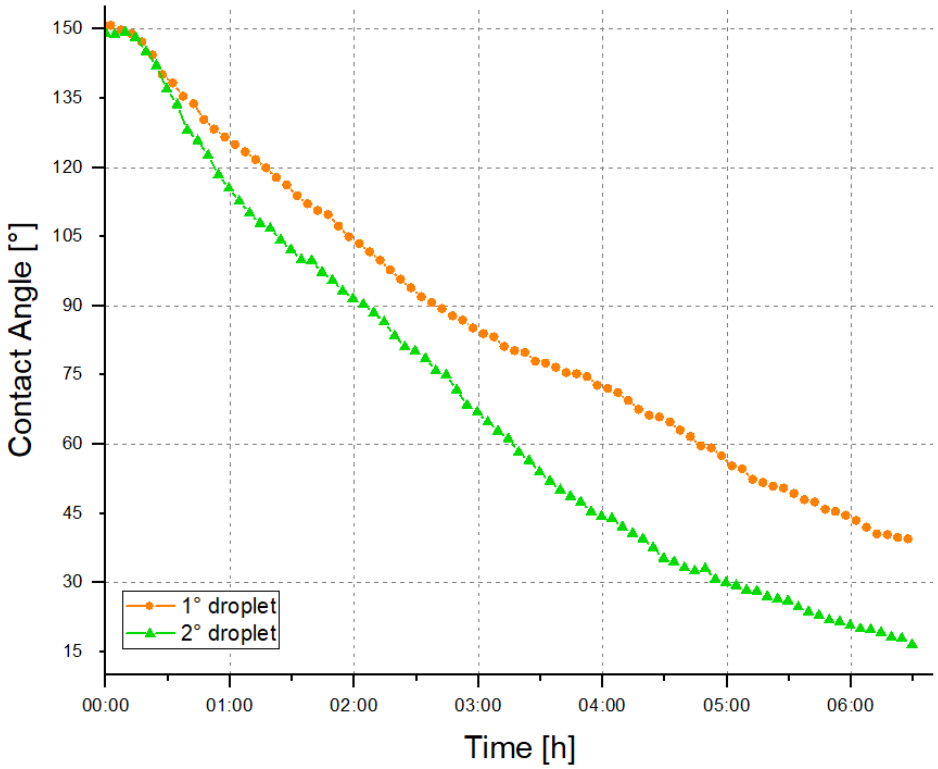

Figure 5.8: Contact angle plot, sample of 63 nm rough

750 nm rough sample

This third sample is treated only with the grinding technique and the silicon carbide paper chosen is P80. In Figure 5.9 the image of the treated surface taken with the 3D profilometer is reported. The roughness measured, expressed in arithmetic

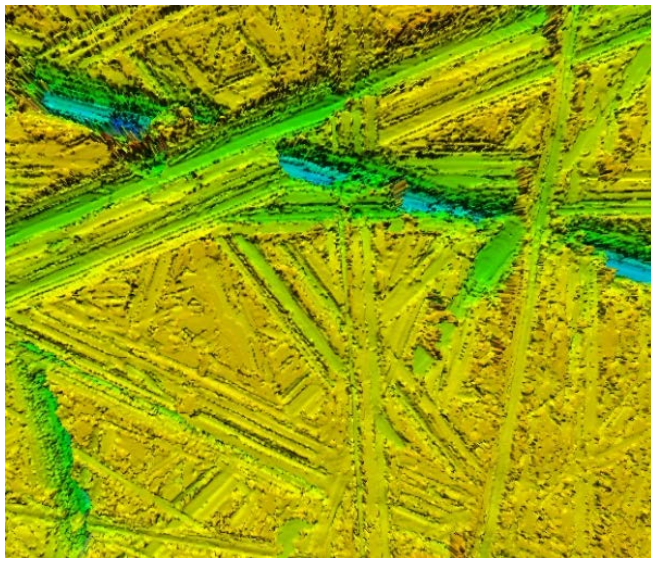

Figure 5.9: Image taken with the profilometer. S_a=750 nm

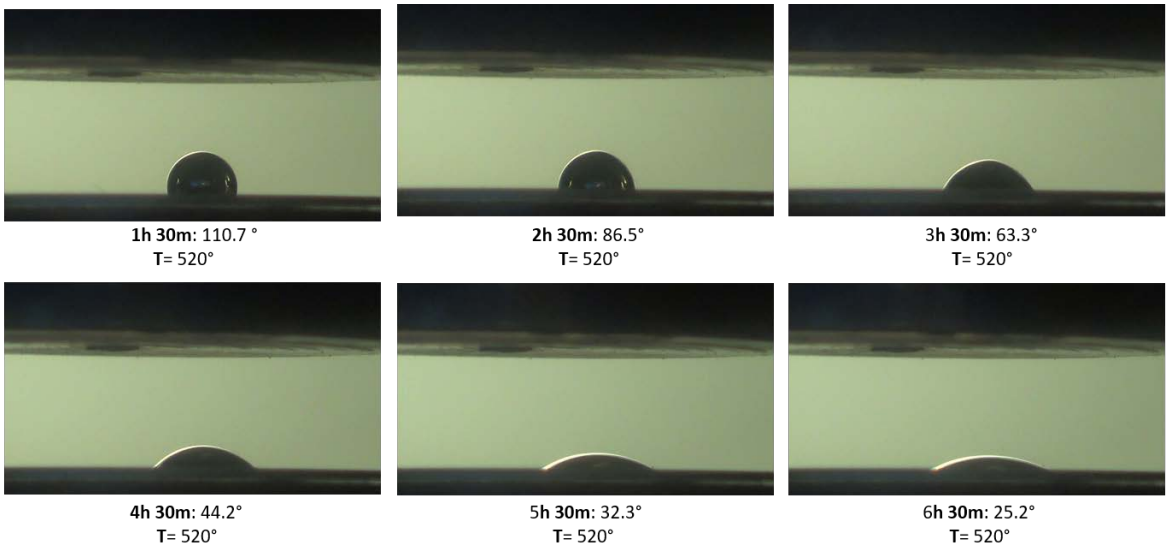

Figure 5.10: First droplet evolution on 750 nm rough sample

mean value S_a, is 750 nm.

Also for this sample, the experiment is repeated two times. In the first time, the deposited droplet is heated up to 520°C. After that, a second droplet is produced and the maximum temperature reached by the heater is 518°C. The contact angle evolution is recorded with the camera starting from when temperature reaches 283°C. Figure 5.10 and Figure 5.11 show how the droplets shape θ changes as a function of time. From Figure 5.11, that reports the fast evolution of the second droplet, it's clear that it reaches completely spreading at the end of the video recording. Moreover, in the last image is observable a new compound layer originated during the wetting

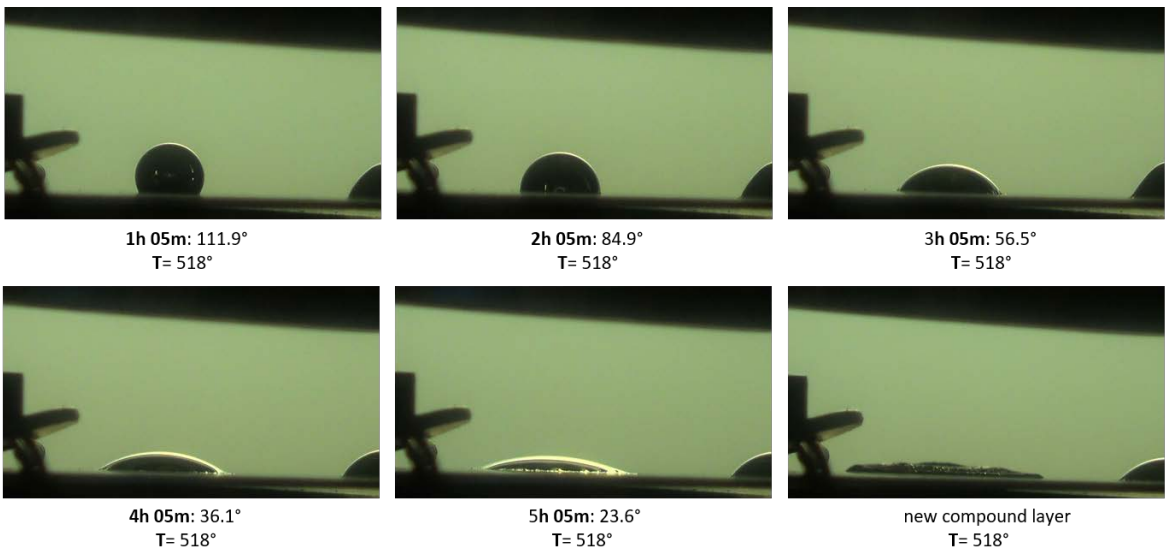

Figure 5.11: Second droplet evolution on 750 nm rough sample

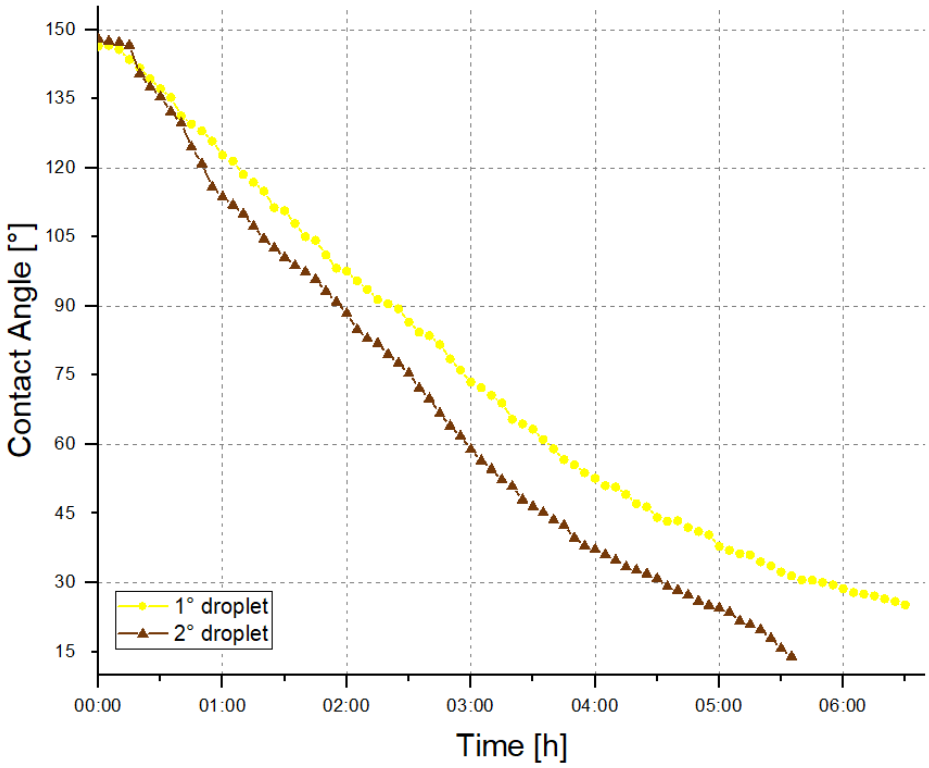

Figure 5.12: Contact angle plot, sample of 750 nm rough

process.

In Figure 5.12 the contact angle evolution of the two droplets is reported. Also for this graph, the difference in temperature between the two experiments is neglected. Furthermore, the behaviours of the droplets observed for the previous two samples are confirmed also for this latter. The curve related to the second droplet stops before the other one since after a certain time it was impossible to measure the contact angle: the droplet spreads completely and the new compound layer is observable.

Figure 5.4, Figure 5.8 and Figure 5.12 make evidence that the second droplet is always spreading faster than the first one. This phenomenon can be explained considering that there is always a small amount of oxygen retained in the stainless steel samples that might have produced a thin layer of gallium oxide. This oxygen completely degassed during the heating of the first droplet: there was no longer any oxide layer when the second droplets were deposited. Therefore, the data related to the second droplets are considered more reliable. This hypothesis could have been demonstrated by degassing at high temperature the SS sample before producing the first droplet.

Comparison between samples

In order to better understand how roughness affects the contact angle, a comparison between all the previous experiments has to been done. Figure 5.13 and Figure 5.14 summarize the behaviours of the first and the second droplets respectively as a function of time and roughness. Considering the fact that the maximum temperatures reached in all the experiments are relatively close, temperature is assumed as constant. As it is evident from both the graphs, wetting, defined as contact angle $\theta < 90°$, was achieved in all the experiments. Unfortunately, the video recording time was not long enough to let the contact angles reach an equilibrium value. Looking at the previous figures that show the fast evolution of the droplets, the formation of an intermetallic compound layer can be observed at the triple line contact. This latter it's easier to notice in the last image of Figure 5.11, where the gallium droplet completely reacted with the stainless steel surface, corroding it. Therefore, the type of wetting process that occurs between gallium and stainless steel is reactive: an intermetallic layer is formed and it grows radially as the wetting process proceeds with time. Furthermore, Figures 5.13 and 5.14 provide evidence that the increase in roughness speeds up the wetting process: the second droplet deposited on top of the sample with the highest roughness spreads completely up to a point it was no longer possible to measure and study the contact angle. This fact can be explained by considering that the high temperatures reached in all the experiments have increased the diffusion rate in such a way that the reactant gallium is fast replenished at the un-reacted substrate: the rough surface provides an additional interfacial area for the reaction which is easily reached by new reactant thanks to the high diffusion rate. The plotted curves seem similar to the one reported in Figure 3.7: after an exponential decay, the curves change abruptly at the end of the graph. Unfortunately, the 6 hours of video were not enough to better observe the linear behaviour that should follow the first exponential stage, as it is shown if Figure 3.7. On the other hand, Figures 5.13 and 5.14 don't clearly show how time affects the wetting angle: the previous experiment demonstrated that keeping the temperature at a value higher than 500°C, wetting is achieved in a couple of hours and that the contact angle continues to change in time but it's not clear if wetting can be achieved at low temperatures just keeping the experiment going on for a long time.

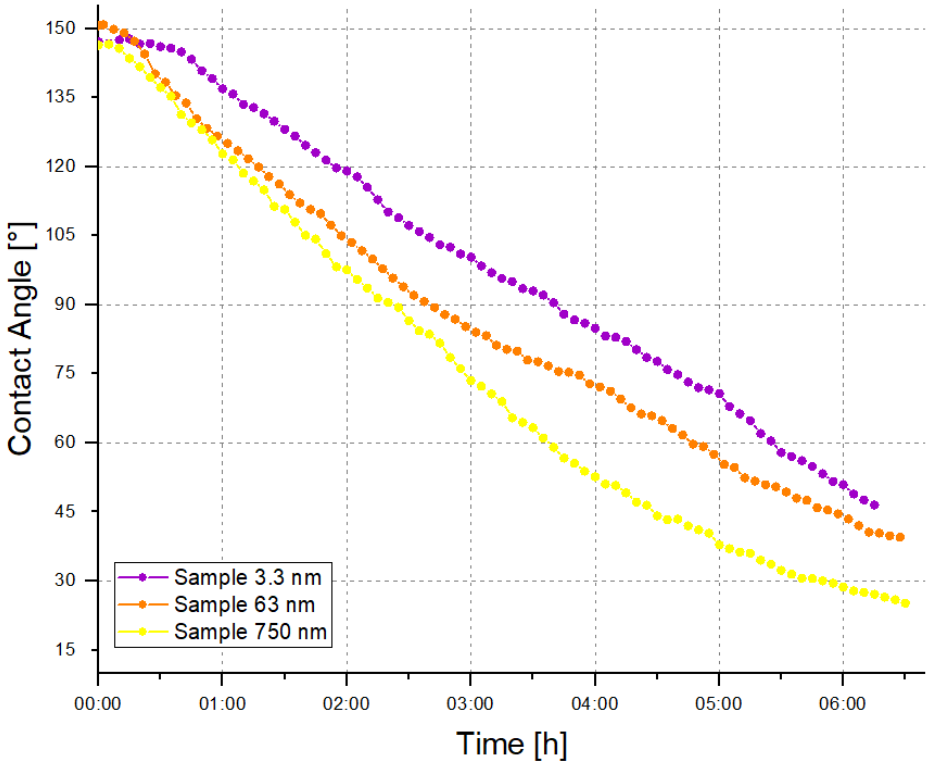

Figure 5.13: Contact angles behaviour of the first droplets at high T

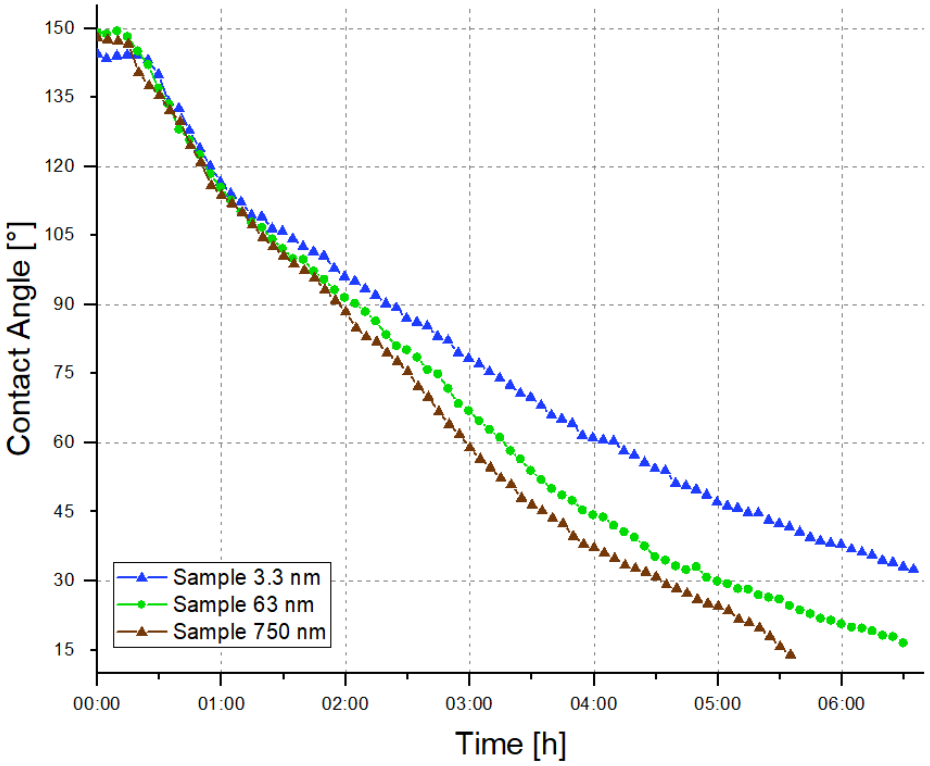

Figure 5.14: Contact angles behaviour of the second droplets at high T

5.3 CONTACT ANGLE AS A FUNCTION OF TEMPERATURE AND TIME

The main objective of this section is to understand how temperature and time affect the contact angle. In order to do that, three experiments are carried out and repeated on two samples with different roughness at temperatures lower than 500°C. The roughness values, expressed in arithmetic mean value S_a, are 22.6 nm and 792 nm whereas, the temperatures at which the experiments are carried out are 309°C, 352°C and 432°C. All the experiments described hereafter are recorded by a video camera and the video recording starts after the temperature on top of the specimen surface reaches 283°C. Therefore, time is counted from the moment temperature has reached this reference value. The video recording lasts about 12 hours since a slower wetting process is expected. Furthermore, temperature is always considered constant for every experiment: the maximum value is reached in less than one hour from the start of the video and remains constant until the end. For the first sample, the experiments were carried out starting from the one at the highest temperature (T=432°C) and finishing with the one at the lowest temperature (T=309°C). Whereas for the second sample, the experiments were carried out increasing temperature. All the experiments are following described starting from the one at the lowest temperature for both the samples.

22.6 nm rough sample

The sample surface is treated with the grinding technique. The desired final roughness value is intermediate between the roughness of the first two samples previously

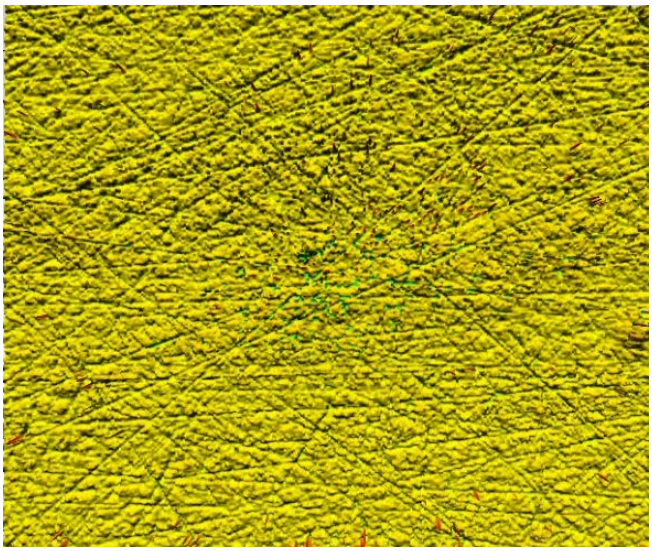

Figure 5.15: Image taken with the profilometer. S_a=22.6 nm

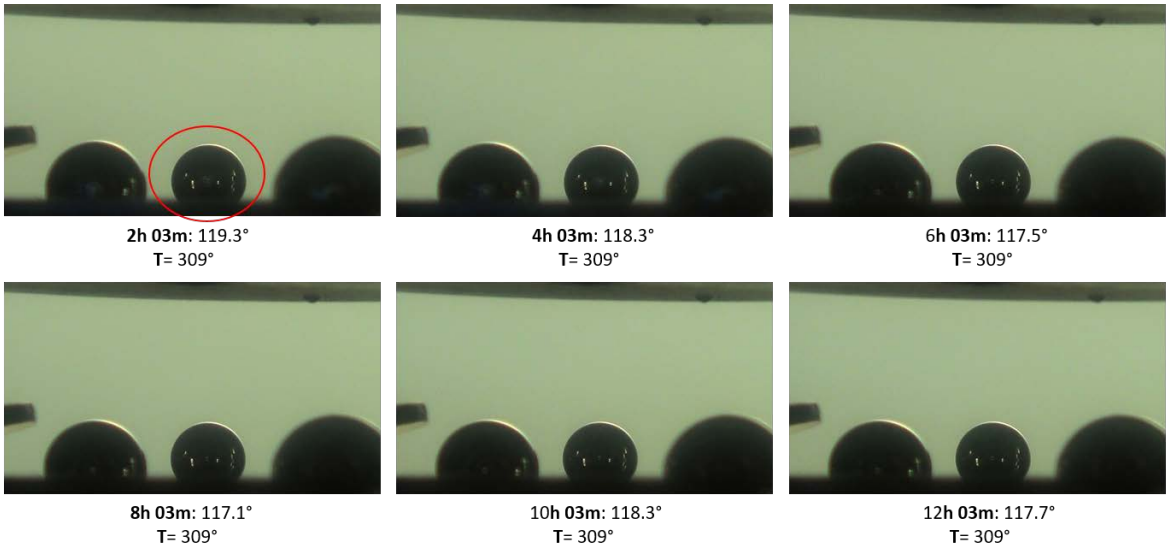

Figure 5.16: First droplet evolution on 22.6 nm rough sample, T=309°C

studied in order to have a middle-way behaviour. The silicon carbide paper used to treat this first sample is P800. It is recalled that higher is the number of the paper, smoother will be the surface treated. The final roughness is studied with the profilometer 3D (Figure 5.15) and the roughness value, expressed in arithmetic mean value S_a, is 22.6 nm.

After mounting the sample on top of the heater and have closed the machine, three experiments are carried out at different temperatures.

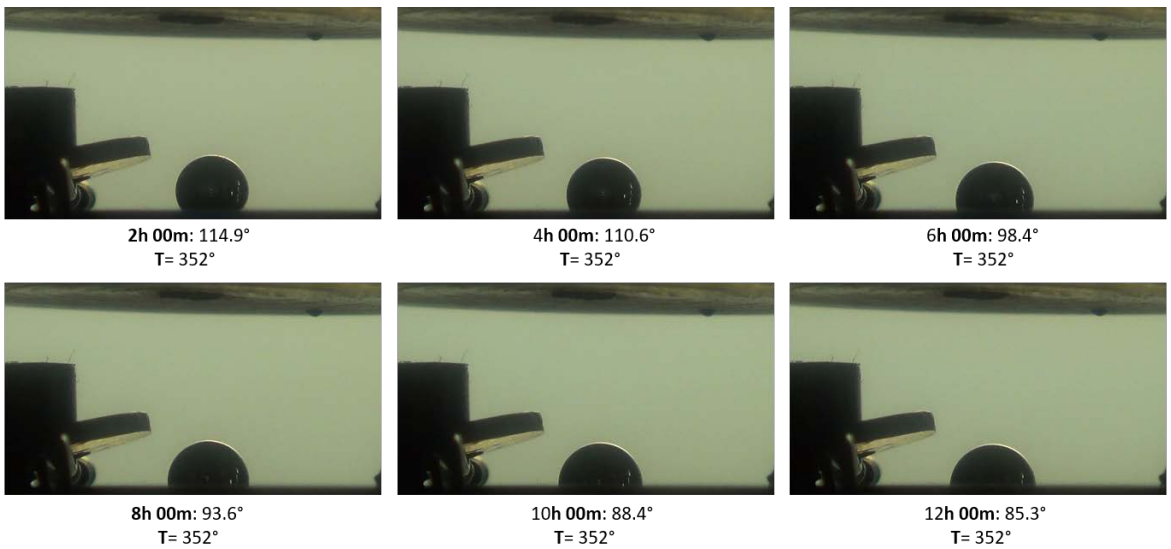

Figure 5.17: Second droplet evolution on 22.6 nm rough sample, T=352°C

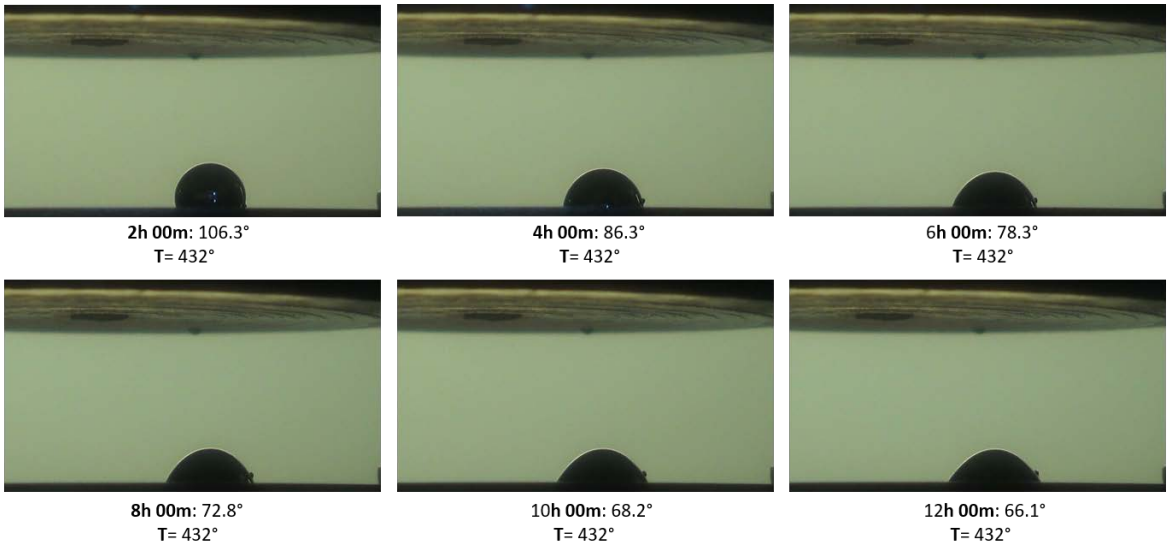

Figure 5.18: Third droplet evolution on 22.6 nm rough sample, T=432°C

In the first one, a droplet (Figure 5.16, marked by a red circle) is deposited and heated up to 307°C. The second and third experiments are carried out at higher temperatures: 352°C and 432°C respectively. Figure 5.16, Figure 5.17 and Figure 5.18 illustrate how the droplets evolve with respect time at the three different temperatures: wetting is achieved only in the last two experiments. At the end of the video recording, the contact angle θ of the second droplet reaches a value just below 90°.

The contact angle behaviours of the three experiments are summarized and plotted in Figure 5.19. From the graph, it can be concluded that wetting improves with increasing in temperature. For the experiment carried out at T=309°C, the contact angle slightly decreases at the beginning before reaching an equilibrium value around 120°. All the curves have a general trend: after a small exponential decay at the very beginning of the graph, there is a linear behaviour during while the contact angle changes slowly. After that, θ reaches an equilibrium value. Wetting, reached when contact angle $\theta < 90°$, was achieved at T=432°C and T=352°C. It has to be underlined that, in the last case, the equilibrium value was around 87°.

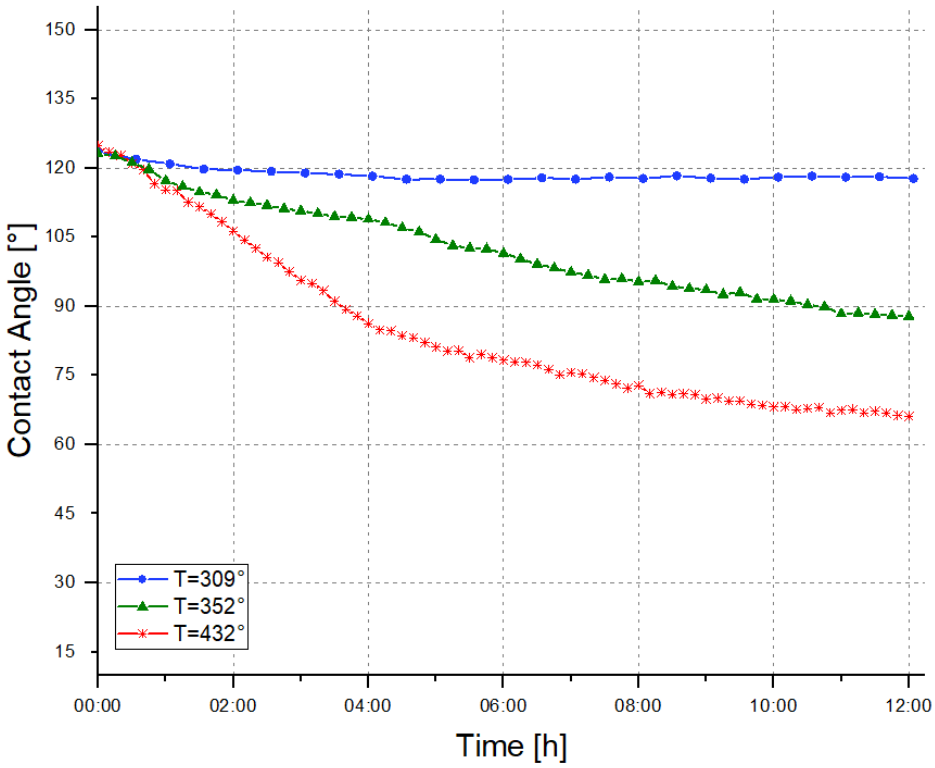

Figure 5.19: Contact angles plot at different T, sample of 22.6 nm rough

792 nm rough sample

This second sample is only treated with the silicon carbide paper chosen P80 in the grinding machine. The final value of surface roughness S_a is 792 nm (Figure 5.20).

Figure 5.20: Image taken with the profilometer. S_a=792 nm

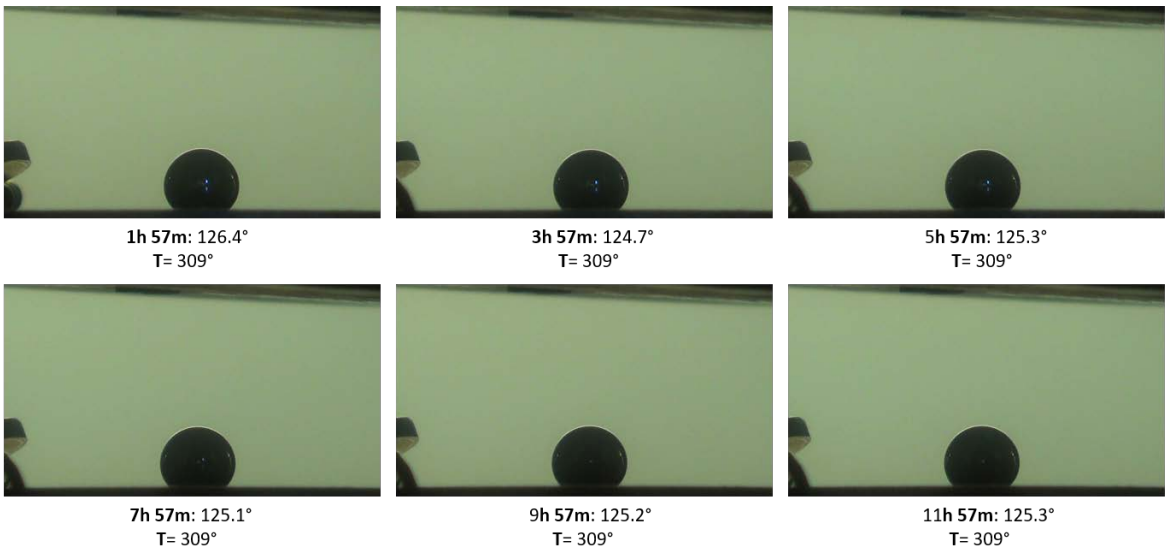

Figure 5.21: First droplet evolution on 792 nm rough sample, T=309°C

Also for this sample, three experiments are carried out at different temperatures, like previously: 309°C, 352°C and 432°C. Figure 5.21, Figure 5.22 and Figure 5.23 show the fast evolution of the droplets deposited in ever experiment. Six images extracted every 2 hours are reported. Wetting is achieved only in the last experiment carried out at 432°C.

Figure 5.19 summarize the trend of the contact angles of the three droplets as a function of temperature and time. As it was observed for Figure 5.19, higher temperatures improve the wetting process: it's evident that wetting is achieved only for T=432°C. Moreover, the video recording time was long enough to appreciate

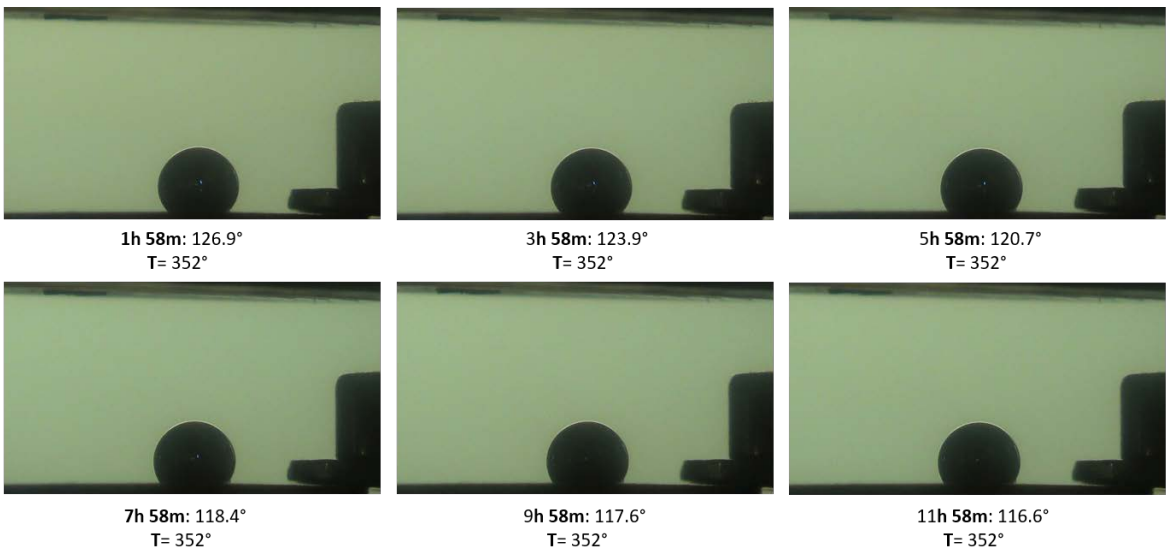

Figure 5.22: Second droplet evolution on 792 nm rough sample, T=352°C

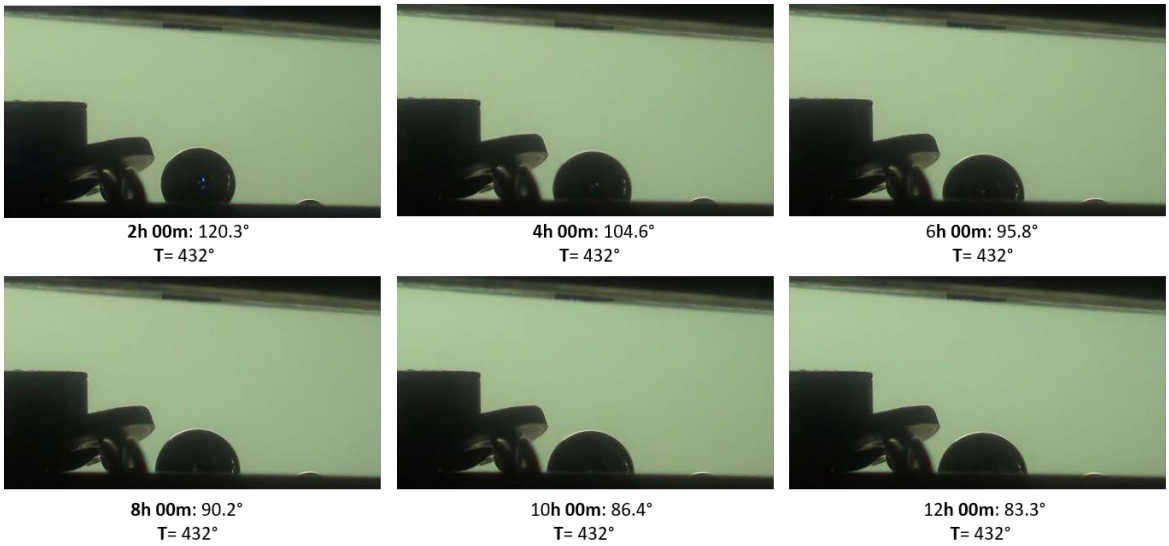

Figure 5.23: Third droplet evolution on 792 nm rough sample, T=432°C

the different trends of the curves, which are the same observed for Figure 5.19. Furthermore, the curves evidence that at higher temperature wetting is improved and a longer time is required for the droplet to reach a steady state value.

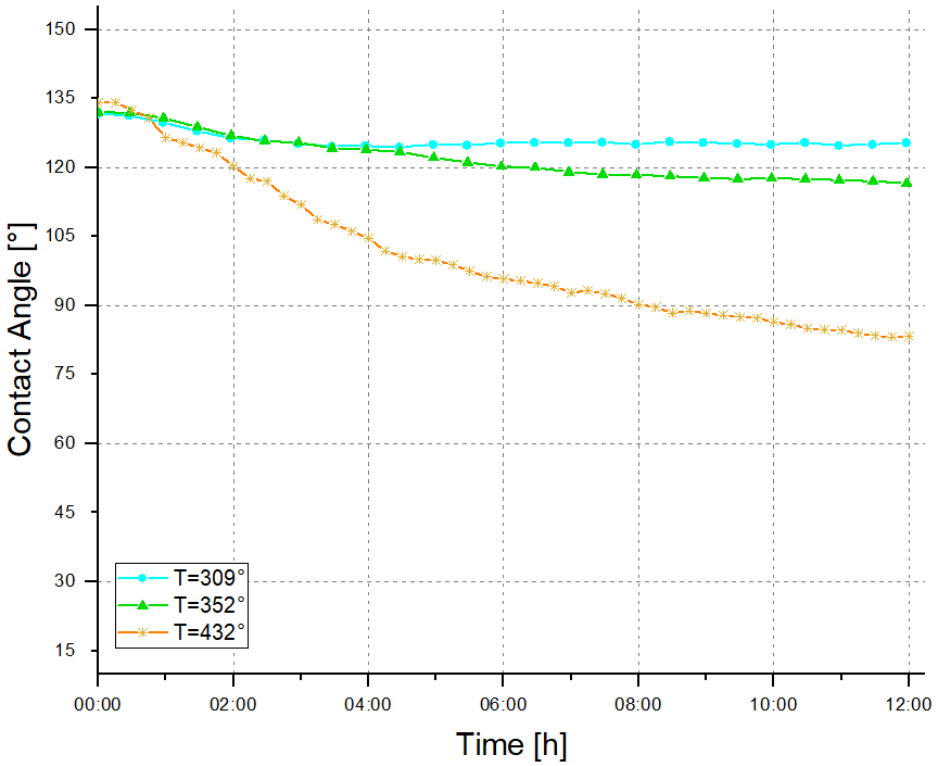

Figure 5.24: Contact angles plot at different T, sample of 792 nm rough

Comparison at different temperatures

In order to have a general view of the previous results, Figure 5.25, Figure 5.26 and Figure 5.27 illustrate the behaviour of the droplets deposited on the two samples of 22.6 nm and 792 nm roughness and heated up to 309°C, 352°C and 432°C respectively.

These graphs provide evidence that temperature improves the wetting process but, simultaneously, the droplet requires more time to reach a steady state point. Moreover, it was demonstrated that temperature is the most fundamental parameter to achieve wetting: gallium doesn't wet the stainless steel samples below 350-400°C even after 12 hours of experiment.

Regarding roughness, the wetting process is favoured by low values of roughness at temperatures below 500°C : as an example, at T=352°C, wetting was achieved only for the sample of 22.6 nm roughness. This result seems to be in contrast with the one observed and obtained from the previous type of experiments carried out at high temperature. Making a comparison between the curves obtained at high temperature and a lower temperature (Figure 5.13, Figure 5.14, Figure 5.25, Figure 5.26 and Figure 5.27), it's evident that the all the graphs can be approximated with the one reported in Figure 3.7, since it a reactive wetting process occurs between gallium and stainless steel. The curves relating to the experiments carried out at high temperature (>500°C) are characterized by a longer first stage, during which the contact angle changes with an exponential decay until value even below 20°. During this stage, the wetting process is controlled by the reaction at the triple line: the second stage is observable just at the end of the 6 hours of the video recording after an abrupt change in the curve slope. On the other hand, the graphs that report the contact angles behaviour at lower temperatures (309°C, 352°C, 432°C) are characterized by a shorter first stage: after a fast exponential change, the contact angle continues changing in a linear way for a long time before reaching the final equilibrium value. Moreover, Figure 5.19 and Figure 5.12 illustrates that as the temperature increase, the second stage decrease in time and the first one takes longer to occur. This means that high temperatures favour the diffusion of reactant to the un-reacted substrate and the overall wetting process is controlled by the reaction at the triple line. This fact takes more evidence considering that roughness enhances the wetting process only at temperatures greater than 500°C: a higher diffusion coefficient leads to an easier overcome of the grooves and a faster replenishment of reactant to the new un-reacted surface. The grooves provide a larger substrate to the reaction to occur: the combination of fast diffusion rate and the addition of interfacial area has results in an improvement of the wetting process. On

the other side, at temperatures lower than 500°C, an increase in roughness hinders the spreading of the droplet due to the pinning effect [1] on the rough surface. The wetting kinetics and final contact angle are controlled by the diffusion of the reactant at the triple line.

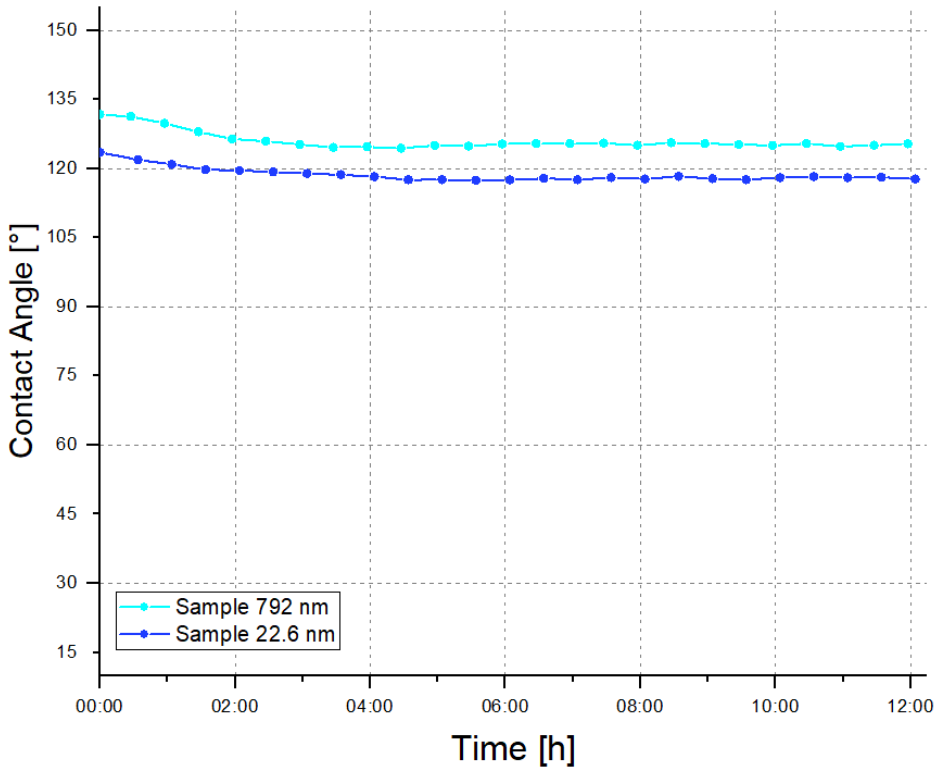

Figure 5.25: Contact angles evolution on samples with S_a= 22.6 nm and S_a=792 nm, T=309°C

[1] Point defects present in a material act as a barrier that requires a greater amount of force in order to be overcome.

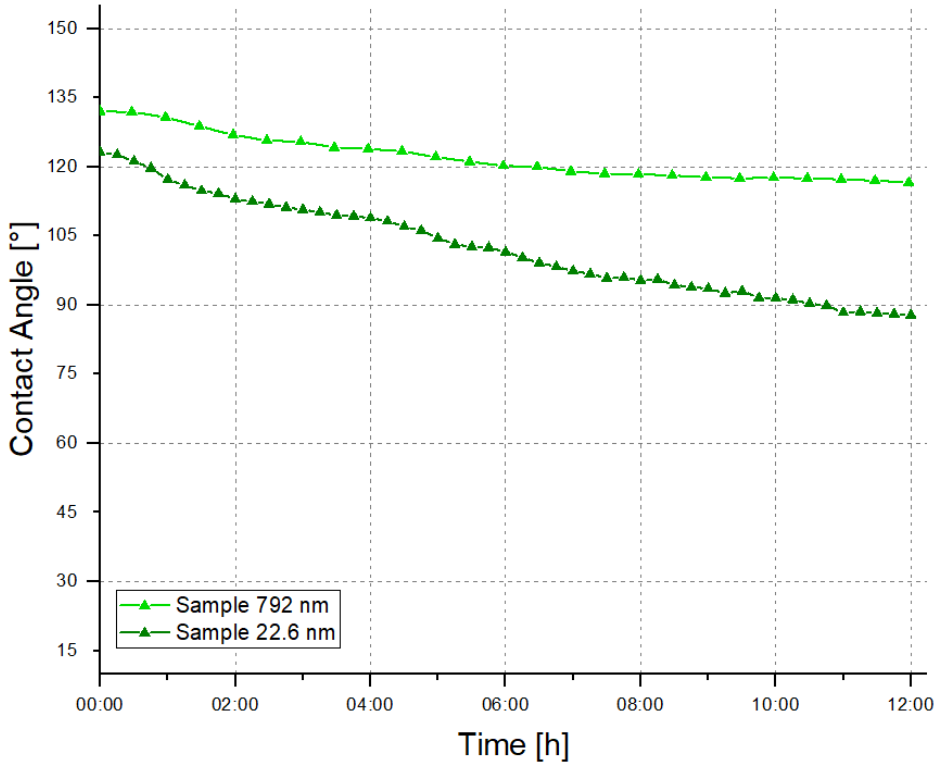

Figure 5.26: Contact angles evolution on samples with S_a= 22.6 nm and S_a=792 nm, T=352°C

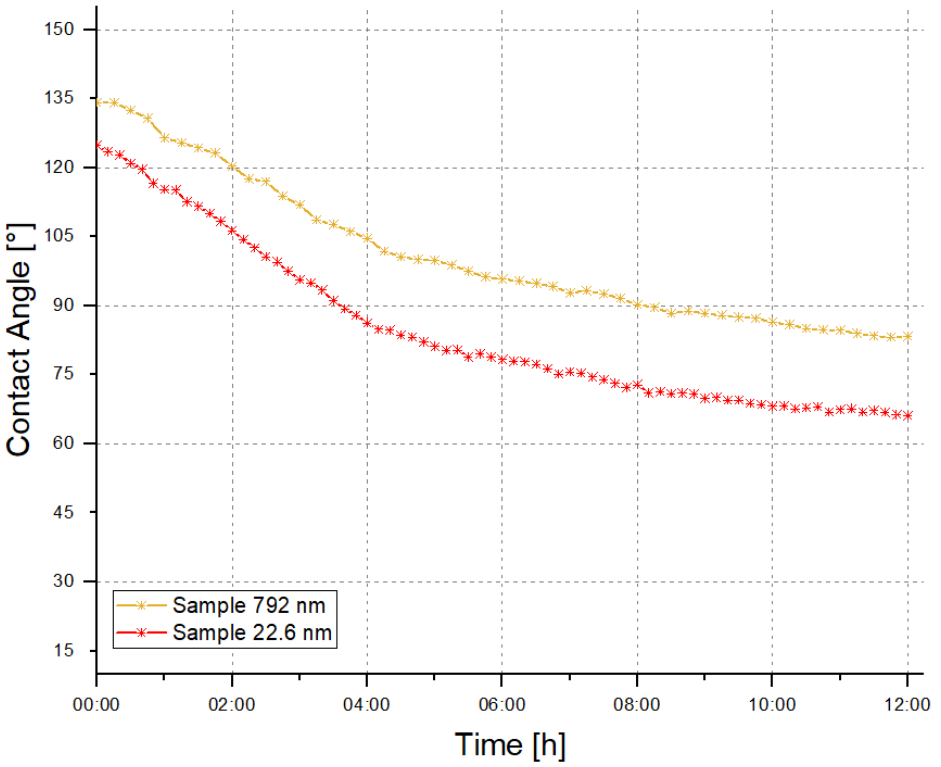

Figure 5.27: Contact angles evolution on samples with S_a= 22.6 nm and S_a=792 nm, T=432°C

CONCLUSIONS AND FUTURE WORK

The main objective of this thesis project was to study and investigate the wettability of stainless steel by liquid gallium. Gallium is a liquid metal that could be employed as a plasma facing component (PFC) in a fusion reactor to replace the most commonly used solid material. Liquid Metals can provide a reliable and feasible solution to the main drawbacks that arise from the impinging of high energy particles on the surface of the solid PFC, like tungsten and beryllium. This work fits into the context of the research to assess the wetting properties of gallium on material that might be used as capillary porous system (CPS), like stainless steel.

The first part of the project was focused on the design and construction of a specific experimental device to test the wettability of stainless steel by pure and oxide-free gallium. The final set-up is an ultra-high vacuum (UHV) equipment that works in a range of $10^{-8} - 10^{-7}$ mbar. Gallium was kept in liquid state by using heating bands wrapped around the gallium tank. In order to determine the effect of temperature on the wetting process, the stainless steel samples have been mounted on top of a heater specifically designed for this work. The maximum temperature that the heater was able to handle due to materials constraints is 540°C.

The second part of the project was centralized on the exploitation of the experimental set-up. Two different set of experiments of experiments have been carried out in order to understand how the wetting phenomena are affected by the following three variables: roughness, temperature and time. The first set was carried out at temperatures above 500°C and three samples with different roughness values (3.3 nm, 63 nm and 750 nm) have been tested. The effect of time and temperature was more deeply investigated with the second type of experiments: two samples of 22.6 nm and 762 nm roughness have been exposed at three different temperature values (309°C, 352°C and 432°C) in order to investigate if wetting is achieved at these physical conditions. Furthermore, it was tried to figure out if, despite the lower temperatures, the contact angle θ decreases below 90° in a longer experimental time scale.

The extracted images of the droplets provide evidence that an intermetallic compound layer is formed during the wetting process: this layer grows radially with

time as the droplet continues spreading. Therefore, a *reactive wetting* occurs between gallium and stainless steel.

The graphs that show the contact angles behaviour as a function of temperature and time clearly indicate that the wetting process is favoured by high temperatures: the time to achieve wetting decreases as the temperature is raised. Furthermore, the second type of experiments have underlined that wetting can be achieved in a longer time scale even at lower temperatures than 500°C but not when temperature is below 350-400°C.

Furthermore, the first set of experiments made evidence that the second droplet, deposited at the same conditions of the first one, spreads faster. The degassing of the oxygen retained in the stainless steel sample during the heating of the first droplet can be a reliable explanation to this phenomenon. In order to prove this hypothesis, the stainless steel samples could be degassed at high temperature before producing the first droplet in the future experiments.

Turning to the effect of roughness, at a first sight the results obtained at T>500°C seem to be in contrast with the ones obtained at lower temperatures: in the first case, the wetting process was enhanced by higher roughness values, whereas in the second case it was hindered. This can be explained observing in details the overall plots. All the curves of the contact angles can be divided into two main stages: a first one characterized by a direct contact between gallium and the initial stainless steel substrate and controlled by the local reaction process at the triple line, and a second stage controlled by the diffusion of gallium to the un-reacted substrate during which the liquid metal has no longer direct access to the initial substrate surface.
The curves related to the first types of experiments show a longer first stage: the contact angle changes in an exponential way until low values are reached. The second stage is only observable at the end of the six hours of experiment. On the other hand, the graphs of the second type evidence a shorter first stage: the contact angle have a fast change at the beginning of the experiment and after that an almost linear trend is observable. This phenomena underlines that high temperatures favour the diffusion of gallium to the un-reacted substrate so that the overall process is controlled by the reaction at the triple line: at temperatures greater than 500°C, roughness enhances wetting since the diffusion coefficient is high enough to overcome the grooves and the surface asperities and to replenish gallium to the un-reacted surface. By contrast, at temperatures lower than 500°C, an increase in roughness hinders the spreading of the droplet due to the pinning effect on the rough surface: the diffusion rate is not

enough to overcome the surface grooves.

Future development of this work will be the analysis of the intermetallic compound layer to better understand the reaction involved in the wetting process. Moreover, it might be interesting to record the experiments carried out at high temperature for a longer time to have a more general view of the second stage of the contact angle curve. The choice of stainless steel as a material to study gallium wetting properties was only a starting point: in future, a mesh of stainless steel, that might be used as a CPS, will be tested. Furthermore, a new and more efficient heater able to reach up to 800°C is in construction in order to test tungsten samples.

ACKNOWLEDGEMENTS

Quando iniziai l'università a Padova non avevo alba dei fantastici ed indescrivibili anni che mi attendevano. Un lungo percorso di studi può essere completato se solo si è circondati dalle persone giuste...

Vorrei cominciare a ringraziare tutti gli amici di Padova con cui ho condiviso quattro intensi anni. Ognuno di voi ha reso questa magnifica città una seconda casa. Anno dopo anno, in sella alle nostre inseparabili bici, mi avete aiutato ad apprazzarne e scoprirne sempre di più i segreti e adesso, ogni singola piazza, strada e angolo sono indissolubilmente legati ad un momento che ho condiviso con voi. Anche se forse non ve ne stavate rendendo conto, avete lasciato dei ricordi indelebili non solo a me, ma a Padova stessa che si nutre, vive e si impreziosisce grazie a noi studenti che la popoliamo e la rendiamo scrigno vivente dei nostri ricordi più intensi. Tornare in questa città senza di voi susciterà sempre in me un misto di emozioni, un antitetico connubio fra tristezza e felicità che sfocia in una semplice e pura nostalgia. Avere voi al mio fianco ha ridimensionato se non annichilito ogni difficoltà incontrata nel lungo percorso di studi. Non potrò mai dimenticare gli spritz del mercoledì universitario, le ansie condivise prima di un esame, le serate ai navigli, i teini serali, le cene in compagnia, il bar in cui ci trovavamo per iniziare la serata ma, soprattutto, la felicità, le risate e la gioia che accompagnavamo ogni istante condiviso .

When I started my Erasmus in Lisbon, I didn't know that, for a second time, I was going to be so lucky to find such amazing and unique people. In Portugal, I finished my exams and did my thesis and you managed to write the perfect end for my wonderful university days. All of you gave me the possibility to have amazing experiences that not all the Erasmus students have the possibility to live. Since the beginning, the closest brewery to the university became a fixed appointment on Friday after a week of work and a place where to organize pizza-parties or share some nice food with the perfect "cerveja". The card games during the lunch break, the barbeques and the nights out in Bairro Alto will be always in my heart and you are the main characters of all these unforgettable memories. We shared amazing trips and the Sunday drives to climb made me appreciate the beauty of Portugal not only from the "ground level" but also from the "top of a rock" level! Particularly, I will

always be grateful to my colleagues in IPFN that helped me with the thesis, shared with me their deep knowledge in topics I never dealt with, cheered me up when I was struggling with the experimental device and celebrated with me an experimental success!

There are no other words to say thank you! Thank you to all of you that I met in these last six years, thank you to make me feel so lucky and to have marked my life with unique moments. Thank you for just being yourselves. I know that, despite distances and work commitments that will arise due to the fact that we are involuntarily growing, we will always find a way to meet each other again.

Furthermore, I want to say thank you to my tutors Prof. P. Sonato and prof. A. Ferro and to my co-supervisor R. B. Gomes that patiently helped me all work long and closed my gaps of knowledge explaining and repeating me how to proceed whenever I had doubts.

In fine, tutto questo non sarebbe stato possibile senza il sostegno e il supporto di una sola persona. Senza di te non avrei avuto l'occasione di vivere questa esperienza unica e irrepetibile, non avrei potuto studiare e realizzarmi professionalmente. Nonostante i nostri contrasti e le nostre diversità, so che posso e potrò sempre contare su di te. Grazie mamma.

BIBLIOGRAPHY

[1] Caineng Zou, Qun Zhao, Guosheng Zhang, and Bo Xiong. Energy revolution: From a fossil energy era to a new energy era. *Natural Gas Industry B*, 3(1):1–11, 2016.

[2] Georgina Santos. Road transport and co2 emissions: What are the challenges? *Transport Policy*, 59:71 – 74, 2017.

[3] U.S. Energy Information Amministration. EIA Outlook 2013. 2013.

[4] M Sadowski. Nuclear fusion-energy for future. *Nukleonika*, 50:53–58, 2005.

[5] Richard Kembleton. Nuclear fusion: What of the future? In *Managing Global Warming*, pages 199–220. Elsevier, 2019.

[6] Darya Ivanova. *Plasma-facing components in tokamaks: Material modification and fuel retention*. PhD thesis, KTH Royal Institute of Technology, 2012.

[7] Francesco Romanelli, P Barabaschi, D Borba, G Federici, L Horton, R Neu, D Stork, and H Zohm. Fusion electricity: A roadmap to the realization of fusion energy. 2012.

[8] A G Peeters. The physics of fusion power. *Lecture Notes*, 2009.

[9] Consorzio Rfx. Fisica e ingegneria della fusione : la ricerca verso una nuova fonte di energia.

[10] JA Romero, Stefano Coda, Federico Felici, Jean-Marc Moret, James Paley, G Sevillano, I Garrido, and HB Le. Sliding mode control of a tokamak transformer. In *Decision and Control (CDC), 2012 IEEE 51st Annual Conference on*, pages 386–393. IEEE, 2012.

[11] Bahman Zohuri. Nuclear energy research and development roadmap. In *Small Modular Reactors as Renewable Energy Sources*, pages 95–116. Springer, 2019.

[12] P. C. Stangeby. *The Plasma Boundary of Magnetic Fusion Devices*. Institute of Physics Publishing, 2000.

[13] NC Christofilos. Design for a high power-density astron reactor. *Journal of Fusion Energy*, 8(1-2):97–105, 1989.

[14] Darya Ivanova. *Plasma-facing components in tokamaks: Material modification and fuel retention*. PhD thesis, KTH Royal Institute of Technology, 2012.

[15] V Philipps. Tungsten as material for plasma-facing components in fusion devices. *Journal of nuclear materials*, 415(1):S2–S9, 2011.

[16] PV Romanov, Yu Shpanskij, AV Klischenko, VS Petrov, SA Moshkin, and AV Beznosov. feasibility of liquid gallium cooling for iter divertor cassette. In *Fusion Technology 1996*, pages 247–250. Elsevier, 1997.

[17] R Neu, J Riesch, JW Coenen, J Brinkmann, A Calvo, S Elgeti, C García-Rosales, H Greuner, T Hoeschen, G Holzner, et al. Advanced tungsten materials for plasma-facing components of demo and fusion power plants. *Fusion Engineering and Design*, 109:1046–1052, 2016.

[18] R. B. Gomes. *Interaction of a Liquid Gallium Jet with the Tokamak ISTTOK Edge Plasma*. Instituto Superior Técnico, 2009.

[19] Francisco L Tabarés. Present status of liquid metal research for a fusion reactor. *Plasma Physics and Controlled Fusion*, 58(1):014014, 2015.

[20] JW Coenen, G De Temmerman, G Federici, V Philipps, G Sergienko, G Strohmayer, A Terra, B Unterberg, T Wegener, and DCM Van den Bekerom. Liquid metals as alternative solution for the power exhaust of future fusion devices: status and perspective. *Physica Scripta*, 2014(T159):014037, 2014.

[21] CB Alcock, VP Itkin, and MK Horrigan. Vapour pressure equations for the metallic elements: 298–2500k. *Canadian Metallurgical Quarterly*, 23(3):309–313, 1984.

[22] F L Tabarés, E Oyarzabal, D Tafalla, A De Castro, F Medina, M A Ochando, B Zurro, K Mccarthy, and Tj-ii Team. Experimental tests of LiSn alloys as potential liquid metal for the divertor target in a fusion reactor. 12:1368–1373, 2017.

[23] RB Gomes, H Fernandes, C Silva, A Sarakovskis, T Pereira, J Figueiredo, B Carvalho, A Soares, P Duarte, C Varandas, et al. Interaction of a liquid gallium jet with isttok edge plasmas. In *AIP Conference Proceedings*, volume 996, pages 151–158. AIP, 2008.

[24] PR Luebbers, WF Michaud, and OK Chopra. Compatibility of iter candidate structural materials with static gallium. Technical report, Argonne National Lab., IL (United States), 1993.

[25] Fanghai Lu, Tangfu Xiao, Jian Lin, Zengping Ning, Qiong Long, Lihua Xiao, Fang Huang, Wankun Wang, Qingxiang Xiao, Xiaolong Lan, et al. Resources and extraction of gallium: A review. *Hydrometallurgy*, 174:105–115, 2017.

[26] Gordon Gang Liu. *Electrochemical behaviour of gallium arsenide*. PhD thesis, University of British Columbia, 1991.

[27] V Ya Prokhorenko, Vladimir Vladimirovich Roshchupkin, Mikhail Alexandrovich Pokrasin, SV Prokhorenko, and VV Kotov. Liquid gallium: potential uses as a heat-transfer agent. *High Temperature*, 38(6):954–968, 2000.

[28] FF Hahn, RK Wolff, and RF Henderson. Gallium oxide toxicity: an example of alveolar proteinosis in rats. *Annual Report of the Inhalation Toxicology Research Institute operated for the United States Department of Energy by the Lovelace Biomedical and Environmental Research Institute, October 1, 1986 through September 30*, 1987.

[29] LC Cadwallader. Gallium safety in the laboratory. energy facility contractors group (efcog) safety analysis working group (sawg) 2003 annual meeting. Technical report, INEEL/CON-03-00078 Preprint, 2003.

[30] Zhuo Zhao, Yongxiang Yang, Yanping Xiao, and Youqi Fan. Recovery of gallium from bayer liquor: A review. *Hydrometallurgy*, 125:115–124, 2012.

[31] SI Stepanov, VI Nikolaev, VE Bougrov, and AE Romanov. Gallium oxide, properties and applications: a review. *Rev. Adv. Mater. Sci*, 44:63–86, 2016.

[32] YL Wang and SJ Lin. Spatial and temporal scaling of oxide cluster aggregation on a liquid-gallium surface. *Physical Review B*, 53(10):6152, 1996.

[33] Jan M Chabala. Oxide-growth kinetics and fractal-like patterning across liquid gallium surfaces. *Physical Review B*, 46(18):11346, 1992.

[34] RB Gomes, R Mateus, E Alves, H Fernandes, C Silva, and P Duarte. Hydrogen retention in gallium samples exposed to isttok plasmas. *Fusion Engineering and Design*, 86(9-11):2458–2461, 2011.

[35] Yue-Guang Deng and Jing Liu. Corrosion development between liquid gallium and four typical metal substrates used in chip cooling device. *Applied Physics A*, 95(3):907–915, 2009.

[36] George H Miley and Celia Elliott. *16th IEEE/NPSS Symposium Fusion Engineering*. IEEE, 1990.

[37] SP Yatsenko, NA Sabirzyanov, and AS Yatsenko. Dissolution rates and solubility of some metals in liquid gallium and aluminum. In *Journal of Physics: Conference Series*, volume 98, page 062032. IOP Publishing, 2008.

[38] OI Tikhomirova, MV Pikunov, LP Ruzinov, and ID Marchukova. Interaction of liquid gallium with copper. *Soviet materials science: a transl. of Fiziko-khimicheskaya mekhanika materialov/Academy of Sciences of the Ukrainian SSR*, 5(6):586–590, 1972.

[39] F Barbier and J Blanc. Corrosion of martensitic and austenitic steels in liquid gallium. *Journal of materials research*, 14(3):737–744, 1999.

[40] KA Narh, VP Dwivedi, JM Grow, A Stana, and W-Y Shih. The effect of liquid gallium on the strengths of stainless steel and thermoplastics. *Journal of materials science*, 33(2):329–337, 1998.

[41] Nicolas Eustathopoulos. Wetting by liquid metals—application in materials processing: the contribution of the grenoble group. *Metals*, 5(1):350–370, 2015.

[42] Girish Kumar and K Narayan Prabhu. Review of non-reactive and reactive wetting of liquids on surfaces. *Advances in colloid and interface science*, 133(2):61–89, 2007.

[43] Nicolas Eustathopoulos. Wetting by liquid metals—application in materials processing: the contribution of the grenoble group. *Metals*, 5(1):350–370, 2015.

[44] Sina Ebnesajjad and Cyrus Ebnesajjad. *Surface treatment of materials for adhesive bonding*. William Andrew, 2013.

[45] Yuehua Yuan and T Randall Lee. Contact angle and wetting properties. In *Surface science techniques*, pages 3–34. Springer, 2013.

[46] Gershon Wolansky and Abraham Marmur. The actual contact angle on a heterogeneous rough surface in three dimensions. *Langmuir*, 14(18):5292–5297, 1998.

[47] A Mortensen, B Drevet, and N Eustathopoulos. Kinetics of diffusion-limited spreading of sessile drops in reactive wetting. *Scripta Materialia*, 36(ARTICLE):645, 1997.

[48] Robert N Wenzel. Surface roughness and contact angle. *The Journal of Physical Chemistry*, 53(9):1466–1467, 1949.

[49] Peter S Swain and Reinhard Lipowsky. Contact angles on heterogeneous surfaces: A new look at cassie's and wenzel's laws. *Langmuir*, 14(23):6772–6780, 1998.

[50] Bernard Miller and Raymond A Young. Methodology for studying the wettability of filaments. *Textile Research Journal*, 45(5):359–365, 1975.

[51] Yi-Ning Lee and Shu-Min Chiao. Visualization of dynamic contact angles on cylinder and fiber. *Journal of colloid and interface science*, 181(2):378–384, 1996.

[52] Min Li, Zuo Guang Zhang, and Zhi Jie Sun. Contact angle of epoxy resin measured by capillary impregnation and the wilhelmy technique. *Polymers and polymer composites*, 14(3):251–259, 2006.

[53] Trong Dang Vu and Hupka Jan. Characterization of porous materials by capillary rise method. *Physicochemical Problems of Mineral Processing*, 39, 01 2005.

[54] Robert Craig Maze. An ultrahigh vacuum study of wetting in liquid metal, solid metal systems. 1970.

[55] WC Bigelow, DL Pickett, and WA Zisman. Oleophobic monolayers: I. films adsorbed from solution in non-polar liquids. *Journal of Colloid Science*, 1(6):513–538, 1946.

[56] Neil K Adam and Gilbert Jessop. Ccl.—angles of contact and polarity of solid surfaces. *Journal of the Chemical Society, Transactions*, 127:1863–1868, 1925.

[57] Sina Ebnesajjad and Cyrus Ebnesajjad. *Surface treatment of materials for adhesive bonding*. William Andrew, 2013.

[58] Edward W Washburn. The dynamics of capillary flow. *Physical review*, 17(3):273, 1921.

[59] Trong Dang-Vu and Jan Hupka. Characterization of porous materials by capillary rise method. *Physicochemical problems of mineral processing*, 39:47–65, 2005.

[60] JC Ambrose, MG Nicholas, and AM Stoneham. Dynamics of liquid drop spreading in metal-metal systems. *Acta metallurgica et materialia*, 41(8):2395–2401, 1993.

[61] N Eustathopoulos. Dynamics of wetting in reactive metal/ceramic systems. *Acta Materialia*, 46(7):2319–2327, 1998.

[62] V Bougiouri, R Voytovych, O Dezellus, and N Eustathopoulos. Wetting and reactivity in ni–si/c system: experiments versus model predictions. *Journal of materials science*, 42(6):2016–2023, 2007.

[63] Quanzi Yuan, Jinhong Yang, Yi Sui, and Ya-Pu Zhao. Dynamics of dissolutive wetting: a molecular dynamics study. *Langmuir*, 33(26):6464–6470, 2017.

[64] George S. Gardner. *Handbook of chemistry*, volume 229. 1940.

[65] RL Montgomery, PC Sundareswaran, DW Ball, and JL Margrave. Thermodynamic properties by levitation calorimetry—v. high-temperature heat content of liquid gallium. *International journal of thermophysics*, 5(2):161–175, 1984.

[66] SC Hardy. The surface tension of liquid gallium. *Journal of crystal growth*, 71(3):602–606, 1985.

[67] D.W. Green. *PERRY'S CHEMICAL ENGINEER'S HANDBOOK 8/E SECTION 2 PHYSICAL & CHEM DATA (POD)*. McGraw-Hill Education, 2007.